University of Alberta
Department of Civil &
Environmental Engineering

BEHAVIOUR OF

DISTORTION-INDUCED FATIGUE

CRACKS IN BRIDGE GIRDERS

by

Robert E.K. Fraser

Gilbert Y. Grondin

and

Geoffrey L. Kulak

December, 2000

BEHAVIOUR OF DISTORTION-INDUCED FATIGUE CRACKS IN BRIDGE GIRDERS

by

Robert E. K. Fraser

Gilbert Y. Grondin

and

Geoffrey L. Kulak

Structural Engineering Report 235

Department of Civil and Environmental Engineering
University of Alberta
Edmonton, Alberta, Canada

December, 2000

ABSTRACT

Many older multi-girder bridges exhibit distortion-induced fatigue cracking at the diaphragm-to-girder connections. Even when such fatigue cracks are relatively small, they are of concern to owners because of the possibility of brittle fracture under conditions of dynamic loading and cold temperatures. These circumstances are often seen in railway bridges, especially in Canada. The opportunity to examine this situation arose when CN Rail made available a multi-girder bridge that was being replaced because of clearance demands. The bridge was a composite slab-on-girder skewed (28°) bridge in which the diaphragms had been placed at right angles to the girders and were therefore discontinuous. The bridge had over 300 distortion-induced fatigue cracks in the web gap region of the diaphragm connections at the time it was taken out of service. Stop-holes had been drilled at most crack locations.

The work performed in the first part of the investigation consisted of field testing to determine the characteristics of the bridge before it was dismantled. The girders were tested in the laboratory with the diaphragms attached. The test setup was designed to replicate the measured field conditions. Structural Engineering Report 235 presents the results of fatigue tests on three of the girders obtained from this bridge. All of these fatigue tests were conducted at a stress range equal to that measured in the field under heavy locomotive loading applied dynamically. The fatigue tests were conducted at room temperature. Subsequent to the fatigue tests, both crack stability and crack propagation rates were examined at low temperature ($-50°$C).

It was observed that, although the fatigue cracks had been repaired in the field by drilling holes at the crack tips, most of the cracks reinitiated within one million cycles of fatigue loading. Indeed, some had already reinitiated in the field. The low temperature tests were conducted under both static and cyclic loading conditions. Some of these tests were conducted when fatigue cracks had extended into the web to a length of nearly 250 mm. At the end of fatigue testing (after 3.7 to 4.7 million cycles), all specimens were tested statically at low temperature at a static stress in the bottom fiber of the girder twice as large as the peak stress measured in the field. Under all testing conditions the fatigue cracks remained stable. All three fatigue tests reported in this report were conducted at a stress range of 35 MPa at the bottom fiber of the test specimens.

More girders are now being tested. These tests include use of different stress ranges in order to establish an S-N curve for the remaining life prediction of this type of detail. In addition, the effectiveness of some repair techniques will be explored. Finite element analysis of the girders is being carried out in order to investigate the stresses in the web gap region.

ACKNOWLEDGEMENTS

TABLE OF CONTENTS

LIST OF TABLES

LIST OF FIGURES

CHAPTER 1

INTRODUCTION

1.1 General Background

Many multigirder bridges contain diaphragm members that are intended to brace the girders during construction, to aid in the transfer of lateral loads, and, to some extent, distribute live loads amongst girders. Common construction practice is to connect the diaphragm members to each girder through transverse connection plates that are welded to the girder web. In the past, these connection plates were commonly cut short of the girder flanges, both to increase the fabrication tolerances of the plates and because it was considered that the connection of these plates to the tension flange would produce a severe fatigue detail.

In the years following their construction, many multigirder bridges began to exhibit fatigue cracks in the web gaps that existed between the girder tension flange and the end of the transverse connection plate. Generally, such fatigue cracks are considered to be the result of differential displacements between adjacent girders, which produces a racking motion of the diaphragms and creates a concentration of deformation in the web gap region. The concentrated deformations produce stresses in the web gap that are large enough to initiate fatigue cracking in relatively few load cycles. These distortion-induced fatigue cracks are usually more pronounced when the diaphragms are staggered, such as is often the case in skewed bridges.

One of these multigirder-skewed bridges with staggered diaphragms is the St. Albert Trail Mile 5.09 Subdivision bridge, which carries CN main line traffic over the St. Albert Trail in Edmonton, Alberta. The St. Albert Trail Mile 5.09 Subdivision crossing, which was placed in service in 1965, is comprised of two parallel bridges, in which each bridge has eight parallel steel girders interconnected by staggered steel diaphragms. The four span bridge (9.9 m–17.3 m–17.3 m–9.9 m) is composite with a 268 mm thick concrete deck. A construction joint separates each set of eight girders into two sets of four girders, even though diaphragms span beneath the joint in the concrete deck. The bridge is on a 28º RHF skew, but the steel diaphragms are perpendicular to the bridge girders: thus, they are not continuous at a given location across the width of the bridge. Figures 1−1 and 1–2 show a plan view and typical section of the bridge structure.

The diaphragm members are connected to the girder through transverse stiffeners that are welded to the girder web and top flange, but cut 50 mm short of the top surface of the

bottom flange. By 1998, over 300 web cracks at the lower ends of the diaphragms connection plates had been observed during routine inspections. In 1985, a rehabilitation program was undertaken to repair the girders that were damaged due to impact from road traffic passing under the bridge and to arrest the growth of fatigue cracks that had initiated in the girder web gaps. In an attempt to arrest the fatigue cracks, 24 mm holes were drilled at the crack tips to relieve the stress concentrations that were affecting crack growth. Between 1995 and 1998, crack extensions beyond the drilled holes were observed at several web gap locations. Because of the large number of fatigue cracks and the substandard clearance between the roadway and the underside of the bridge, the owner decided to replace the bridge. The superstructure of the bridge was replaced with a new structure in August 1998.

1.2 Objectives

A short time before the bridge was removed, field testing was carried out to measure the deflections and strains in one set of the 9.9 m spans under the north–east structure (see Figure 1–1). Two CN Rail EF–644a locomotives were used to conduct both static and dynamic tests. At the time of dismantling, the University of Alberta obtained four sets of three girders, each from the 9.9 m north spans. The concrete slab and the fascia girder were then removed from each set in order to reduce the weight of the specimens for shipping. The girders were then used to explore the behaviour of the fatigue cracks that had developed at the bottom of transverse stiffeners while the bridge was in service.

Starting in October 1999, an experimental program on the full-scale bridge girders was undertaken at the University of Alberta. The objectives of the test program were:

1. Determine the characteristic behaviour of the bridge using the field data;

2. Design a test setup and procedure to replicate in the laboratory the strain and displacement conditions observed in the field;

3. Study the behaviour of the distortion-induced fatigue cracks in three of the girders obtained from the bridge (see Figure 1–1);

4. Determine the remaining fatigue life of the bridge girders under a stress range equal to that observed in the field under loading with the EF–644a locomotives;

5. Assess the stability of distortion-induced fatigue cracks at -50°C.

1.3 Scope of Research

The research program presented in the following chapters was limited in scope as follows:

1. Field instrumentation was limited to the north–east short span under the main line;

2. Field testing was limited to EF–644a locomotive loading;

3. Three test specimens were tested;

4. All three test specimens were tested at a stress range equal to that determined in the field test, namely, 35 MPa in the bottom flange.

4
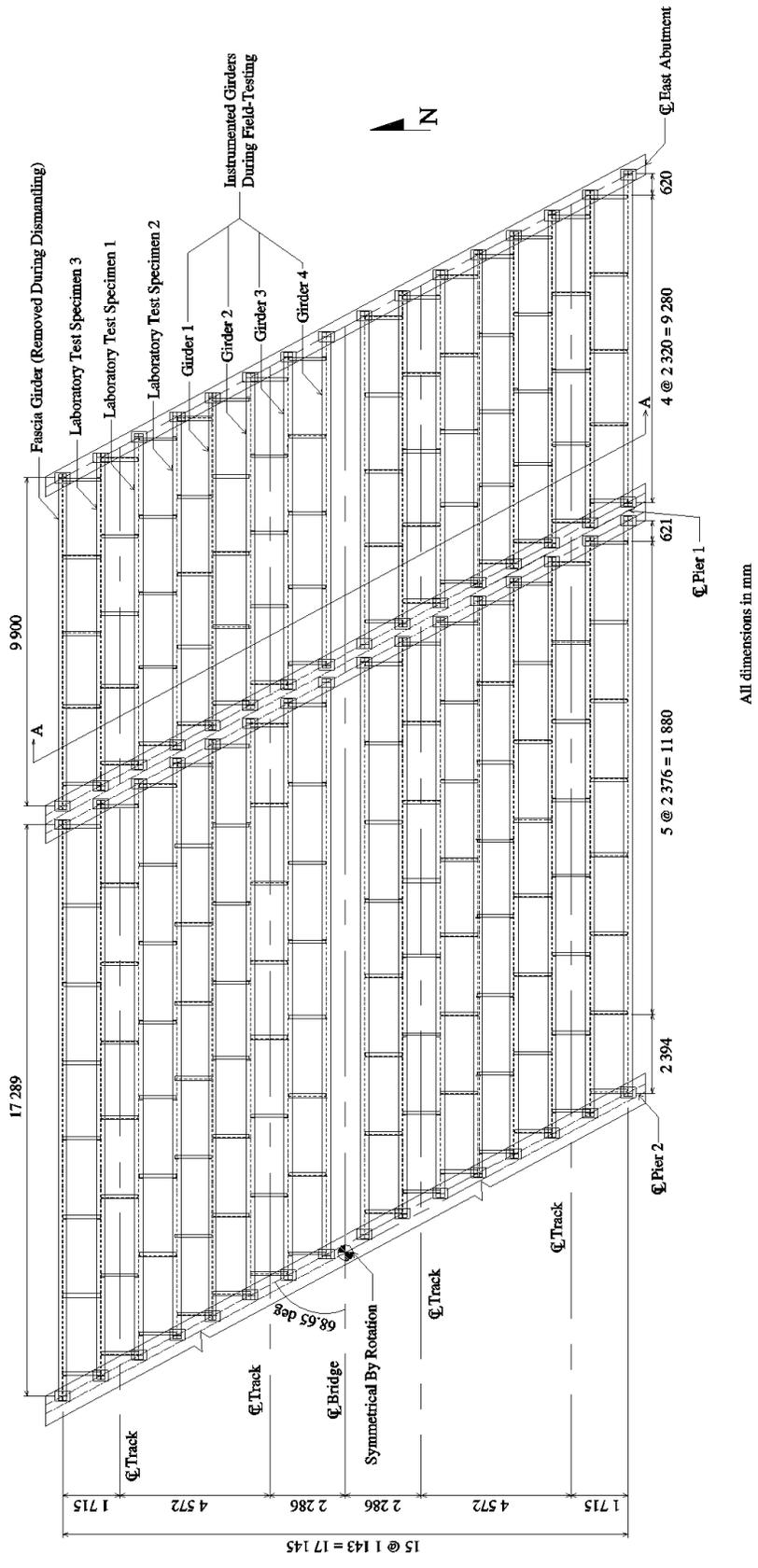
Figure 1–1 Plan View of CN Mile 5.09 Edson Subdivision Bridge

Fascia Girder (Removed During Dismantling)

Laboratory Test Specimen 3

Laboratory Test Specimen 1

Laboratory Test Specimen 2

Instrumented Girders
During Field-Testing

Girder 1

Girder 2

Girder 3

Girder 4

℄ East Abutment

620

4 @ 2 320 = 9 280

℄ Pier 1

621

5 @ 2 376 = 11 880

2 394

℄ Pier 2

All dimensions in mm

N

9 900

17 289

A

A

℄ Track

℄ Track

℄ Track

℄ Bridge

Symmetrical By Rotation

℄ Track

68.65 deg

1 715

4 572

2 286

2 286

4 572

1 715

15 @ 1 143 = 17 145

Figure 1–2 Typical Bridge Cross-Section

Section A-A

All dimensions in mm

Section B-B

L 102 x 102 x 9.5
Diaphragm Flange Section

9.5 mm x 686 mm
Diaphragm Web Plate

L 102 x 102 x 9.5
Diaphragm Flange Section

737

16 mm x 254 mm
Interior Girder Flange

16 mm x 254 mm
Interior Girder Flange

22 mm dia. Studs

9.5 mm x 914 mm
Interior Girder Web

268 mm Concrete Slab

51

Diaphragm

Exterior Fascia Girder

ℂ Bridge

ℂ Track

ℂ Track

ℂ Track

B

B

572

2 286

4 572

1 715

7 @ 1 143 = 8 001

CHAPTER 2

LITERATURE REVIEW

2.1 General

There are two major aspects of research undertaken in this thesis. The first deals with distortion-induced fatigue cracking of full-scale bridge girders due to the presence of short web gaps at diaphragm positions. The second is the behaviour of the resulting fatigue cracks under extreme cold temperatures, which is known to reduce the toughness of the steel and may lead to crack instability.

Many of the research programs carried out to date on distortion-induced fatigue cracking of bridge girders containing diaphragms have concentrated on fatigue life and possible rehabilitation schemes. For the most part, the behaviour of fatigue cracks under low temperature conditions was not studied. A number of research programs have investigated the behaviour of cracks at several types of fatigue-prone details under low temperature conditions. A review of these research programs is presented herein.

Current detailing guidelines proposed in design codes to guard against distortion-induced fatigue cracking are also reviewed.

2.2 Distortion–Induced Fatigue Cracking of Bridge Girders Containing Diaphragms

2.2.1 General Background

The interaction of the various components of a bridge structure under normal service loading can result in cracking at unexpected locations in a relatively short time (Fisher, 1978). In multigirder bridges, diaphragm members are present for construction purposes, to transfer lateral loads and, to some extent, to distribute live loads among the girders. These diaphragms commonly are connected to the girders at the location of transverse stiffeners welded to the girder web. In the past, transverse stiffeners were often cut short of the girder tension flange. In bridge girders, fatigue cracks resulting from out-of-plane deformations are common in webs where short gaps between the stiffener and the flange exist (Fisher and Keating, 1989). The differential displacement between adjacent girders under live loads causes a racking motion in the diaphragms, resulting in a concentration of deformation in the flexible web gap location (since the cross-sectional shape of the stiff diaphragm is maintained). This problem is accentuated when diaphragms are placed on only one side of the girder web such as at exterior girders or in skewed bridges where diaphragms are staggered.

The fatigue cracks that result from out-of-plane displacements usually extend across the weld toe at the end of the transverse connection stiffener and into the web. Then, if crack growth is allowed to continue, the crack turns upward and is perpendicular to the primary stress field. Figure 2–1 illustrates the typical deformation resulting at a web gap location.

Most displacement-induced secondary stress problems resulting in fatigue crack growth are difficult to anticipate at the design stage because of the difficulty in estimating the stress range in the web gap. Over the past few decades, understanding of distortion-induced fatigue cracking has improved significantly and detailing guidelines to prevent such problems have been developed. The use of full depth transverse stiffeners with positive connection to the flanges or an increase in the length of the web gap have both been shown to improve the fatigue life at diaphragm connections. Unfortunately, prior to the 1983 American Association of State Highway and Transportation Officials (AASHTO) Bridge Specifications (AASHTO, 1983), it was customary not to attach the transverse stiffener to the tension flange. Furthermore, no guidelines had been developed to ensure that the appropriate flexibility was present in the web gap region. In fact, positive connections between the transverse stiffener and the girder flanges were usually not provided in order to avoid the need for cutting the stiffeners to precise lengths and because it was considered that welding the stiffeners to the tension flanges would create fatigue-prone details at these locations. Over the past 20 years, experience has shown that the fatigue life of this detail is independent of whether the stiffener terminates in the web or is extended down to the flange (Fisher *et al.*, 1998). A large number of bridges with fatigue-prone web gap details are still in service today. Therefore, research to determine the behaviour and remaining life of these structures is important from both economic and safety-related points of view.

2.2.2 Studies on Distortion-Induced Fatigue Cracking in Bridges Containing Web Gaps

Research at Lehigh University

In 1978, Fisher presented an investigation of three cases of distortion-induced fatigue cracking resulting from out-of-plane displacements (Fisher, 1978). Only two of these cases will be discussed herein. The first case involved cracks at the ends of transverse stiffeners that were cut short of the flanges in several plate girders. Most of the cracks were discovered either before erection of the girders or shortly after they were erected. Examination of these details indicated that cracks had formed at the weld toes at the end of the stiffeners and had extended across the weld, into the web and, in some cases, had started to turn upward, perpendicular to the primary stress field. Figure 2–2 illustrates the crack patterns observed during field inspections. Crack initiation and growth was believed to have occurred during shipping of the girders to the site by rail. Differential

movements of the girder flanges, caused by the swaying motion of the train, likely induced sufficiently large strains in the web gap to initiate and propagate the cracks.

In the second case, Fisher (1978) investigated fatigue cracks in the web gaps of longitudinal bridge girders at the connection of transverse beams. The cracks had developed due to the end rotations of the transverse beams, which were bolted to stiffeners that had been welded to the web of the longitudinal girders. None of the stiffeners were connected to the girder flanges. Cracks developed in positive moment regions at the tension flange near the end supports and adjacent to the top flange in the negative moment regions. In order to determine the magnitude of strains resulting from distortion of the web, strains were measured on the girder web near the web gap regions at several floor beam locations. These measurements indicated that the strains were significantly higher in the negative moment regions, where the concrete slab restrained the embedded top flange. The strain measurements also showed that the transverse beams were pushing the web out-of-plane and, as a result, the gap was subjected to double curvature. For a typical record, the level of stress in the top gap ranged from 130 MPa in compression near the top flange to 124 MPa in tension at the end of the stiffener. Using the records from over 300 vehicles, the equivalent stress range in the top gap was determined to be 99 MPa. At the bottom web gap, the resulting stress gradients were significantly smaller since the level of restraint was less than the restraint from the concrete slab at the top web gap detail. Furthermore, strain measurements at existing crack sites indicated visible signs of cracking and a high stress range near the crack surfaces. This indicated that these cracks would continue to grow unless measures were taken to stop crack growth.

The repair strategy consisted of first welding the stiffeners to the flanges and then drilling "stop holes" at the crack tips in order to relieve the stress concentration and arrest the cracks. In areas where welding of the stiffeners to the flanges would be difficult, cutting back the stiffener to increase the length of the web gap was recommended.

Fisher and Keating (1989) also investigated the behaviour of distortion-induced fatigue cracks in web gaps of bridge girders. Several field studies were performed at various in service bridge details in order to determine the stresses and out-of-plane distortions in the web gap of typical structures. The relative out-of-plane distortions between the end of the stiffener and the flange ranged between 0.013 mm to 0.025 mm under service loading conditions and the bending stresses in the web gap ranged from 10 MPa to 97 MPa. Furthermore, all strain measurements taken in the web gaps showed that reverse curvature bending was present.

The field investigations indicated that the relatively high stress levels in the gap region usually caused cracking within the first ten years of the service life of the bridges.

Generally, cracks were found to initiate at the web gap boundaries, where the maximum bending stresses, induced by the relatively small deformations are located. The parametric field study showed that the weld type or the treatment of the weld at the end or the stiffener does not influence the probability of cracking.

The rehabilitation procedures proposed by these authors were similar to those outlined by Fisher in 1978. In addition to drilling holes at crack tips, it was suggested that the crack path between the drilled holes be saw-cut in order to ensure free movement between crack surfaces. Saw cutting was suggested because crack surfaces tend to be jagged and cause significant distortion-induced stresses to be present, even after cracks have formed.

Castiglioni *et al.* (1988) presented a numerical investigation of web gaps subjected to out-of-plane displacements in multigirder steel bridges. A parametric study was carried out to determine the effects of varying the ratio g/t_w, where g represents the web gap length and t_w denotes the web thickness. A finite element model of the Beaver Creek Bridge and its details was calibrated using data collected during field testing of the bridge. Several load cases were applied to the models in order to determine the behaviour of the structure under load. For each load case, web gap lengths of 100 mm, 50 mm and 0 mm were examined. The results obtained from the 50 mm and 100 mm web gaps indicated that the concentrated deformations are independent of the length of the gap. Furthermore, nearly no concentrated deformation was observed when the web gap was reduced to 0 mm. It was also observed that the direction of the web gap deformation can reverse, depending on the position of the live loads on the bridge. Next, the thickness of the web was varied from 7.6 mm to 14.25 mm. The global bending stiffness of the members was maintained by slightly reducing the flange width (from 418 mm to 354 mm) for each trial web thickness. Each combination of web gap length and web thickness was analysed and the concentrated deformations at the web gaps were compared. The results indicated that varying the gap length had very little influence on the web distortions but that increasing the web thickness caused a reduction in the magnitude of the relative displacements. At a gap length of 50 mm, increasing the web thickness resulted in a significant increase in the bending stresses in the gap region. On the other hand, no appreciable increase in stresses resulted when the web gap was 100 mm long and the web thickness was increased. The deformation results also reinforced the earlier findings with regard to the reversal of deformations occurring at a gap location for different loading conditions. Furthermore, the results showed clearly that the gaps were subjected to double curvature.

The effect of the web gap size, g, and web thickness, t_w, on the diaphragm member forces was also investigated. It was found that the gap stiffness has essentially no effect on the vertical components of force in the diaphragms and that the vertical deflection of the girders was actually the main influencing factor. On the other hand, horizontal forces that may arise in the diaphragms as the result of lateral wind or earthquake loads are

10

strongly influenced by the gap length. Little difference in the magnitude of the horizontal forces was observed when the gap length was changed from 50 mm to 100 mm, but when the gap length was reduced to 0 mm a sharp increase in the diaphragm forces was noticed.

One of the major conclusions that arose from this numerical study was that a change in length of the web gap has little effect on the magnitude of the deformations. Hence, rehabilitation schemes that involve cutting back the stiffener to increase the gap length and decrease the gap stiffness may decrease the stresses in the web gap enough to reduce the probability of developing distortion-induced fatigue cracks in these areas.

Research at Auburn University

In the mid 1990s, a series of studies dealing with the behaviour and cracking of the diaphragm-to-girder connections were undertaken at Auburn University. These studies included finite element modelling to study the diaphragm–girder interaction behaviour and field studies of multigirder bridges containing diaphragms.

In 1995, Tedesco, Stallings and Tow presented the results of a numerical study of the behaviour of multigirder bridges with and without diaphragms. Bridges with no diaphragms were studied since removal of the diaphragms would completely eliminate the distortion-induced fatigue problems in the girder web gaps. A three-dimensional dynamic finite element analysis of a multigirder steel bridge was performed in order to calibrate the model. The results of a case study performed on a bridge located on the I-65 highway in Birmingham, Alabama were used as the basis of the calibration. Using the calibrated model, dynamic analyses of the bridge were performed with and without the diaphragms. The results indicated that increases of 8 to 9 percent in the bottom fiber stresses and midspan deflections occurred when the diaphragms were removed. The change in relative displacements between adjacent girders was also studied. With the diaphragms removed, it was found that the maximum increase in relative deflection was about 25%, which resulted in a significant increase in the transverse slab bending moments. For the particular bridge investigated, the increase in slab bending moments was considered acceptable.

Since the increase in slab moments due to the removal of diaphragms can be significant, a comprehensive study of the increase in slab moments should be completed for each bridge before such a drastic rehabilitation scheme is adopted. Furthermore, the need for diaphragms to provide lateral support to the girders and in transferring lateral loads safely through the structure should also be assessed before any of these members are removed.

Stallings, Cousins and Stafford (1999) investigated the effect of removing the interior diaphragms from a 76 m, three-span, continuous steel girder bridge located in

Birmingham, Alabama. The non-skewed superstructure consists of eight wide flange girders that support a non-composite concrete deck. Prior to removal of the diaphragms, the end spans had two lines of interior diaphragms and the center span had four lines of interior diaphragms. In addition, diaphragm members were located at all four support positions. Six series of field tests were performed with and without the diaphragms in place. A comparison of the bridge behaviour with and without diaphragms indicated that diaphragms had little effect on the live load distribution in the bridge: the increase in stresses and deflections was small. The authors did not identify the effect of removing the diaphragms on the ability of the bridge to resist lateral loads. The importance of the diaphragm members in the overall structural response must be assessed before these elements are removed from any bridge.

In the past, the Alabama Department of Transportation used specific techniques to repair fatigue cracking at diaphragm-to-girder connections, but inspections revealed that many of the repaired and unrepaired details were experiencing distortion-induced fatigue cracks. Cousins *et al.* (1998) investigated all the typical diaphragm-to-girder connection details in service in Alabama. Discussions on this research are limited to the behaviour of the original welded connection details.

During the summers of 1993 and 1994, field tests were performed at the diaphragm-to-girder connections of several bridges. Strain gauges were mounted in several web gaps to monitor the horizontal and vertical strains during field testing. The service stress ranges in the gaps containing no cracking at the time of testing were determined and compared with an upper bound fatigue limit, described below, to see if cracking at these locations was to be expected. Out of 250 random truck load events, if any single event resulted in a stress range greater than the assumed fatigue limit, then it was considered that cracking would occur during the service life of the structure. This assumption was made because a single event in 250 corresponds to a large number of events over the service life of the structure. If none of the measured stress ranges were greater than the assumed threshold stress, then it was assumed that cracking would not occur. Although the authors acknowledged the statistical shortcomings of this assumption, it was never really put to the test since: in most instances, the measured stress ranges suggested that cracking was to be expected.

Based on results from others (Fisher, 1978), the fatigue detail at the stiffener-to-web junction was assumed by Cousins *et al.* (1998) to be Category C with a fatigue limit of 69 MPa. At the flange-to-web junction the category was assumed to be Category A with a fatigue limit of 165 MPa since the girder was a rolled steel section. In more than half of the web gaps monitored, there was at least one measured stress range that exceeded the fatigue limits assumed for the critical web gap details. The maximum of the horizontal and vertical stresses measured at each end of the web gap was compared with the

applicable fatigue limit to determine whether cracking was to be expected. Principal stresses were not used, which likely would have shown that even more of the service stress ranges exceeded the fatigue limits. Furthermore, the strain gauges were positioned outside the web gap area and linear extrapolation was used to estimate the actual stresses in the web gap region. This resulted in lower bound estimates of the stresses in the web gap since the stress distribution is not linear in and around the web gap region. Nonetheless, the results showed that further fatigue cracking due to distortion-induced stresses was to be expected in the web gaps at welded transverse stiffener connections.

Other Research

Barth and Bowman (1999)

Barth and Bowman (1999) investigated the fatigue behaviour of a diaphragm detail in which a hot-rolled wide flange diaphragm member was welded directly to the girder web at mid-height of the girder. Intermittent welds along the diaphragm web and short welds along the flanges were used for the connection.

Fatigue cracks were detected in a significant number of diaphragm welds during bridge inspections. These cracks were found primarily in the intermittent web welds and in the bottom flange welds. At the time of inspection, no crack propagation into the girder webs was observed. In order to determine the behaviour of these cracks, a fatigue-testing program comprised of nine steel beams with welded diaphragms was conducted. A given test consisted of three girders attached together with diaphragms. All three girders were simply supported and only the middle girder was loaded. All diaphragms were attached to the exterior girders by means of bolted connections.

Two different diaphragm configurations, staggered and non-staggered, were investigated in the test program. Static load tests showed that when the diaphragms were not staggered they acted as rigid connections that transferred loads to adjacent beams as long as the diaphragm-to-girder welds were intact. In the staggered diaphragm configuration, used to simulate the typical arrangement of diaphragms in a skewed bridge, it was observed that the diaphragm pulled the web out-of-plane, as expected. The fact that out-of-plane web distortions were only present in the staggered diaphragm tests can be attributed to the design of the test setup. The three-girder test setup and loading configuration used in this research ensured that in the non-staggered diaphragm configuration the forces in opposite diaphragms at any one location were equal. This, in turn, ensured that no loads were transferred to the girder web and that no apparent out-of-plane web distortions were occurring. This behaviour is not representative of multigirder bridges containing non-staggered diaphragms. In fact, the forces and racking motion in adjacent diaphragms in

real bridges are significantly different and this difference causes some distortion in the web gaps, as reported elsewhere (Castiglioni *et al.*, 1988; Cousins *et al.*, 1998).

Results of cyclic tests showed that cracking in the diaphragm-to-web welds at the non-staggered diaphragm positions took place after only a few thousand cycles. Cracking occurred because the load effects transferred from the diaphragms to the welds created stresses in the welds large enough to initiate cracking after a small number of cycles. Cracking was observed in both the intermittent web welds and the bottom flange welds. Since no distortion of the web was occurring at these diaphragm locations, cracking during the test was restricted to the welds.

Limited cracking was observed in the test specimens that had staggered diaphragms. This was because the diaphragms were mounted near the neutral axis of the girder, where the primary bending stresses are small, and because the length of the web gaps (approximately 110 mm) were large enough to reduce the stresses in the web to a level less than the fatigue limit.

At the locations where cracking did occur, crack growth was slow because of the geometry and orientation of the diaphragm connection. Barth and Bowman suggest that the reason for the low crack growth rates was that the diaphragms were attached to the beams near the neutral axis of the members where in-plane bending stresses are relatively small and because of the inherent flexibility in the web gap.

Lai (1997)

Lai (1997) investigated the effectiveness of hole drilling as a fatigue crack stopping method. This work is reviewed because hole drilling repairs had been carried out in the girders that were obtained from CN Rail and used for the test program presented in the following chapters. Lai performed a series of finite element analyses to assess the effectiveness of hole drilling at various fatigue crack lengths.

Drilling holes at the tips of fatigue cracks generally is considered to be an effective measure to retard or stop crack growth in steel bridges. Although a drilled hole represents a stress raiser, this effect is more than offset by the fact that the stress intensity factor is substantially reduced when the sharp crack tip is replaced by a hole of finite radius.

The hole drilling criterion, based on linear fracture mechanics and limited full-scale bridge attachment test data, proposed by Fisher *et al.* (1980) can be used to determine the size of holes necessary to arrest crack growth. The criterion to prevent crack re-initiation from the drilled hole is given as

$$\frac{\Delta K}{\sqrt{r}} = \frac{\Delta s \cdot \sqrt{p \cdot A_r}}{\sqrt{r}} < 10.5 \cdot \sqrt{s_y} \qquad (1)$$

where: ΔK = range stress intensity factor range;

r = radius of the drilled holes (mm);

A_r = half the equivalent crack length after rehabilitation (mm);

Δs = nominal stress range (MPa);

s_y = yield strength of the material (MPa).

Lai investigated the validity of Equation 1 by computing the true stress concentration factor at the rim of holes using finite element models and Mode I loading. The numerical analysis indicated that Equation 1 may give unconservative results in terms of crack reinitiation for large crack lengths.

Lai also discussed the applicability of Equation 1 when out-of-plane web distortions are the cause of cracking. He suggested that when out-of-plane distortions are present the deformation at the rims of the holes becomes Mode III (tearing or antiplane shear mode) with significant shear stresses present in the direction of the plate thickness. He proposed that deformation modes in addition to Mode I should be examined in order to determine if crack re-initiation at the rims of drilled holes can be expected when out-of-plane distortions are the cause of cracking. This suggestion is supported by the fact that further cracking past holes that satisfy Equation 1 was observed at web gap locations in the St. Albert Trail Mile 5.09 Subdivision bridge prior to its removal from the site. Further research is required in this area in order to come up with an effective criterion. Until this is available, drilling holes at distortion-induced fatigue crack tips should only be considered as a temporary measure because crack re-initiation is likely.

2.2.3 Current Design Specifications

Clause 6.6.1.3 of the 1998 AASHTO LRFD Bridge Design Specification provides guidelines intended to guard against distortion-induced fatigue (AASHTO, 1998). Clause 6.6.1.3.1 of the Specification states that transverse connection plates shall be attached to both the compression and tension flanges of the longitudinal members in situations where diaphragms, cross-frames, and floor-beams are attached to transverse connection plates or transverse stiffeners. Current AASHTO guidelines do not permit a gap to exist between the stiffener and the flanges, regardless of the gap length and flexibility provided.

Clause 7.17.6.2 of the Canadian Highway Bridge Design Standard (CAN/CSA-S6-88) states that strains due to out-of-plane displacements shall be calculated and the corresponding stress ranges computed. However, no guidance is offered for the calculation of the web gap strains and stresses. The Standard requires that the calculated stress ranges not exceed the allowable stress ranges tabulated for each fatigue category in Table 19 of Clause 7.17.3 by more than 1.2 times (CSA, 1988). The guideline is of limited use, however, since accurate calculation of the stresses resulting from out-of-plane distortions is usually difficult. This Standard is currently (2000) under revision.

The Manual for Railway Engineering (AREA, 1994) provides no guidance to designers for dealing with the problem of distortion-induced fatigue cracking in bridge structures.

2.3 Crack Behaviour at Low Temperatures

2.3.1 General

The fatigue life of a structural component can be broken down into three stages: crack initiation, crack growth, and fracture (Reed and Clark, 1983). Fatigue cracks propagate until they reach a critical length, at which time the toughness of the material is exceeded and fracture results. To ensure the fracture safety of structures, knowledge of the largest tolerable crack sizes under the most severe service conditions is required.

In most modern steel structures, the fracture toughness properties of the material are such that the likelihood of fracture shortly after erection is very low. Fabrication techniques, rational designs and the use of fine-grained steels should provide high toughness and large critical crack sizes, a_{cr}. Unfortunately, the presence of initial flaws and defects in structures, although initially much smaller than a_{cr}, propagate over time due to fatigue, corrosion, stress corrosion, etc. (Fisher *et al.*, 1998).

As the ambient temperature is lowered, the yield strength of most metallic materials increases, and ductility and fracture toughness decrease (Suresh, 1998). When the fracture toughness of a material has been exceeded, it fractures. Since lower temperatures reduce the fracture toughness of a material, it is important to ensure that sufficient fracture toughness exists at the lowest expected service temperature so that the critical crack size remains larger than the size of existing cracks.

Several approximate fracture toughness tests exist, for example, the Charpy V-notch (CVN) impact test and the slow bend test. None of these tests can duplicate the conditions in the actual structural details; therefore, the critical crack length cannot be assessed directly. The results of these fracture tests can be converted into approximate critical crack lengths using fracture mechanics models, but only for relatively simple

details. For complex details, such as details prone to distortion-induced fatigue, this simple and empirical procedure cannot provide accurate estimates of the critical crack length required to cause fracture. Therefore, a full-scale experimental fracture test program subjected to extreme service conditions is essential in order to properly evaluate the critical crack size for a particular detail.

In high cycle fatigue, where the behaviour is controlled by strength, lower temperatures tend to increase both the yield strength of the material and the number of cycles to failure (Suresh, 1998). Figure 2–4 shows the effects of temperature on the overall fatigue life at given stress ranges. From Figure 2–4, it can be seen that at high stress ranges and lower cycles to failure, defined as low-cycle fatigue, lower temperatures decrease the fatigue life of the material. Conversely, at lower stress ranges and higher cycles to failure (high-cycle fatigue), lower temperatures have the effect of increasing the fatigue life of the material at a given stress range.

The most practical manner in which to determine the tolerable crack size of a structural detail subject to high-cycle fatigue is to test full-scale specimens cyclically under service conditions at room temperature and then incrementally test various crack lengths under the lowest service temperatures and extreme service conditions. This general test procedure should identify the smallest critical crack length and the fewest number of stress cycles to obtain this crack length.

2.3.2 Reports on Low Temperature Tests on Full Scale Bridge Details

Low-Temperature Tests on Simulated Bridge Members

Low-temperature tests were performed on six structural members after the propagation of fatigue cracks under cyclic loading at room temperature (Schilling et al., 1975). The girders contained welded cover plate end details and welded transverse stiffener details near midspan. Half of the specimens were fabricated using A36 steel and the other half using A572 Grade 50 steel. The tests were performed under the worst loading and temperature conditions expected in similar bridge details in service. One test for each steel type was performed for more than 100 000 cycles at a stress range of 145 MPa, which the authors state is much more severe than the stresses measured in actual highway bridges. After cyclic loading was stopped, each beam was cooled to –34ºC and then loaded by a sinusoidal impulse to achieve maximum bending stresses of 140 MPa for the A36 steel specimens and 186 MPa for the A572 Grade 50 steel specimens. If failure did not occur under these conditions, stresses were then raised to 249 MPa and 350 MPa. In the specimens where failure still did not occur, the temperature was lowered further and the girders were re-stressed.

Prior to fracture, fatigue testing produced cracks in the flanges 8.9 mm deep and had essentially exhausted all of the fatigue life of these details. Even after large fatigue cracks were present in the tension flanges, the conditions required to induce fracture were temperatures lower than -30ºC and bending stress levels close to the specified minimum yield points of the respective steels. Thus, an increase in fracture toughness of these steels is unwarranted since the probability of brittle fracture occurring before exhausting the fatigue life of the details is small.

Fatigue Strength of Riveted Bridge Members

Fatigue tests on full-scale riveted girders were conducted at Lehigh University using both room temperature and temperatures as low as -73ºC (Fisher *et al.*, 1990). The tests indicated that fatigue cracks remained stable at low temperatures until they became very large. Furthermore, these results showed that the low Charpy V-notch absorbed energy levels are not critical for the strength of riveted built-up members. The fact that the results from the Charpy impact tests did not support the findings from the full-scale testing program is not surprising because of the shortcomings associated with Charpy impact tests, as previously outlined.

The fact that the critical crack size at low service temperatures is large is in agreement with the findings from tests performed on other full-scale bridge details (Schilling *et al.*, 1975; Roberts *et al.*, 1977).

Rehabilitation of Cracked Welded Steel Bridge Girders

A vertical crack 1 700 mm long was found in the web and flange of the fascia girder in the Route 95 Bridge in Providence, Rhode Island (Pullaro, 1990). All cracks were found in the vicinity of diaphragms. Further analysis indicated that out-of-plane distortion-induced fatigue was the primary cause of crack growth in the girders. Inspections of the bridge had not reported the presence of such a large crack, which seems to indicate that the fracture toughness of the material was exceeded and unstable crack propagation resulted. An inspection of the eight-span multigirder bridge was carried out after the large crack was reported. Several other smaller cracks (less than 225 mm) were found in the girders.

No full-scale tests were carried out to determine the fracture toughness or critical crack length of the complex detail. Instead, a number of samples were removed from the girders and Charpy V-notch tests were conducted. According to AASHTO requirements, the base metal in fracture critical members located in Zone 2 (minimum service temperature from -18ºC to -34ºC) must be able to absorb 33.9 J at 4ºC (Pullaro, 1990). None of the samples taken from the cracked fascia girder met these requirements.

The authors attempted to convert the CVN values to a dynamic stress intensity factor (K_{Id}), and then to a critical crack length using empirical equations. Based on the lowest measured CVN value of 6.8 J and the 34.5 MPa maximum measured stress in the web gap, the corresponding critical crack length was calculated as 196 mm. The approach adopted by the authors to determine the critical crack length is approximate for several reasons. These include the fact that Charpy impact tests do not properly simulate the conditions driving crack growth, the increase in total stress due to residual stresses was not taken into account, and the empirical model used to convert CVN values to a critical crack length is based on approximate correction factors.

The fracture surface showed no sign of shear lips, which would be indicative of ductile fracture. Propagation of the crack was observed to be by cleavage. This is typical of crack growth below the transition temperature of the material. Two porosity defects, on the order of 2 mm to 3 mm, were found at the root of the weld that connected the diaphragm bracing to the girder web. Crack growth was observed to have started at these stress raisers.

A portion of each diaphragm was cut out in order to increase the gap length and reduce the stresses in the gap region caused by the racking of the diaphragms. A noticeable upward deflection of the flange of the diaphragm was noticed during the softening process. This indicated that significant residual stresses were introduced during construction. These residual stresses, coupled with the high live load stresses in the web gap, the low CVN values, and the presence of the flaws were likely to be the cause of fracture, which likely occurred during low temperature conditions. The author believed that softening the diaphragms would relieve enough stress in the web gap so as to avoid brittle fracture. The bridge was returned to full service even though no tests simulating service conditions were conducted on the rehabilitated detail to determine the critical crack length at which fracture would be expected.

Determination of Tolerable Flaw Sizes in Welded Bridge Details

A testing program consisting of 24 full size beams with welded details was undertaken at Lehigh University to determine the degree of inspection sophistication and frequency necessary to ensure fracture safety of structures (Roberts et al., 1977). The beams were made from A36, A588, and A514 steels and the details tested included cover-plated beams, lateral attachments, transverse stiffeners, and flange transitions. All beams were cyclically loaded at room temperature for a minimum of two million cycles and then the temperature was dropped to at least -40ºC for static testing. Several fracture toughness tests were also performed on steel samples taken from the beams, but only the full-scale testing program will be discussed herein.

For the lateral attachment details and the cover plate details, fatigue testing was carried out using a stress range of 55.2 MPa at the extreme tension fiber of the beams. The test specimens with the flange transition details and with the transverse stiffeners were tested at a stress range of 124.2 MPa and 89.7 MPa at the extreme tension fiber, respectively. The maximum stress for each detail was set at approximately 55% of the specified yield strength of the respective steels.

After two million cycles, or sooner if it was felt that the fatigue crack had reached a critical size, the temperature around the cracked section was lowered to -40ºC and load cycling was continued for at least one-half hour. Fatigue tests were conducted at temperatures at or below -40ºC intermittently during the room temperature fatigue testing, until fracture occurred.

Elliptical surface cracks, with surface dimensions on the order of 12 mm or greater, formed on the tension flanges of the specimens during fatigue testing. Results of the full-scale testing program showed that the tolerable crack length at the lowest service temperature is on the order of the flange plate thickness or greater. Highly visible fatigue cracks were present in all test specimens before fracture. In several instances, temperatures significantly less than -40ºC were required to cause fracture, even after significant fatigue cracking. Nearly all of the fatigue life of each of the details had been exhausted before the crack became unstable at the lowest service temperature.

2.4 Summary of Work Reviewed

From the literature reviewed, it can be concluded that the most appropriate manner to assess the behaviour of distortion-induced fatigue cracks is to perform full-scale tests on the fatigue-prone structural detail. Both fatigue and low temperature static tests should be carried out so that the remaining life of the girders can be determined.

The in-plane girder stresses and the diaphragm racking, which induces the distortions and secondary stresses in the gap region, are the main contributing factors affecting crack growth. Knowledge of their magnitudes in service is essential so that the field conditions can be re-created during experimental testing. It should be noted that not only are the magnitude of the distortions in the web gap very small, but, like the resulting web gap stresses, they are highly dependent on the localised conditions in the gap region. Therefore, these measurements should not be used to correlate the test conditions to the field conditions. On the other hand, the diaphragm racking motions are caused by the global response of the structure and correlating these differential displacements in the lab to the field values is more practical.

In order to assess the remaining life of the girders, fatigue testing should be carried out at room temperature since the number of cycles to failure may increase as the ambient temperature decreases (Suresh, 1998). The test stress range should be representative of service conditions, but using the stress range produced by the heaviest repeated loads on the structure in service will yield safe results.

The point at which fatigue cracks reach a critical length is dependent on several parameters—temperature, stress level, and the fracture toughness of the material. Therefore, to determine the critical crack length in the girders taken from service the maximum service loads should be applied to the girders while the ambient temperature surrounding the crack is reduced to the minimum expected service temperature. Initially, fracture tests should be performed at several stages during fatigue testing so that the smallest crack length required to induce fracture under the most extreme low temperature conditions can be determined. This general test procedure should provide the smallest critical crack length and the fewest number of stress cycles to obtain this crack length.
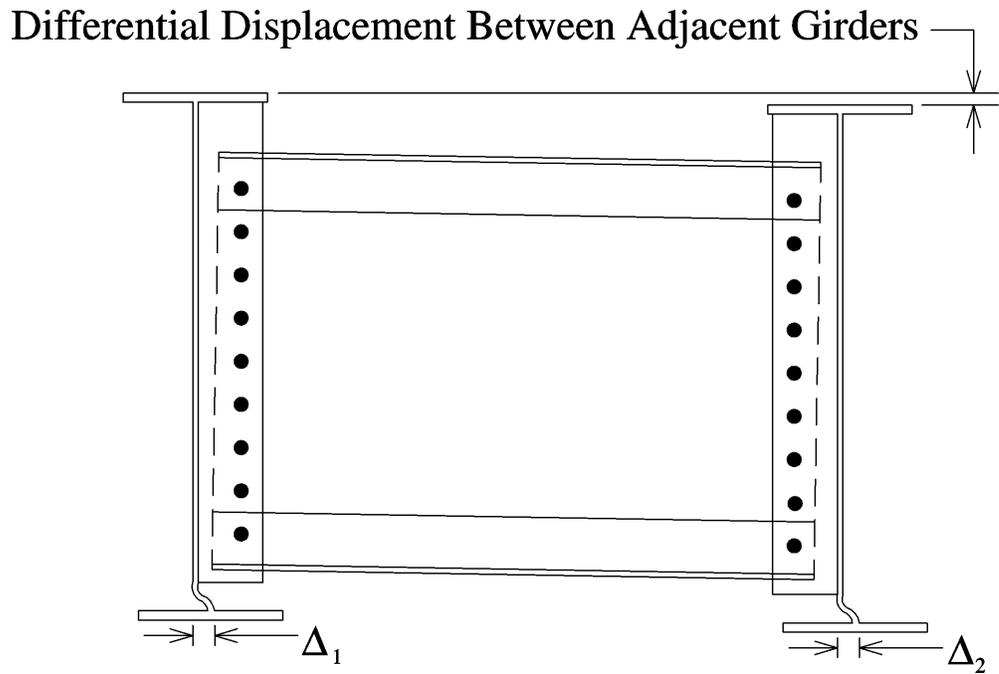
Figure 2–1 Typical Out-of-Plane Web Distortion Mode Concentrated in Web Gap
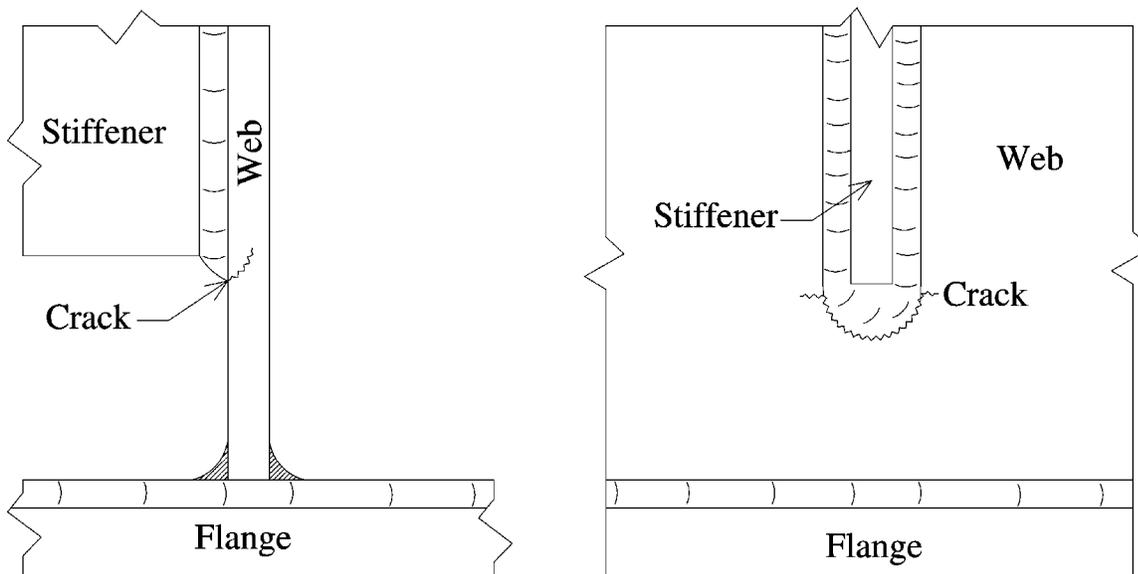
Figure 2–2 Schematic of Web Crack at End of Transverse Stiffener (Fisher, 1978)
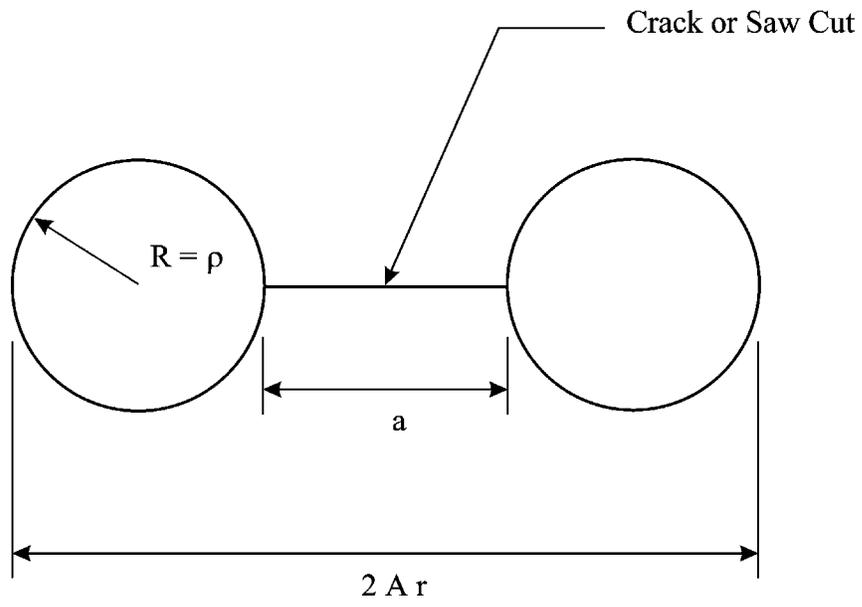
Figure 2–3 Hole Drilling Rehabilitation (Lai, 1997)
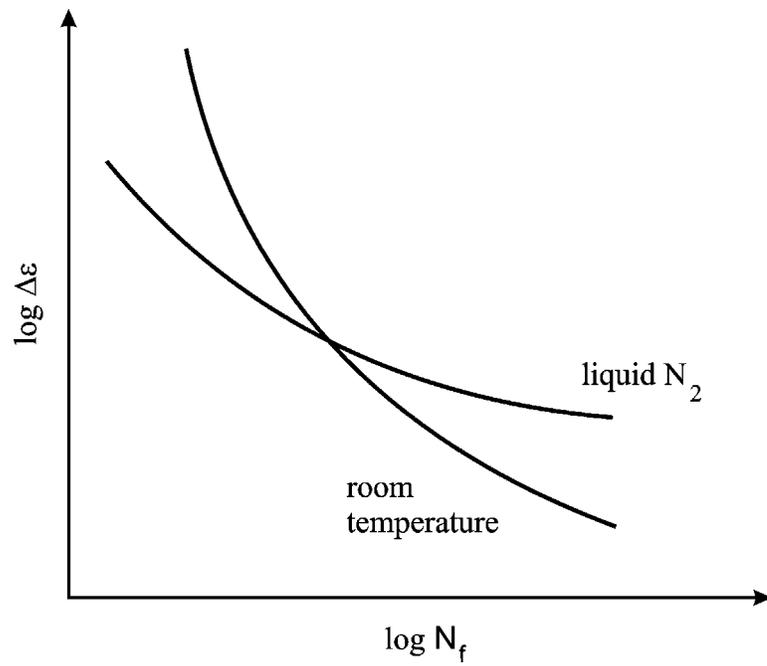
Figure 2–4 Effect of Low Temperatures on Stress-Based Total Fatigue Life

(Suresh, 1997)

CHAPTER 3

FIELD TESTING OF BRIDGE PRIOR TO DISMANTLING

3.1 Objectives of Field Monitoring Program

On August 27, 1998, University of Alberta researchers, with the co-operation of CN Rail employees, monitored the behaviour of the 9.9 m span girders under the north east main rail line (Figure 1–1 and Figure 1–2). The purpose of the field-monitoring program was to obtain the response of the superstructure to service loading so that the behaviour of the bridge could be studied and then recreated for laboratory testing.

Several aspects of the overall behaviour of the structure are important when correlating the conditions recreated in the lab to the in-situ conditions. The information collected from the bridge under service conditions included the strain distribution at a cross-section in each girder, the vertical deflection of the girders at midspan, and the web out-of-plane deformation relative to the bottom flange of the girders. The data collected were needed to determine:

- The location of the neutral axis, from which the degree of composite action between the concrete slab and the steel girders would be assessed;

- The service load effects in the girders, including bending moments and stress range;

- The live load distribution among the four girders under the north east main line;

- The vertical displacements at diaphragm positions;

- The magnitude of out-of-plane web distortion at the bottom of the transverse stiffeners to which diaphragms are bolted. These data will be compared to the magnitude of distortion measured during the laboratory-testing phase of the research.

3.2 Description of Instrumentation

Figure 3–1 shows the type and position of each instrument mounted at midspan during field-testing. Figure 3–2 is a plan view of the test span showing the position of the instrumentation along each girder.

Eight-120 ohm, 5 mm gauge length strain gauges were mounted on each girder at midspan to monitor the strain distribution over the depth of the steel section during service loading. Four strain gauges were mounted on each of the north and south faces of

each girder in order that the strain distribution over the depth of the web and out-of-plane displacement effects could be assessed. The strain data were used to establish the location of the neutral axis, from which the degree of composite action between the concrete slab and the girders was determined. The strain data were also used to establish the load effects in each girder and the live load distribution between girders. Lastly, the strain data were used in conjunction with the vertical displacement data to determine the girder displacements at each diaphragm position, from which the differential displacement between girders could be assessed. The procedure used to obtain this information is described in detail in Chapter 4.

The midspan vertical deflections of each girder were measured during the field tests using cable transducers. These displacements were measured in order to assess the differential displacement between girders at diaphragm positions and, in conjunction with the strain data, to calibrate a numerical model of the structure. Four linearly variable differential transducers (LVDTs), one on each girder, were also used to measure the relative out-of-plane deformation of the web at the base of a stiffener. These LVDTs were fixed to the top of the girder bottom flange and measured the relative displacement between the bottom flange and the web at the base of the stiffener nearest to the midspan location (Figure 3–2 and Figure 3–3).

All instrumentation was connected to a National Instruments SCXI-1100 high-speed data acquisition and data were collected using Lab View® software. For both the static and dynamic tests, all instrument channels were sampled at a rate of 1000 Hz. Excitation of the strain channels was provided by signals sent directly from the high-speed data acquisition, whereas external power supplies provided the excitation voltage for the cable transducers and LVDTs. All results and field testing data are described in Chapter 4.

3.3 Description of Field Loading and Testing

Field-testing was conducted on August 27, 1998 using two Class EF-644a locomotives (No. 2505 and 2513) provided by CN Rail. The field test consisted of both static and dynamic loading of the east 9.9 m span under the north main line. During the static test, the locomotives were moved incrementally along the span such that the leading axle of each truck was positioned at 4, 8, and 10 meters from the east abutment of the bridge. At each position, the locomotives were stopped and the strains and displacements were recorded manually at the discretion of the field testing personnel. Static tests were conducted for the locomotives advancing westbound from the east abutment and eastbound from the support pier located at the west end of the test span. Table 3–1 outlines the locations of the two locomotives during the static tests as well as the corresponding recorded reading times. Figure 3–4 shows a schematic of the locomotives

26

and indicates the axle spacing and axle numbering system employed in Table 3–1. Lastly, Figure 3–5 indicates the orientations of the instrumented girders and each of the locomotive axles during each of the static load cases performed during field-testing.

During the dynamic test the instrumentation was monitored while the locomotives advanced westward across the span at 38.6 kph (24 mph), which is close to the speed limit of 40.2 kph (25 mph) for the zone where the bridge was located. Strains and displacements were recorded continuously at a rate of 1000 Hz during the 20-second test duration. The 20 000 readings recorded were later reduced to 500 readings by averaging sets of 40 consecutive data points. Afterwards, the reduced data was plotted with the unreduced data in order to ensure that the measured response did not change as a result of the adopted data reduction procedure.

3.4 Bridge Dismantling and Removal of Girders

After field-testing was completed, the superstructure of the bridge was dismantled and replaced by the owner with a new structure. During the dismantling process, the four 9.9 m girder sets in the North Bridge were removed basically intact from the East and West spans. Then, in order to reduce the weight and size of each set the concrete deck slab and the fascia girder were removed from each set. Each of the four sets of three parallel girders, complete with attached diaphragms, were then transported off the site and stored until required for laboratory testing.

Table 3–1

Locations of Two Locomotives During Static Tests

Location	Description	Recorded Reading Times	
		Advancing West	Advancing East
0	No load (load east of span)	14:37:52 to 14:38:31	15:07:58 to 15:08:21
1	Axle 1 at meter 4	14:40:41 to 14:40:59	15:06:58 to 15:07:08
2	Axle 1 at meter 8	14:41:35 to 14:41:59	15:06:08 to 15:06:19
3	Axle 1 at meter 10	14:42:48 to 14:43:01	15:05:29 to 15:05:40
4	Axle 4 at meter 4	14:44:19 to 14:44:30	15:04:35 to 15:04:45
5	Axle 4 at meter 8	14:45:29 to 14:45:40	15:03:14 to 15:03:27
6	Axle 4 at meter 10	14:46:24 to 14:46:35	15:02:14 to 15:02:24
7	Axle 7 at meter 4	14:47:24 to 14:47:34	15:01:38 to 15:01:48
8	Axle 7 at meter 8	14:48:24 to 14:48:34	15:00:48 to 15:01:04
9	Axle 7 at meter 10	14:49:13 to 14:49:26	15:00:12 to 15:00:22
10	Axle 10 at meter 4	14:50:37 to 14:50:44	14:59:22 to 14:59:33
11	Axle 10 at meter 8	14:51:26 to 14:51:50	14:58:33 to 14:58:43
12	Axle 10 at meter 10	14:52:34 to 14:52:55	14:57:43 to 14:57:56
13	No load (load west of span)	14:54:02 to 14:54:26	
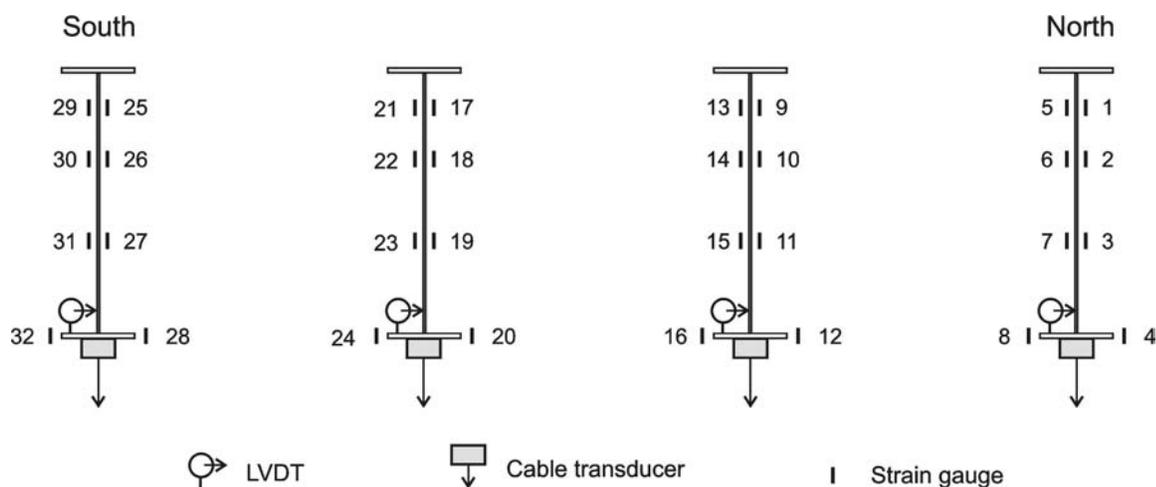
Figure 3–1 Instrumentation of Girders Under Test Span
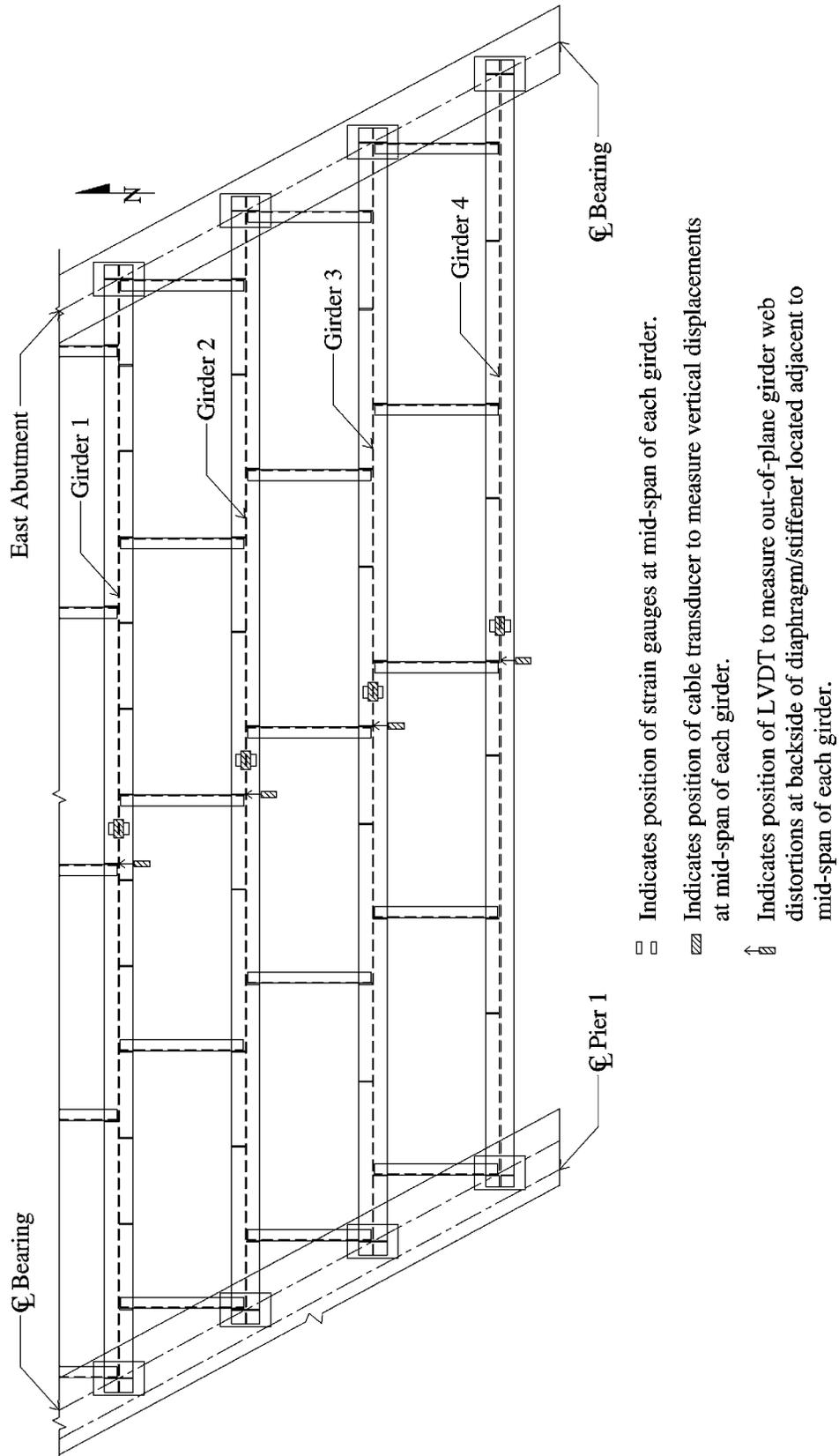
Figure 3–2 Plan View of Test Span and Field Instrumentation

Indicates position of strain gauges at mid-span of each girder.

Indicates position of cable transducer to measure vertical displacements at mid-span of each girder.

Indicates position of LVDT to measure out-of-plane girder web distortions at backside of diaphragm/stiffener located adjacent to mid-span of each girder.
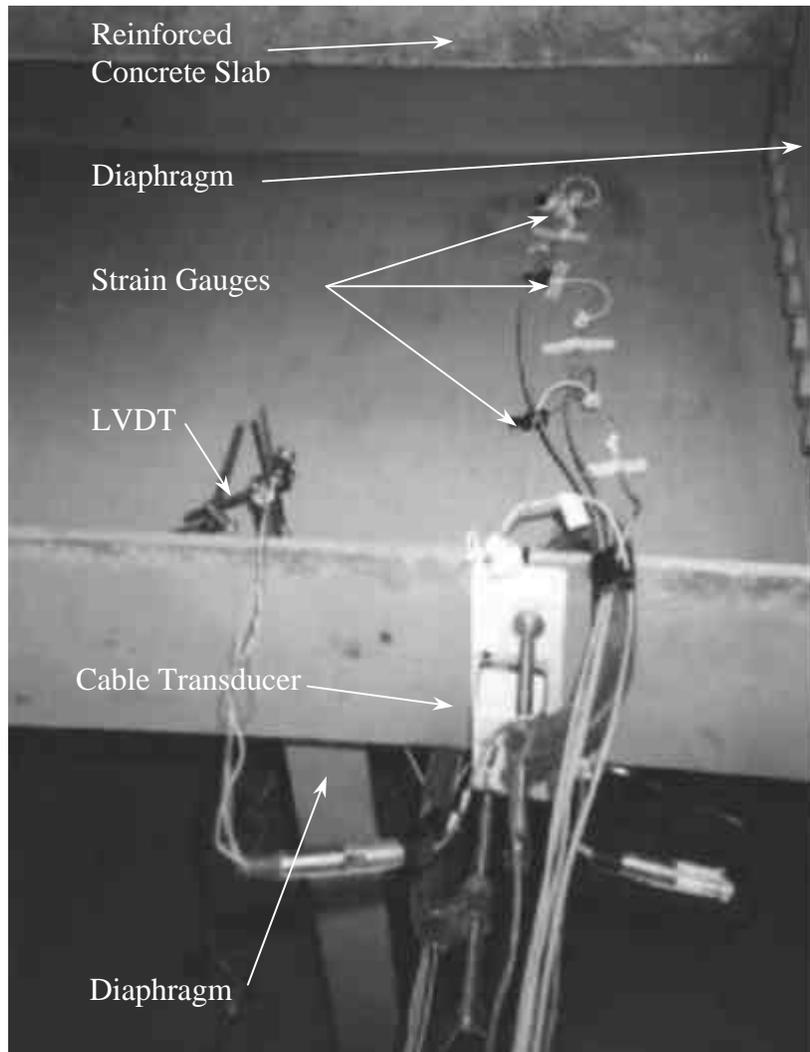
Figure 3–3 Typical Field Instrumentation at Midspan of Test Girders

Axle 1   Axle 2   Axle 3   Axle 4   Axle 5   Axle 6   Axle 7   Axle 8   Axle 9   Axle 10   Axle 11   Axle 12
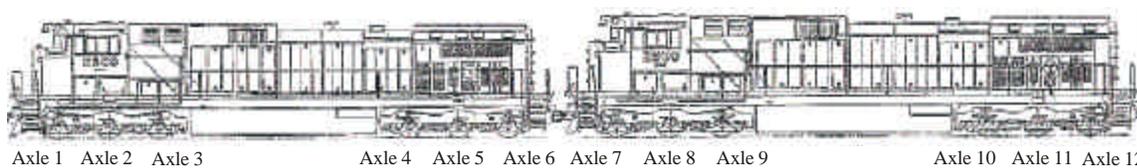
Note: All dimensions in mm

Figure 3–4 Schematic of Locomotives Provided for Field Testing Purposes

30

Static Load Case	Time		Position of Locomotive Axles
	Locomotive Advancing Westward	Locomotive Advancing Eastward	Axle 1, Axle 2, Axle 3 ... Axle 10, Axle 11, Axle 12
1	14:40:41	15:06:58	
2	14:41:35	15:06:08	
3	14:42:48	15:05:29	
4	14:44:19	15:04:35	
5	14:45:29	15:03:14	
6	14:46:24	15:02:14	
7	14:47:24	15:01:38	
8	14:48:24	15:00:48	
9	14:49:13	15:00:12	
10	14:50:37	14:59:22	
11	14:51:26	14:58:33	
12	14:52:34	14:57:43	

Figure 3–5 Position of Locomotive Axles on Test Span During Static Field Testing

CHAPTER 4

ANALYSIS AND RESULTS OF FIELD TEST DATA

4.1 Data Reduction and Drift Correction Measures

The first step in the field data reduction consisted of filtering to remove any high frequency noise, or disturbance, that was picked up from outside the electrical circuit during field testing. Possible external sources of noise include voltage surges in power lines, thermal variations, magnetic and electrostatic sources, radio-frequency EM fields, gravitational force, vibrations, humidity, etc (Fraden, 1996).

Figures 4–1 to 4–7 show the filtered strain gauge readings taken during static testing. The figures show the strain gauge readings from the gauges mounted on either the north or south face of each girder. For example, Figure 4–1 shows the entire set of static readings taken from gauge 1 through gauge 4 which, subsequently, illustrate the relative distributions of strain up the north face of girder 1 (see Figure 3–1) as the locomotives advanced along the test span. (It should be noted that the static and dynamic strain gauge data obtained from gauges 21 through 24, mounted on the south face of girder 3, are not presented herein because two of the four gauges were damaged prior to field testing.)

In Figures 4–1 through 4–7, it can be seen that when no load was present on the test span (see Table 3–1 and Figure 3–5) the strain gauge readings did not return to zero. This is due to drift, which may be thought of as ultra-low frequency noise that causes the output signal to gradually increase or decrease over time (Fraden, 1996). Drift was not significant in the displacement data because both the cable transducers and LVDTs are high voltage devices. On the other hand, strain gauges read small voltages (microvolts) and are therefore much more sensitive to drifting. In order to correct the static strain gauge data for drift, the zero load readings were plotted for each gauge and bi-linear drift versus time relationships were determined by regression analysis. Figures 4–8 through 4–11 shows both the zero readings and the bi-linear regression curves for gauges 17 through 20, respectively. It should be noted that the drift analysis for all other gauges, although not presented herein, was carried out in the same manner as for gauges 17 to 20. The drift versus time relationships were then used to correct the filtered strain gauge data. The corrected static strain measurements are presented in Figures 4–12 through 4–18. An analysis of these results is presented in section 4.2.

Figures 4–19 through 4–25 show the filtered strain gauge readings obtained during dynamic testing. As observed for the static strain data, significant drifting was present during the dynamic test. The zero load readings versus time (expressed in terms of

measurement step) were plotted for each strain gauge and drift versus time relationships were determined in the same manner as for the static strain data. Figures 4–26 through $4-29$ show the zero readings and corresponding drift versus time relationships for gauges 17 through 20, respectively. The figures present time expressed in terms of measurement step, where the time interval between each measurement step was approximately 40 milliseconds. These relationships were then used to correct the filtered dynamic strain data. The corrected dynamic strain measurements are presented in Figures 4–30 through 4–36.

4.2 Analysis of Static Field Test Data

4.2.1 Determination of the Degree of Composite Action

For each set of strain gauges mounted on the north or south face of each girder, the measured strain versus distance from the bottom flange was plotted at each static load case. Figure 4–37 and Figure 4–38 show the strain readings and associated regression line for representative static load cases for the north face of girder 3 as the locomotives moved westward and eastward on the test span, respectively. Examination of the field strain data indicates that the maximum strain recorded during the static tests was 150 με (see Figure 4–16) and that the strain distribution over the depth of the girder is linear. A least squares regression analysis therefore was performed for each set of gauges in order to determine the strain distribution over the height of each girder face and the location of the neutral axis for each static load case. Although not presented herein, the strains and distributions for all other girder faces are similar to those shown in Figures 4–37 and $4-38$.

For each static load step, the strain distribution plots indicate that as the locomotives advanced westward across the test span the measured strains are less than when the locomotives advanced eastward. In comparing the distribution results for each of the static load cases plotted in Figures 4–37 and 4–38, the difference between the west and east bound strain values can be seen clearly. This same trend was observed at all other instrumented locations. The difference in strain between the west and eastbound set of data can be attributed mainly to the variability in the positioning of the locomotive axles and the drift in the strain gauges as discussed above. Although corrections were made to eliminate the drift, some error is still expected from this source.

The location of the neutral axis in each of the four-instrumented girders was obtained for each load case. Using the method of least mean squares, which is a linear unbiased minimum-variance estimation method, the mean neutral axis position and the corresponding standard deviations were calculated for the north and south faces of the web of each girder (Mandel, 1964). A summary of the results is presented in Table 4-1.

The location of the neutral axis on the south face of girder 3 could not be accurately calculated because of problems with two of the strain gauges.

Table 4–1 shows that the location of the neutral axis is essentially the same for the interior girders (girder 2 and girder 3). Since the laboratory testing protocol tried to replicate the behaviour of the most heavily loaded interior girder, determination of a single neutral axis position from the static data was carried out using only the results from the north and south face of girder 2 and the north face of girder 3. Using the method of least mean squares and the data summarized in Table 4–1, the mean neutral axis position for an interior girder was determined to be 843 mm, measured from the bottom fiber of the girder, with a standard deviation of 2.7 mm.

For each static load step, comparisons of the strain readings on the north and south face of each girder were made and it was observed that the strains were consistently larger on one face than on the other. For girder 2, the north face strains were larger than those measured by the gauges mounted on the south face of the girder. This is illustrated in Figure 4–40 where the strain distributions on the north face (depicted by the thin regression lines) are consistently larger than the strain distributions on the south face (depicted by the bold regression lines) of girder 2. The fact that measured strains on the north face were larger than the measured strains on the south face suggests that girder 2 was subjected to lateral bending when the bridge was loaded. The same type of response was observed in girder 1 as shown in Figure 4–39. Girder 4, on the other hand, was subjected to less lateral bending when the bridge was loaded since the difference in the north and south face strains were notably smaller. Furthermore, the lateral bending present in girder 4 was in the opposite direction to the lateral bending in girder 1 and girder 2. This is evidenced by the fact that the measured south face strains in girder 4 were higher than the strains on the north face (Figure 4–41). It should be noted that similar observations could not be made for girder 3 since the south face strain data was disregarded because of a malfunction of the strain gauges.

4.2.2 Lateral Load Distribution

Since the bridge was built on a 28° RHF skew, determining the live load distribution between the girders was not as simple as comparing midspan moments or midspan vertical displacements. Instead, the equivalent concentrated loads resisted by each girder in the test span were determined for each static load case. This approach is adopted because in a skew bridge a load applied in a vertical plane transverse to the bridge will load each girder at a different location along their span. As a result, even though the midspan effects in each girder were significantly different, the actual load resisted by each girder was similar.

At each static load step, the position of the locomotive axles on each girder span was determined. This was accomplished by assuming that the axle loads were distributed down through the rails, rail ties, gravel bed, and concrete deck and into the girders in a transverse vertical plane located at each axle position. Since the measured strains were only in the order of 150 $\mu\varepsilon$, it was concluded that the girders were responding elastically in service. For each load case, the calculated neutral axis positions were used in conjunction with the girder dimensions and slab depth to determine the effective width of concrete acting compositely with the steel girders. Knowing the effective width of concrete, the composite moment of inertia and elastic section modulus were calculated for each girder. The strain distribution regression results were used to calculate the bottom fiber strains on the north and south faces of each girder for each load case. For each girder, the bottom fiber strains on each face were averaged in order to eliminate the effects due to lateral bending and obtain the response due to in plane bending only. The bottom fiber in plane bending strains in each girder were then converted into stresses and multiplied by the elastic section modulus to obtain the midspan bending moments resisted by each girder during each static load case. Knowing the girder midspan moments and the load positions on each girder, the equivalent concentrated loads resisted by each girder were determined for each load case. Initially, the calculation of these loads was carried out by assuming that each girder was a solitary simple span member and that the diaphragms did little in terms of load distribution. This assumption was verified when the test span was modelled using the structural analysis program S-Frame®.

Table 4–2 summarises the results of the lateral load distribution calculations from the static field test data. Since the weight of the locomotives is assumed to be equally distributed to each axle, the table shows the magnitude of the concentrated load resisted by each girder at a single locomotive axle position on the test span. At certain static load cases the vertical axle planes on the instrumented bridge structure did not intercept all of the girder spans because of the 28º RHF skew. Consequently, the only static load cases considered in the determination of the live load distribution were those in which the vertical axle planes intercepted all four girder spans. Results of the static live load distribution analysis show that the percentage of total load resisted by each girder is 16.3% for girder 1, 23.2% for girder 2, 31.4% for girder 3, and 29.1% for girder 4. Since the total load resisted by all girders at a single vertical axle plane (Table 4–2) was significantly less than a single locomotive axle load (approximately 250 kN), significant load distribution between adjacent structures and possibly a significant contribution from the rails must have been present.

4.3 Analysis of Data from the Dynamic Field Test

4.3.1 Degree of Composite Action

Several representative dynamic load cases were selected from the field test and the measured strain distributions in the girders were plotted. Linear regression analysis was performed on each set of strain readings to determine the response of each girder to service loading. Figure 4–42 shows both the strain readings and the regression lines for several of the dynamic load steps analysed for the north face of girder 3. Although not presented in this report, the strain distribution results for all other girders were also obtained and were found to be similar to those presented for girder 3.

For each dynamic load case analysed, the strain distributions were used to determine the location of the neutral axis for each of the girder faces (Table 4–3). As observed during the static tests, the north face strains were larger than the south face strains in girder 1 and girder 2 at each dynamic load step. This indicates that some lateral bending was present in the girders because of the action of the diaphragms. Also, the south face strains in girder 4 were larger than the north face strains, indicating that the lateral bending force resisted by girder 4 was in the opposite direction of the lateral bending forces resisted by girder 1 and girder 2. The results obtained from the vertical deflections, measured by the cable transducers at midspan of each girder, support this observation. Midspan vertical displacement measurements indicate that the maximum deflection at each load step was in girder 3, followed by girder 2, then girder 4, and finally girder 1 (Figure 4–43). The resulting differential displacements produce out-of-plane moments in the girders at the diaphragm locations. Hence, the strains measured on the south face of girder 4 should be higher than the north face strains, and vice-versa for girder 1 and girder 2.

As was the case for the static tests, the determination of a single neutral axis position from the dynamic data was carried out using only the results from the north and south faces of girder 2 and the north face of girder 3. Using the method of least squares and the data summarised in Table 4–3, the mean neutral axis position for an interior girder was determined to be 868 mm, measured from the bottom fiber of the girder, with a standard deviation of 2.5 mm. Both the static and dynamic results for the north and south face of girder 2 and the north face of girder 3 were then combined using the method of least mean squares to determine a linear unbiased minimum-variance estimation of the position of the neutral axis of an interior girder. For a typical interior girder, the neutral axis was 847 mm from the bottom fiber, with a standard deviation of 2.5 mm.

From the measured position of the neutral axis, the concrete slab properties, and girder and slab dimensions outlined in the structural drawings of the bridge, the moment of inertia of the composite section was determined. A summary of the moment of inertia

calculations for the composite section is presented in Table 4–5. The moment of inertia of the composite section was determined to be 6 240×106 mm4.

The theoretical position of the neutral axis and composite moment of inertia were calculated and compared to the values obtained from the field test data. For the purpose of this analysis, 100% composite action between the girder and slab was assumed and the theoretical effective width of the concrete slab was determined based on the provisions of Clause 17.4 of CAN/CSA-S16.1-94 (CSA, 1994). The theoretical position of the neutral axis was determined to be 853 mm from the girder bottom fiber, which is only 0.71% different from the position determined from the field test data. The theoretical composite moment of inertia was determined to be $6\ 300{\times}10^{6}$ mm^{4}, or 1.06% greater than the moment of inertia obtained from the field test results. Table 4–5 summarises the calculation of the theoretical moment of inertia of a typical interior girder.

4.3.2 Lateral Load Distribution

In order to determine the lateral load distribution between girders from representative dynamic load steps, the same procedure outlined for the static data was adopted (Section 4.2.2). As for the static tests, only those dynamic load steps in which the vertical axle planes on the bridge structure intercepted all four girders were considered in the analysis. Table 4–4 summarises the lateral load distribution results calculated from the dynamic field test data. Results of the lateral load distribution analysis show that the percentage of total load resisted by each girder is 16.5% for girder 1, 25.7% for girder 2, 30.1% for girder 3, and 27.8% for girder 4. Comparison between the static and dynamic load distribution shows a good correlation.

4.3.3 Differential Displacements Between Adjacent Girders at Diaphragm Positions

Since adjacent girders deflect by different amounts under train loading, the differential movement produces a racking motion of the diaphragms, resulting in out-of-plane deformation in the web gaps that exist at the lower ends of the stiffeners (Fisher *et al.*, 1998). These relatively small deformations can produce large local strains in the web and are the source of the fatigue cracks that formed in the girders prior to bridge dismantling. Therefore, knowledge of the magnitudes of the differential displacements that cause these deformations is an important parameter when duplicating the field conditions in the laboratory.

In order to assess the differential displacements between girders at diaphragm positions, a numerical model of the test span was created using the structural analysis program S-Frame®. The geometry of the structure was modelled using the information presented on the structural drawings of the bridge and the girders and diaphragms were both

modelled as beam elements. With the exception of the girder neutral axis position and composite moment of inertia, the section and material properties for both elements were calculated based on information presented on the structural design drawings of the bridge. The cross-section used for the composite girder elements was selected so that the centroid and moment of inertia would be as calculated from the field test data. Channel sections with the same properties as the diaphragm sections were used to model the diaphragm members. Figure 4–45 shows a plan view of the model.

Since it was intended that laboratory testing would simulate the behaviour of an interior girder under the maximum loading conditions measured during the field test, the load cases analysed in S-Frame® were obtained from the dynamic load cases that created maximum effects in girder 3. The equivalent concentrated axle loads resisted by each girder and the corresponding axle positions were determined and applied to the model. The results of the analysis showed that both the bottom fiber stress and midspan vertical displacements were in good agreement with the field test data (Table $4-6$). With the model calibrated to the results of the field test data, the respective girder displacements were obtained and the differential displacements between adjacent girders at each diaphragm location were calculated. Table 4–7 lists the displacement results as well as the calculated differential displacements. In Table 4–7, only the displacements for girder 2, girder 3 and girder 4 are tabulated since these displacements are the ones required to calculate the differential displacements at the diaphragms connected to girder 3.

4.3.4 In-Plane Nominal Stress Range

The stress range at the bottom fiber of girder 3 was determined from the field dynamic test. Figure 4–44 presents a simplified plot of the bottom fiber stress versus time step for the north face of girder 3. The results obtained from the reservoir counting analysis are presented in Table 4–8. Table 4–8 shows that girder 3 underwent four cycles of stress as the locomotives advanced across the test span with stress ranges varying from 35 MPa to 14 MPa.

4.3.5 Out-of-Plane Web Distortions Near Midspan of Girders

Figure 4–46 shows the LVDT measurements recorded during dynamic testing. The measured out-of-plane web distortions, relative to the girder bottom flanges, were very small. For each girder, the data indicates that non-zero measurements started when the first set of axles made its way onto the test span (at around measurement step 200) and did not return to zero after the locomotives moved west of the structure. At the time of field testing, varying degrees of girder web cracking were present at each instrumented position and the results suggest that after the loads left the span the steel above and below

the cracked surfaces did not return to their original positions. The measured distortions were found to be similar in magnitude for girder 1 (approximately 0.0009 mm), girder 2 (approximately 0.0008 mm), and girder 4 (approximately 0.0021 mm). However, for Girder 3 shortly after the locomotives advanced westward onto the span, at approximately load step 210, the measured distortion increased suddenly from 0.0012 mm to 0.0225 mm. Since slippage of the mounted instruments is unlikely, then it is possible that the force created at the lateral crack, located at the instrument position on Girder 3, was large enough to overcome the maximum achievable static friction force. If this occurred, then it is likely that slippage between the two surfaces would occur almost instantaneously, as the LVDT measurement results indicate. Observations of the degree of cracking in the webs at the instrumented diaphragm locations showed that the extent of cracking in Girder 3 was more severe than in the other girders. Hence, instantaneous slip only occurring at the LVDT mounted near midspan of Girder 3 is plausible.

Figure 4–47 shows the out-of-plane web distortions measured by the LVDTs mounted near midspan of each girder during static testing. By comparing Figures 4–46 and 4–47, it can be seen that the static responses are different from the responses measured during dynamic field testing. During static testing, the out-of-plane web distortions measured in each girder increased or decreased depending on the location of the axles on the test span. From the dynamic measurements the distortions were independent of axle locations since the distortions essentially remained constant throughout the test except when instantaneous slip of the crack surfaces occurred in girder 3. The relationship between axle positions and out-of-plane web distortions, observed during static field testing, is most prevalent in girder 3. From Figure 4–47 and Figure 3–5, it can be seen that the measured distortions in girder 3 were maximised when a set of axles was positioned along vertical planes near the girder midspan and decreased significantly when the axles were located near the ends of the girder span. Like the distortions measured during dynamic testing, the LVDT static measurements did not return to zero when no axles were present on the test span. This again suggests that the steel above and below the crack surfaces did not return to their original positions after the loads left the span.

The variability in the out-of-plane web distortion measurements recorded during the dynamic and static field tests can be attributed to the presence of the cracks in the web where the LVDTs were located (see Figure 3–3). When load was applied to the test span, slippage of the surfaces above and below the cracks either occurred suddenly, gradually or not at all depending on the size, position and roughness of the crack surfaces. This variability makes it difficult to draw comparisons between the measurements taken at each girder and between the static and dynamic measurements taken at any single girder.

Comparisons between the out-of-plane web distortions measured during field testing and during the laboratory-testing phase are presented in Chapter 6.

Table 4–1

Location of Neutral Axis Based on Static Strain Gauge Data

Girder Face	Distance from the Bottom Fiber to the Neutral Axis (mm)	Standard Deviation (mm)
Girder 1 North	952	6.8
Girder 1 South	856	7.1
Girder 2 North	834	6.3
Girder 2 South	863	4.6
Girder 3 North	833	3.9
Girder 4 North	824	4.9
Girder 4 South	977	3.1

Table 4–2

CALCULATED LIVE LOAD DISTRIBUTION BASED ON STATIC FIELD TEST DATA

Load Step[†]	Calculated Girder Load (kN)				Total Load (kN)	Live Load Distribution Ratios				Sum of Ratios
	Girder 1	Girder 2	Girder 3	Girder 4		Girder 1	Girder 2	Girder 3	Girder 4	
2W	18.4	25.7	32.6	27.3	104.0	0.177	0.247	0.313	0.262	1.000
3W	22.9	27.6	39.8	29.1	119.4	0.192	0.231	0.333	0.244	1.000
8W	17.3	25.5	33.4	30.0	106.3	0.163	0.240	0.315	0.282	1.000
9W	15.0	19.5	32.4	28.0	94.8	0.158	0.206	0.341	0.295	1.000
11W	16.2	26.8	33.9	30.5	107.5	0.151	0.249	0.315	0.284	1.000
12W	18.6	26.6	39.0	36.5	120.8	0.154	0.220	0.323	0.302	1.000
2E	23.9	34.8	41.6	41.1	141.4	0.169	0.246	0.294	0.291	1.000
3E	26.7	34.9	46.9	52.0	160.5	0.166	0.218	0.292	0.324	1.000
8E	18.6	29.4	36.1	34.5	118.7	0.157	0.248	0.304	0.291	1.000
9E	19.3	27.8	36.7	37.3	121.1	0.159	0.230	0.303	0.308	1.000
11E	17.4	27.6	34.2	32.1	111.3	0.157	0.248	0.307	0.288	1.000
12E	14.7	19.6	30.5	29.9	94.6	0.155	0.207	0.322	0.316	1.000
					Average:	*0.163*	*0.232*	*0.314*	*0.291*	*1.000*

[†] Load step number indicates the position of locomotive axles as described in Table 3–1, whereas W/E indicates whether locomotives were advancing westward or eastward across test span.

Table 4–3

NEUTRAL AXIS POSITION RESULTS BASED ON DYNAMIC STRAIN GAUGE DATA

Girder Face	Distance from the Bottom Fiber to the Neutral Axis (mm)	Standard Deviation, (mm)
Girder 1 North	937	7.1
Girder 1 South	829	16.3
Girder 2 North	821	15.0
Girder 2 South	895	8.8
Girder 3 North	850	11.3
Girder 4 North	857	16.7
Girder 4 South	973	6.0

Table 4–4

Live Load Distribution Results Based on Dynamic Field Test Data

Load Step	Calculated Girder Load (kN)				Total Load (kN)	Live Load Distribution Ratios				Sum of Ratios
	Girder 1	Girder 2	Girder 3	Girder 4		Girder 1	Girder 2	Girder 3	Girder 4	
184	26.5	39.6	46.0	45.8	157.9	0.168	0.251	0.291	0.290	1.000
213	22.6	36.7	39.1	36.2	134.6	0.168	0.273	0.291	0.269	1.000
232	23.2	34.6	40.9	38.4	137.2	0.169	0.252	0.298	0.280	1.000
234	23.1	35.5	42.0	38.1	138.6	0.166	0.256	0.303	0.275	1.000
262	20.4	33.2	40.5	36.4	130.5	0.157	0.254	0.310	0.279	1.000
264	21.3	33.6	41.5	36.1	132.5	0.161	0.254	0.313	0.272	1.000
					Average:	*0.165*	*0.257*	*0.301*	*0.278*	*1.000*

Table 4–5

Properties of Composite Section

Composite Section	Field Data	Theoretical
Modular ratio (n=E_s/E_c)	10.18	10.18
Concrete Thickness (mm)	268	268
Transformed Concrete Width (mm)	1 100	1 143
Transformed Concrete Area (mm^2)	294 800	306 324
Equivalent Area of Steel (mm^2)	28 959	30 091

Composite Neutral Axis	(measured from girder bottom fiber)	
A_{girder} (mm^2)	16 774	16 774
A_{total} (mm^2)	45 733	46 865
Concrete: A $\bar{y}$ (mm^3)	30 820 990	32 025 099
Girder: A $\bar{y}$ (mm^3)	7 935 360	7 935 360
ΣA $\bar{y}$ (mm^3)	38 756 150	39 960 459
$\bar{y}$ (mm)	847	853

Composite Moment of Inertia		
Girder: ($\times 10^6$ mm^4)	2 352	2 352
Girder: A($\bar{y}$)^2 ($\times 10^6$ mm^4)	2 351	2 417
Concrete: ($\times 10^6$ mm^4)	173	180
Concrete: A($\bar{y}$)^2 ($\times 10^6$ mm^4)	1 361	1 347
ΣI_x ($\times 10^6$ mm^4)	6 238	6 296

Table 4–6

Calculated and Measured Mid-Span Bottom Fiber Stresses and Displacements

	Field Test Results		Numerical Model Results	
	Bottom Fiber Stress	Vertical Displacement	Bottom Fiber Stress	Vertical Displacement
Girder	(MPa)	(mm)	(MPa)	(mm)
1	18.2	-0.742	16.6	-0.962
2	26.1	-1.403	24.8	-1.415
3	29.8	-1.696	30.0	-1.689
4	25.0	-1.378	25.0	-1.431

Table 4–7

GIRDER DISPLACEMENTS AT DIAPHRAGM

LOCATIONS

| Joint | Vertical Displacement (mm) | Differential Displacements | |
		Designation	Displacement (mm)
2	-0.2696		
		$\Delta_{2\text{-}7}$	-0.2696
7	0.0000		
3	-1.1309		
		$\Delta_{3\text{-}9}$	-0.0005
9	-1.1314		
4	-1.4307		
		$\Delta_{4\text{-}11}$	-0.2497
11	-1.6804		
5	-0.9826		
		$\Delta_{5\text{-}13}$	-0.3733
13	-1.3559		
6	0.0000		
		$\Delta_{6\text{-}15}$	-0.3271
15	-0.3271		
8	-0.3269		
		$\Delta_{8\text{-}17}$	-0.3269
17	0.0000		
10	-1.3556		
		$\Delta_{10\text{-}18}$	-0.3835
18	-0.9721		
12	-1.6805		
		$\Delta_{12\text{-}19}$	-0.2658
19	-1.4147		
14	-1.1318		
		$\Delta_{14\text{-}20}$	-0.0142
20	-1.1176		
16	0.0000		
		$\Delta_{16\text{-}21}$	0.2663
21	-0.2663		

* Refer to Figure 4–45 for joint locations.

Table 4–8

RESERVOIR COUNTING STRESS CYCLE RESULTS

Drain From Trough No.	Water Level at Peak	Stress Range (MPa)
7	2	34.9
3	4	30.2
5	6	14.1
9	8	33.1
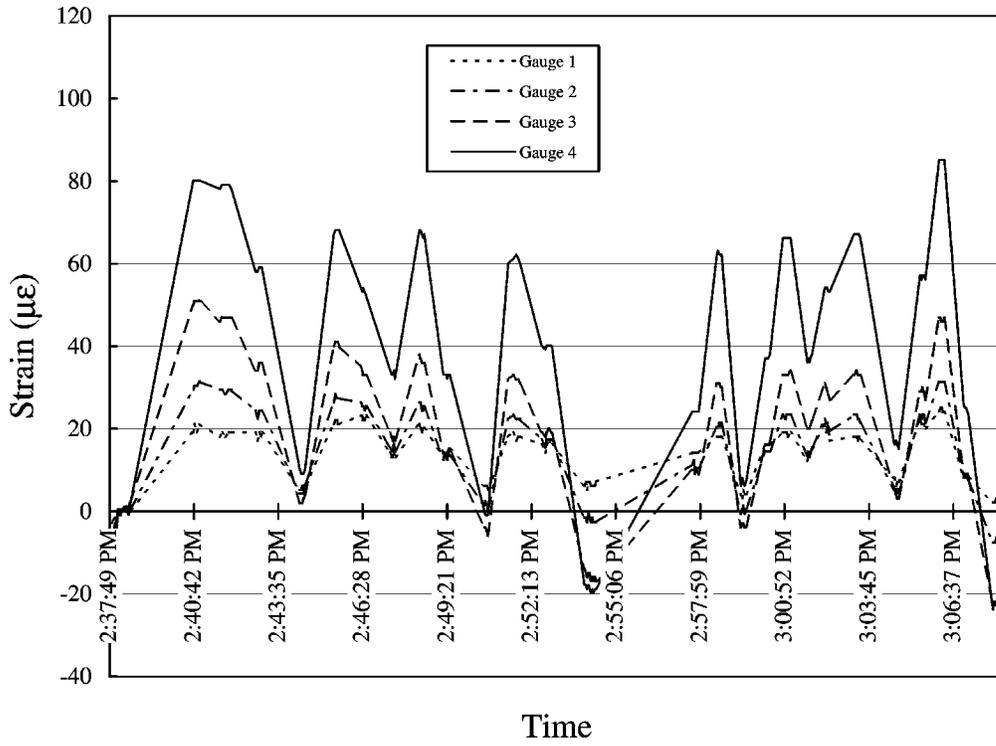
Figure 4–1 Measured Static Strain vs. Time Step – Gauges 1 Through 4, Girder 1 North
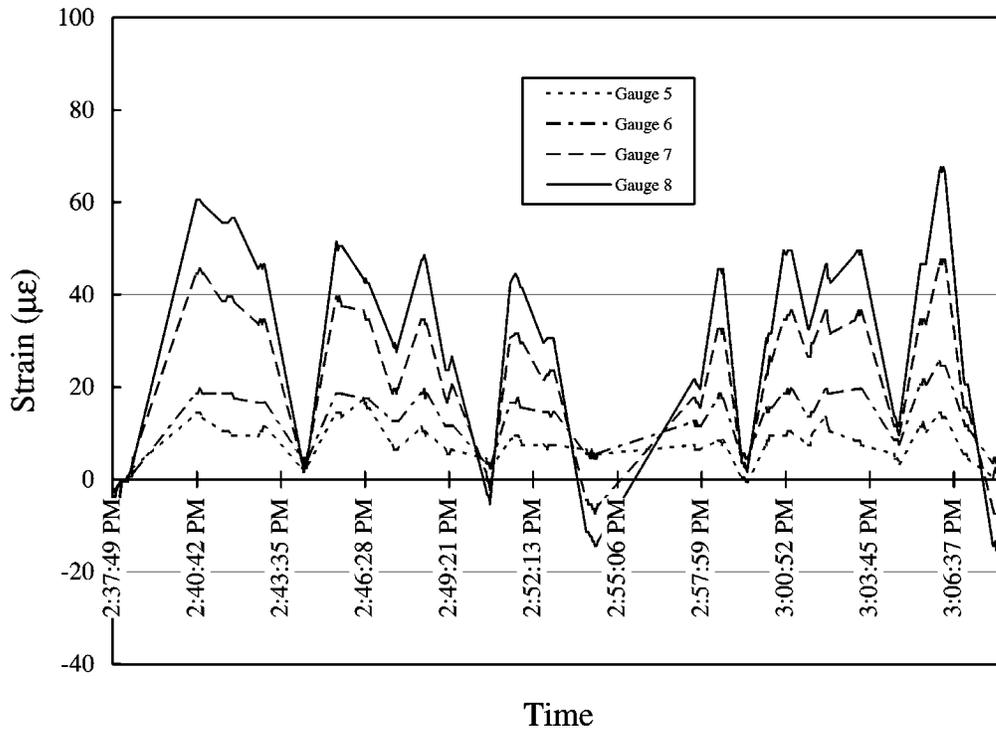
Figure 4–2 Measured Static Strain vs. Time Step – Gauges 5 Through 8, Girder 1 South

46
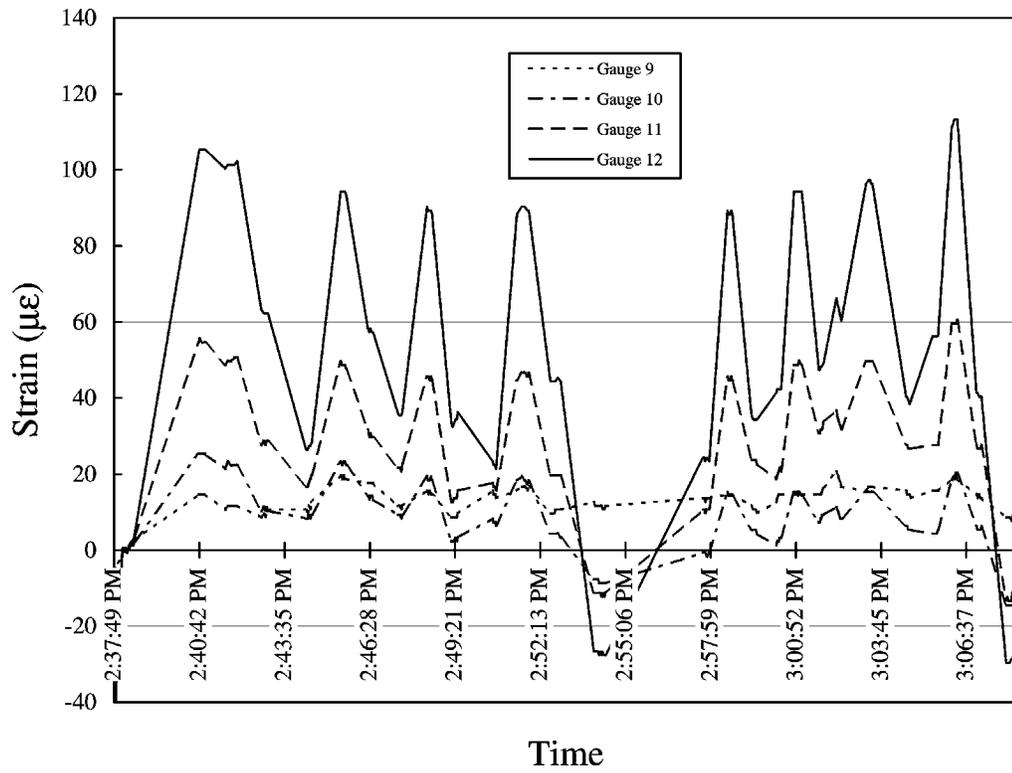
Figure 4–3 Measured Static Strain vs. Time Step – Gauges 9 Through 12, Girder 2 North
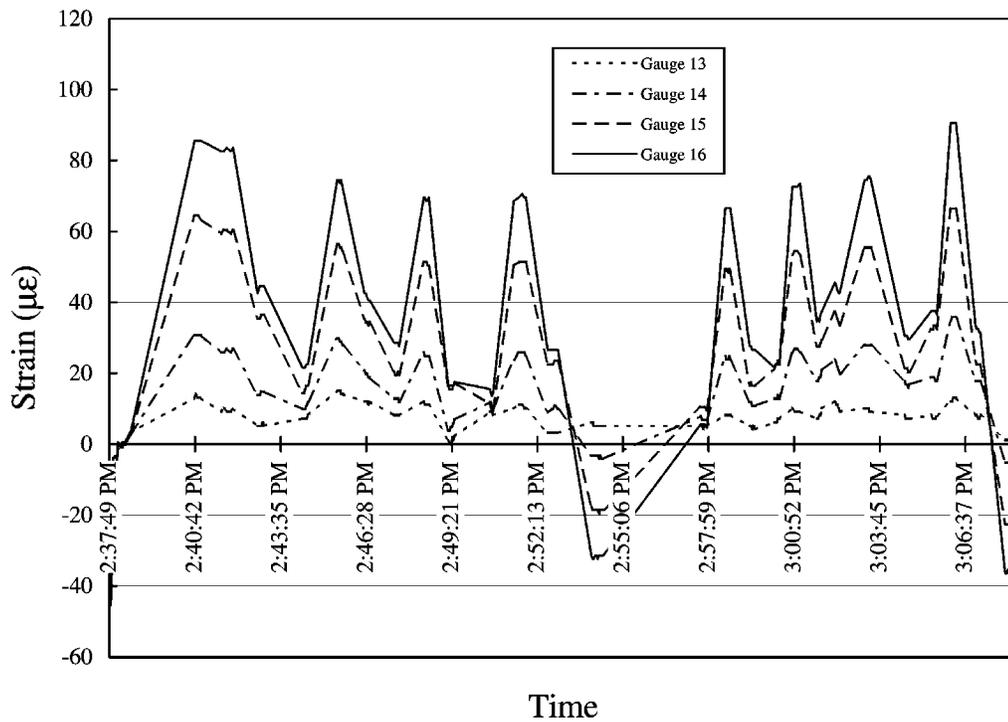
Figure 4–4 Measured Static Strain vs. Time Step – Gauges 13 Through 16, Girder 2 South

47
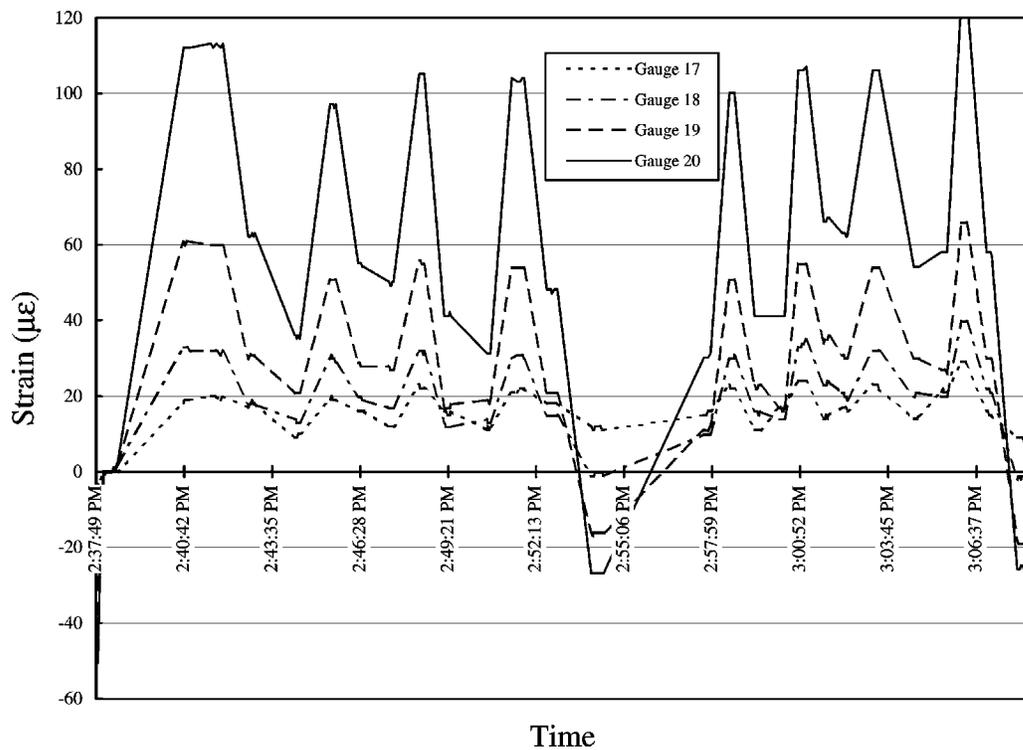
Figure 4–5 Measured Static Strain vs. Time Step – Gauges 17 Through 20, Girder 3 North
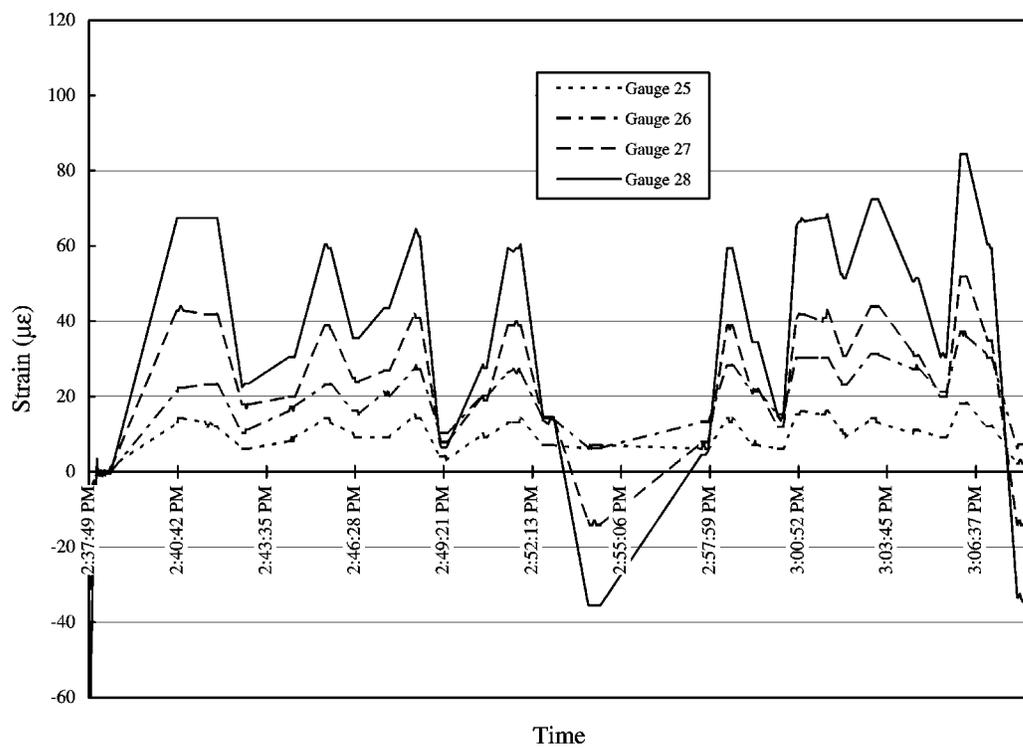
Figure 4–6 Measured Static Strain vs. Time Step – Gauges 25 Through 28, Girder 4 North

48
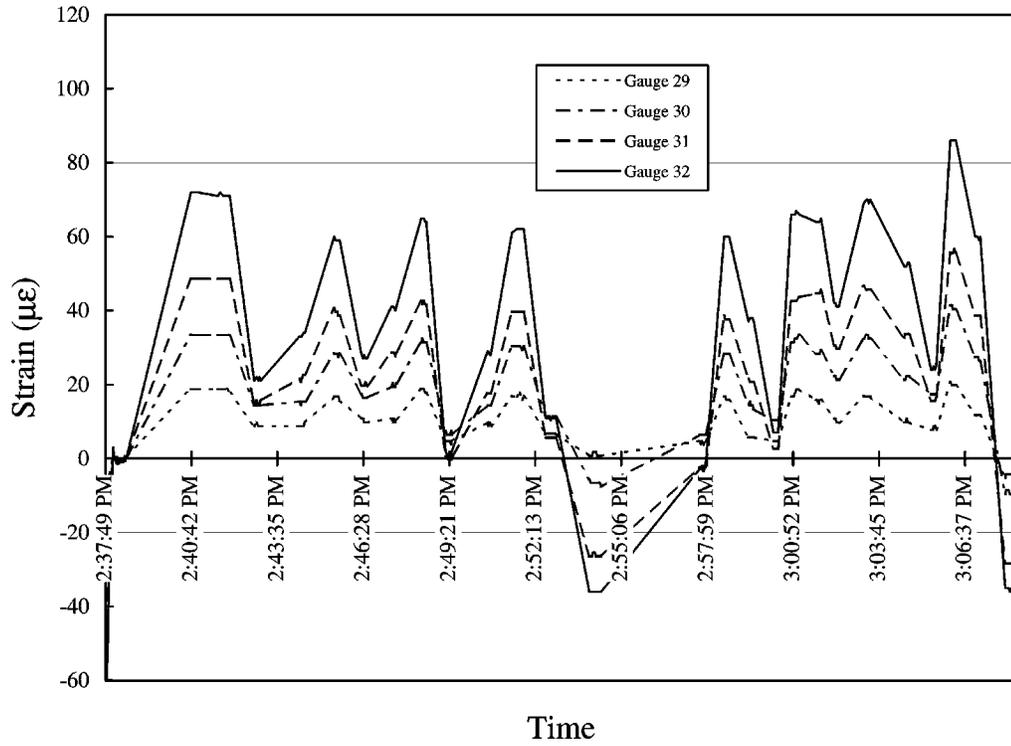
Figure 4–7 Measured Static Strain vs. Time Step – Gauges 29 Through 32, Girder 4 South
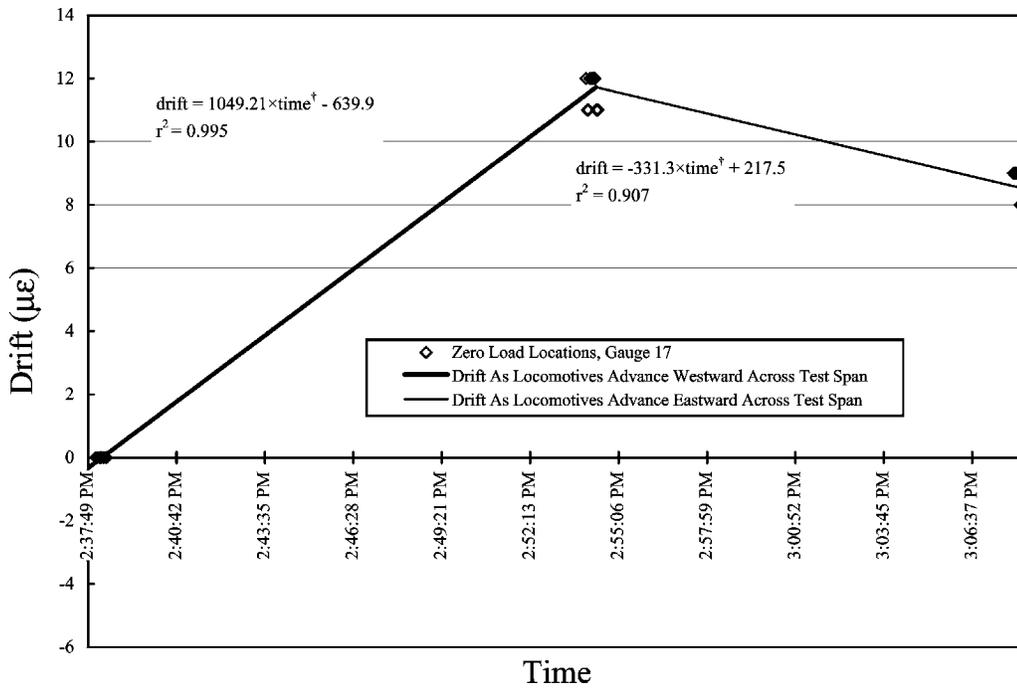
† Time expressed as a fraction of 24 hours

Figure 4–8 Drift vs. Time Step, Gauge 17

drift = -190.4×time† - 117.1
r² = 0.264

drift = 187.9×time† + 116.6
r² = 0.436

Zero Load Locations, Gauge 18
Drift As Locomotives Advance Westward Across Test Span
Drift As Locomotives Advance Eastward Across Test Span
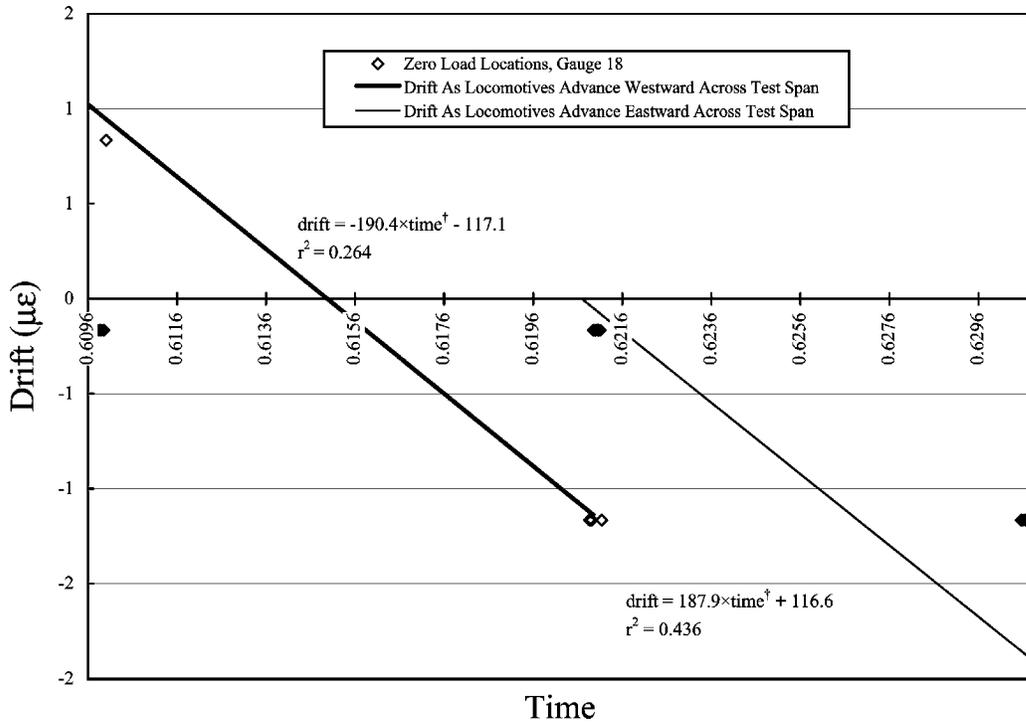
† Time expressed as a fraction of 24 hours

Figure 4–9 Drift vs. Time Step, Gauge 18

drift = -1467.2×time† - 894.9
r² = 0.997

drift = -278.3×time† + 156.7
r² = 0.889

Zero Load Locations, Gauge 19
Drift As Locomotives Advance Westward Across Test Span
Drift As Locomotives Advance Eastward Across Test Span
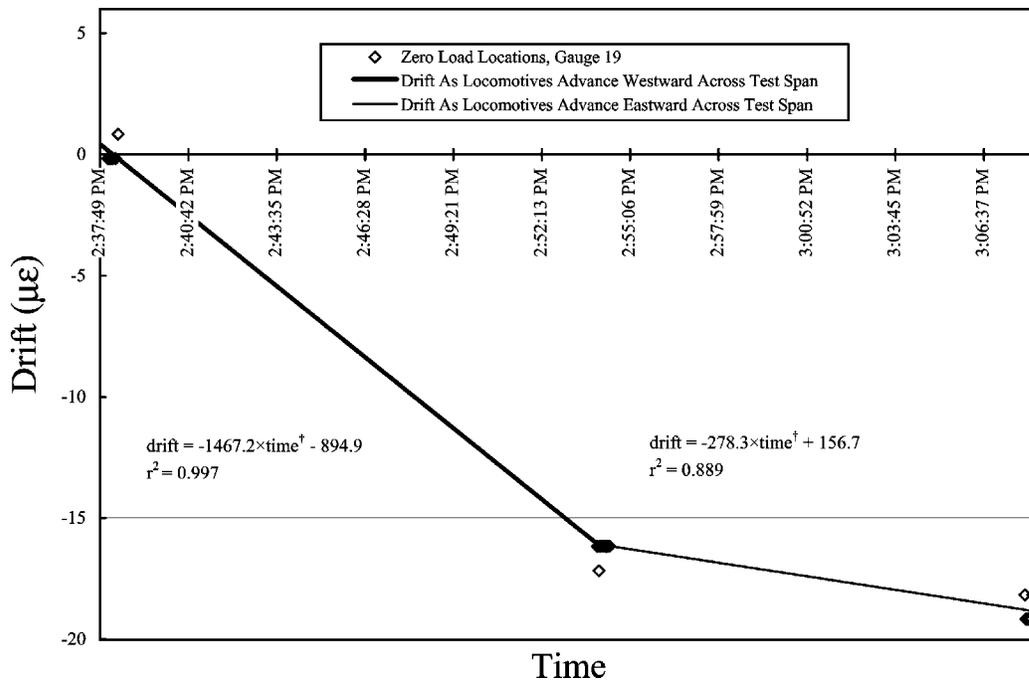
† Time expressed as a fraction of 24 hours

Figure 4–10 Drift vs. Time Step, Gauge 19

drift = -2416.2×time† - 1473.6
r² = 0.9993

drift = 167.7×time† - 131.1
r² = 0.802
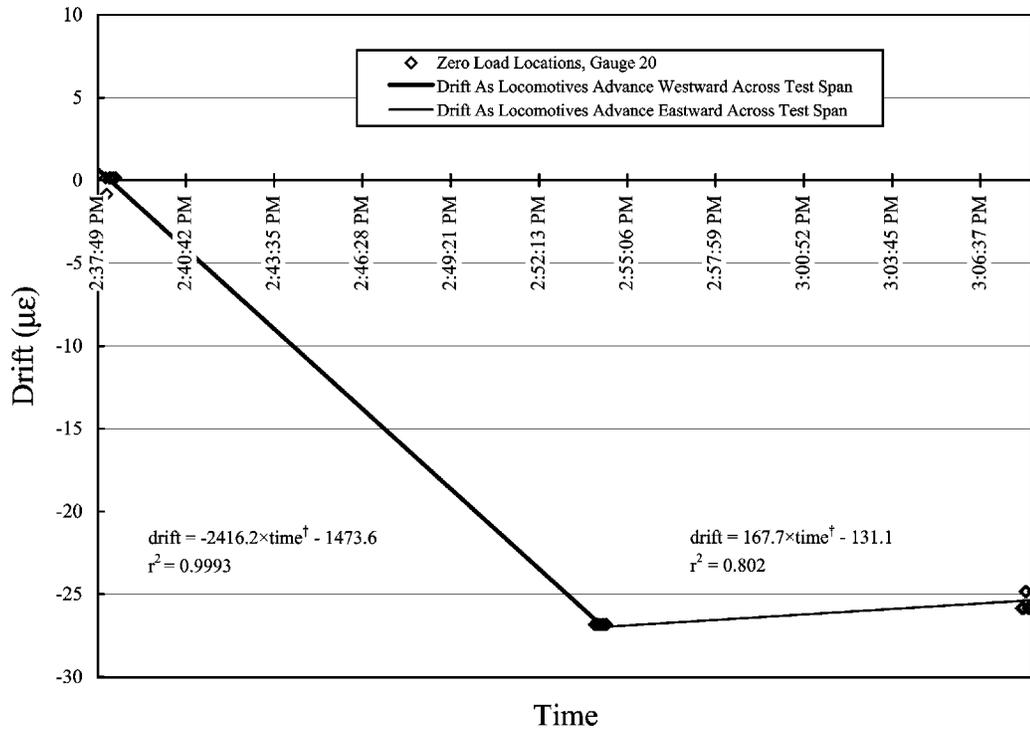
† Time expressed as a fraction of 24 hours

Figure 4–11 Drift vs. Time Step, Gauge 20
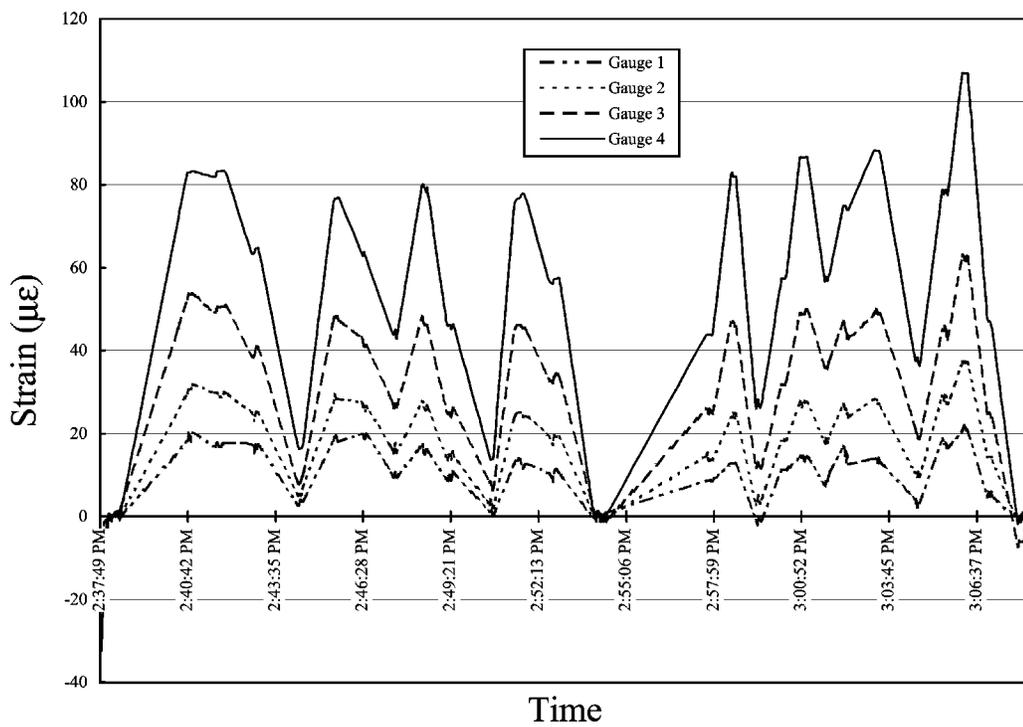
Figure 4–12 Revised Static Measurements, Gauges 1 Through 4, Girder 1 North

51
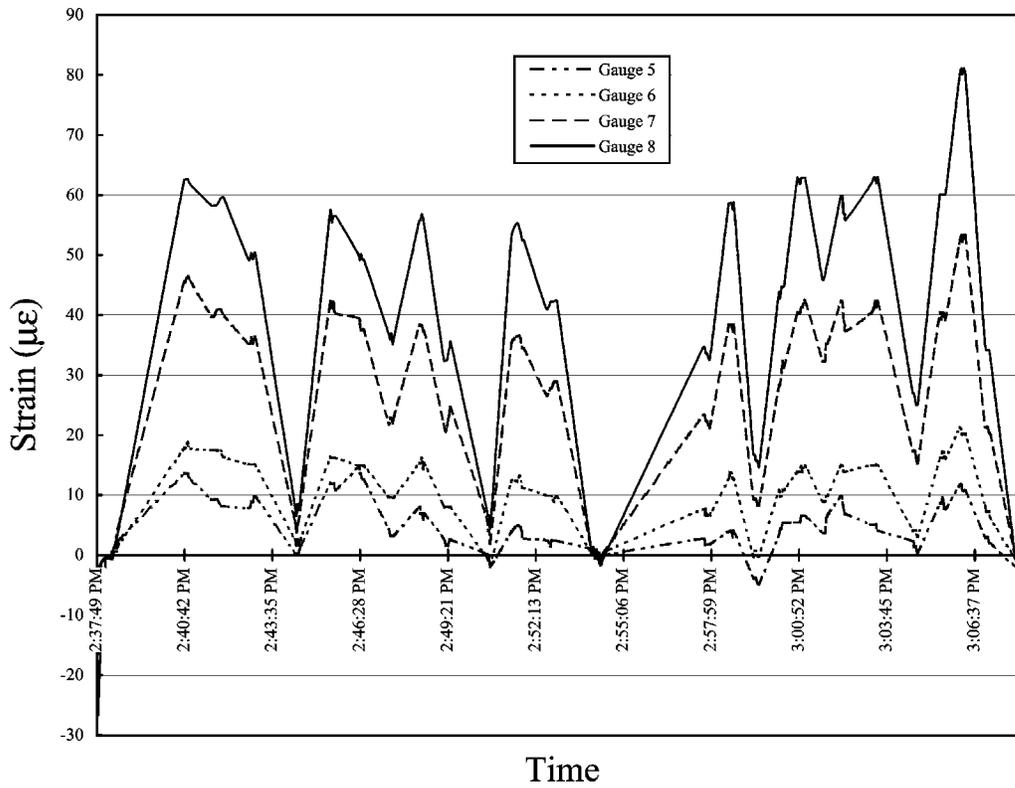
Figure 4–13 Revised Static Measurements, Gauges 5 Through 8, Girder 1 South
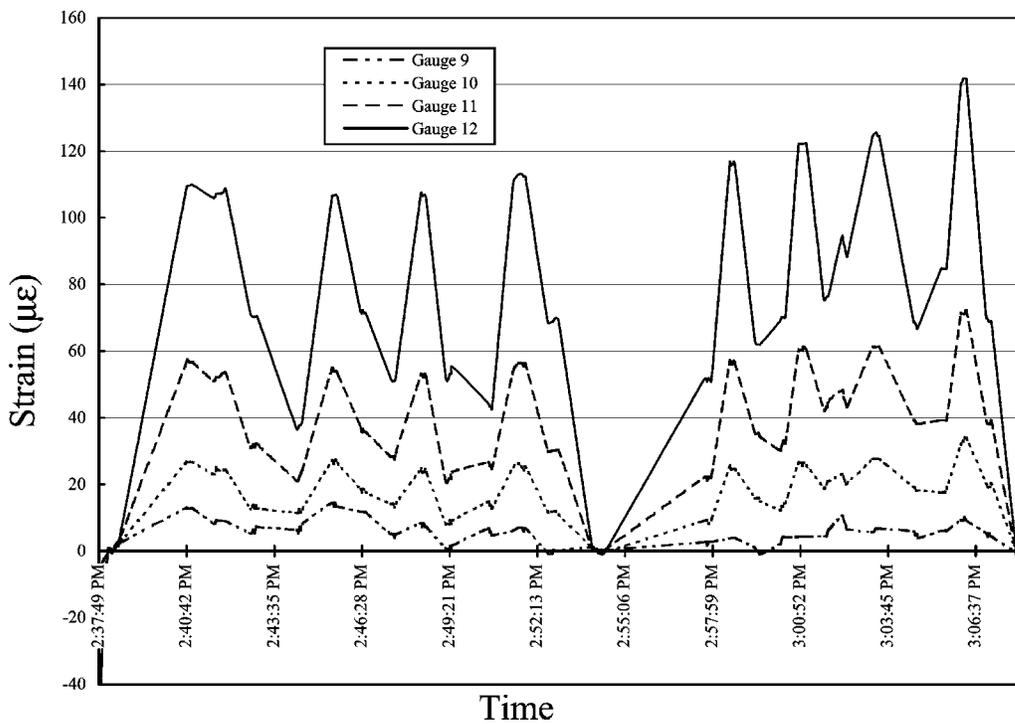
Figure 4–14 Revised Static Measurements, Gauges 9 Through 12, Girder 2 North

52
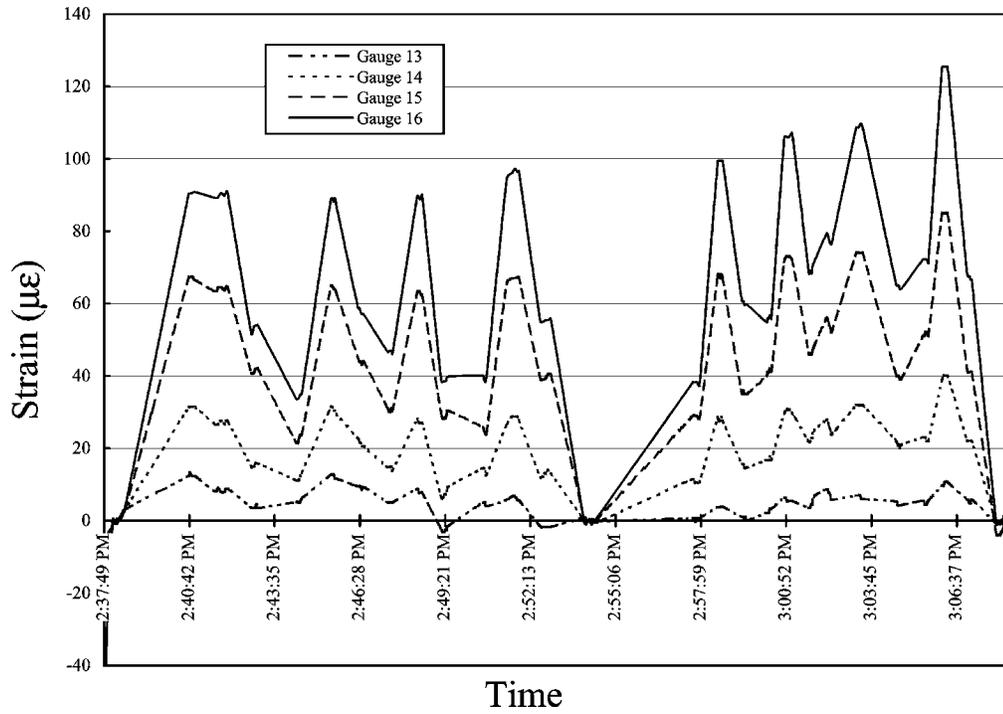
Figure 4–15 Revised Static Measurements, Gauges 13 Through 16, Girder 2 South
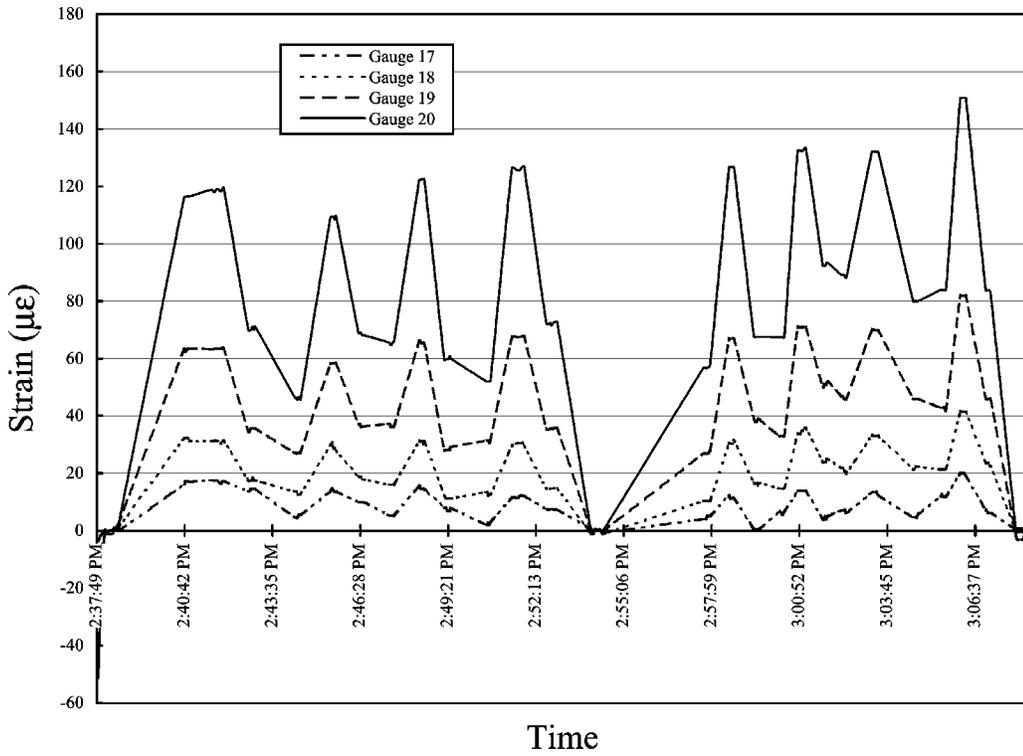
Figure 4–16 Revised Static Measurements, Gauges 17 Through 20, Girder 3 North
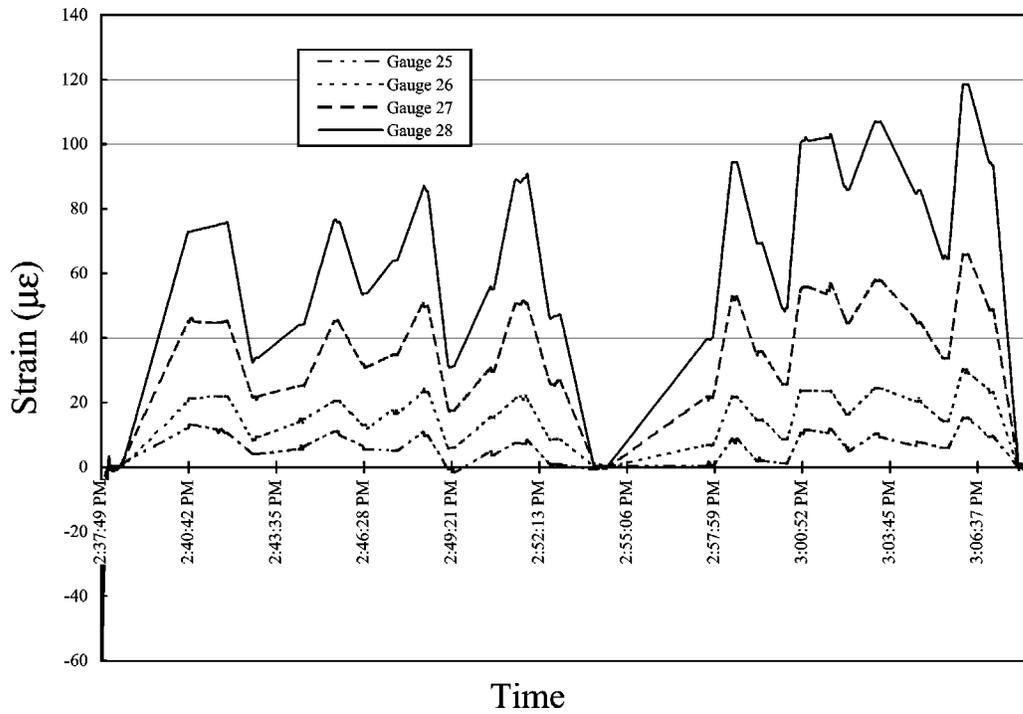
Figure 4–17 Revised Static Measurements, Gauges 25 Through 28, Girder 4 North
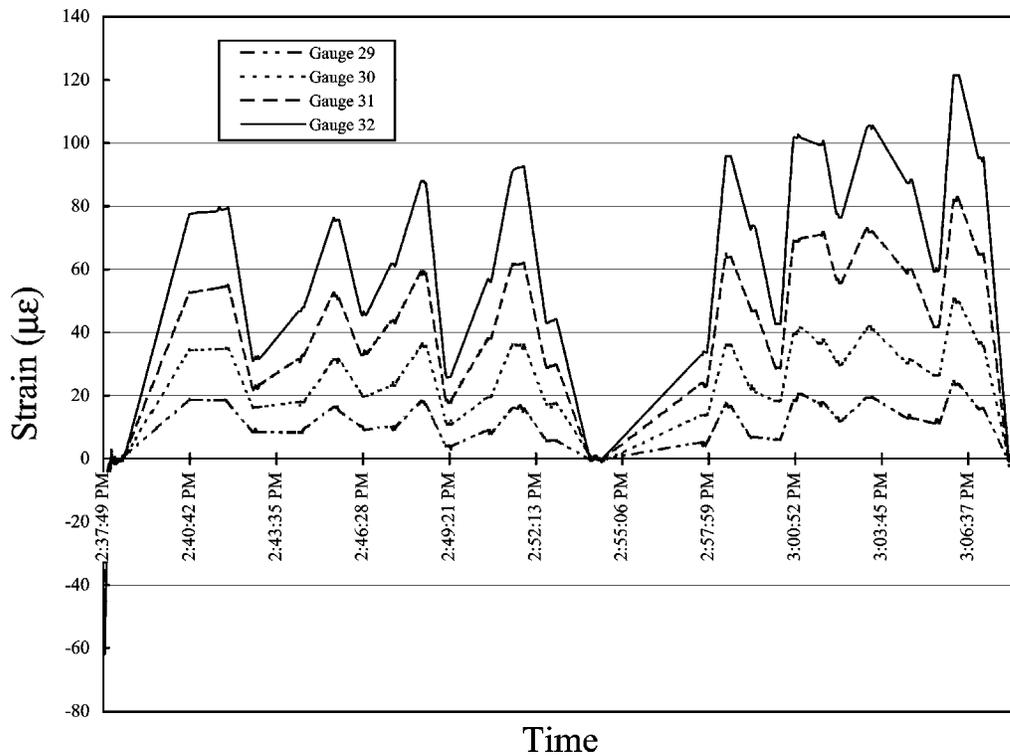
Figure 4–18 Revised Static Measurements, Gauges 29 Through 32, Girder 4 South

54
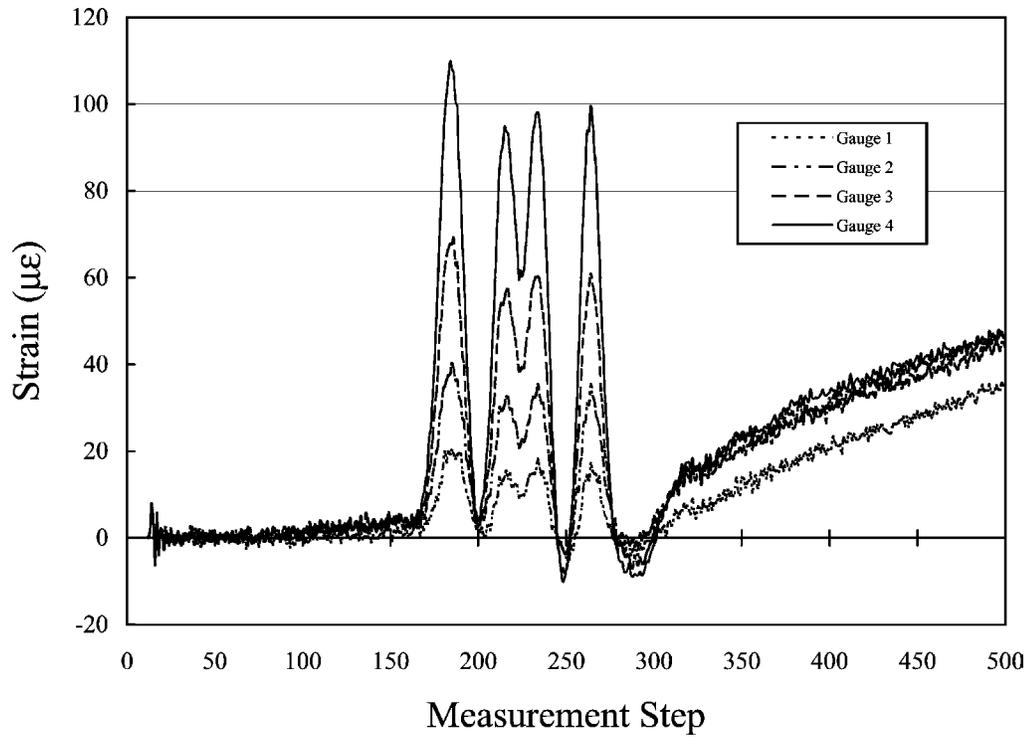
Figure 4–19 Measured Dynamic Strain vs. Time Step – Gauges 1 Through 4, Girder 1 North
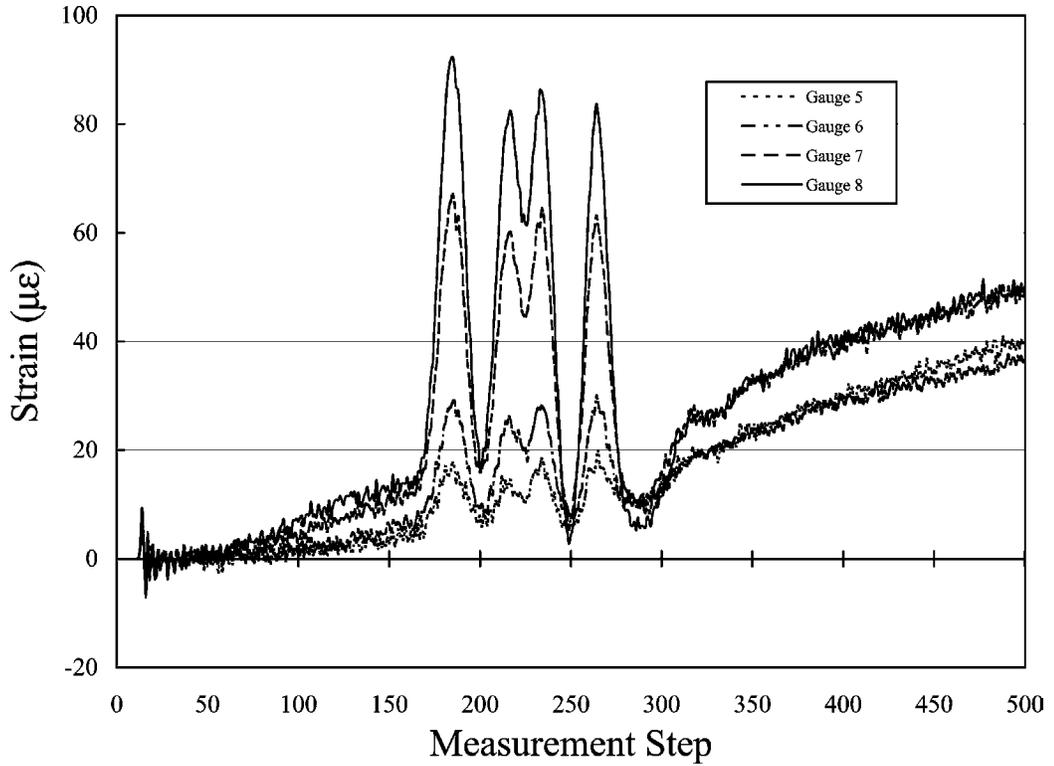
Figure 4–20 Measured Dynamic Strain vs. Time Step – Gauges 5 Through 8, Girder 1 South
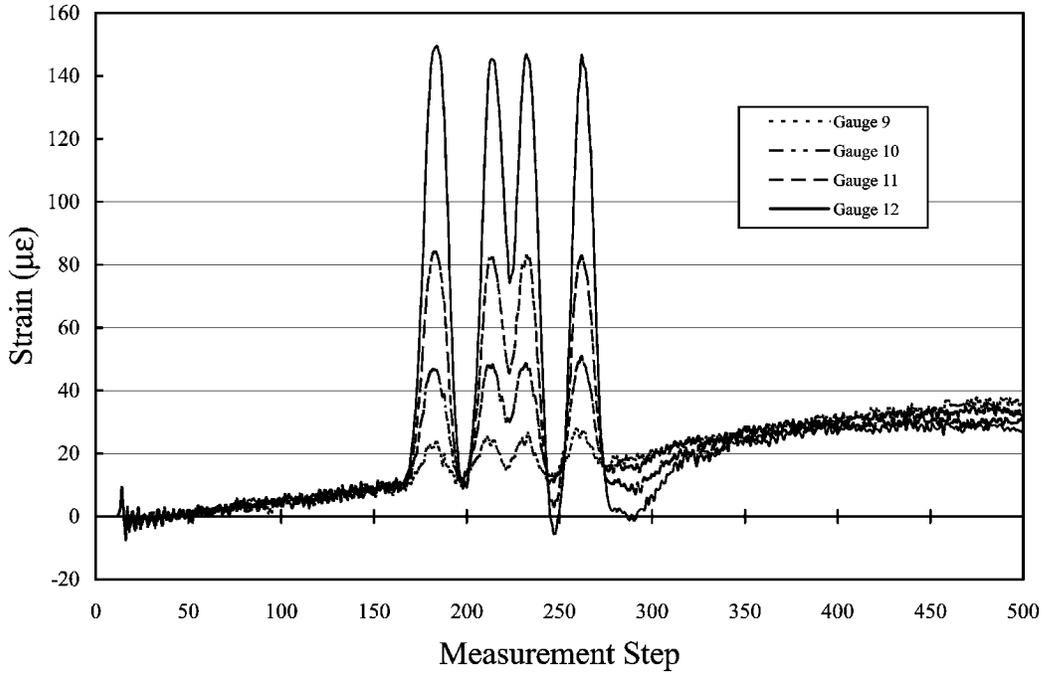
Figure 4–21 Measured Dynamic Strain vs. Time Step – Gauges 9 Through 12, Girder 2 North
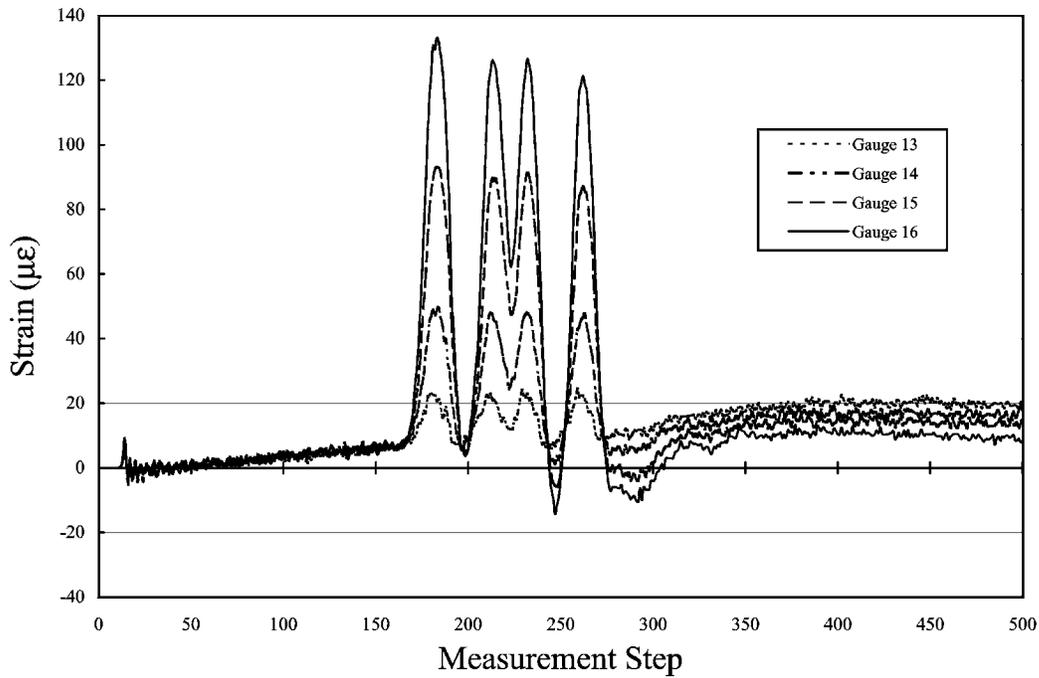
Figure 4–22 Measured Dynamic Strain vs. Time Step – Gauges 13 Through 16, Girder 2 South

56
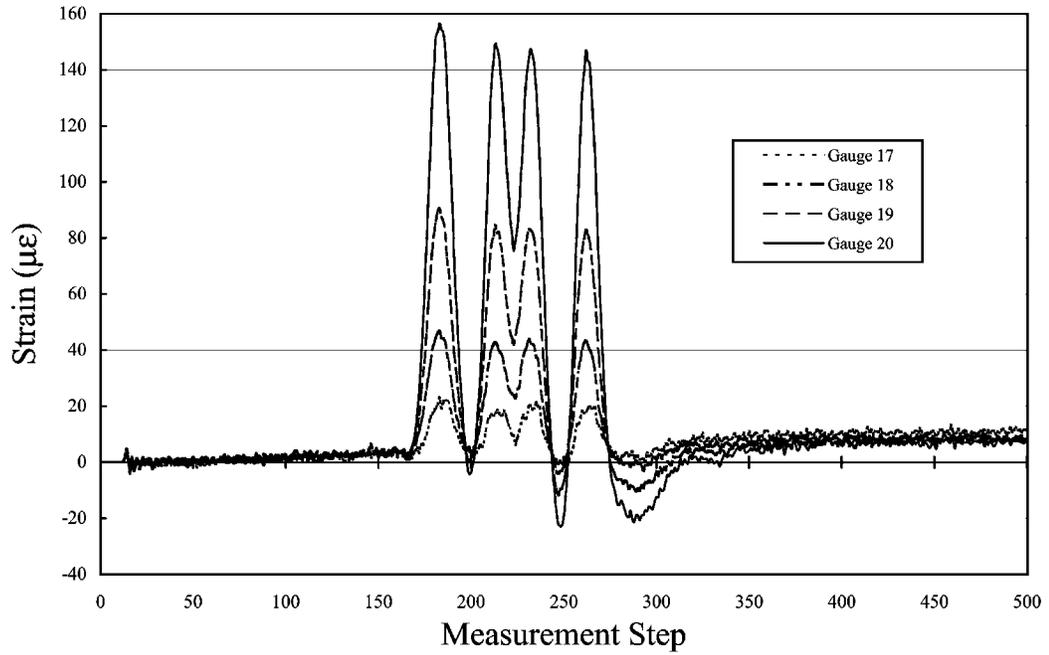
Figure 4–23 Measured Dynamic Strain vs. Time Step – Gauges 17 Through 20, Girder 3 North
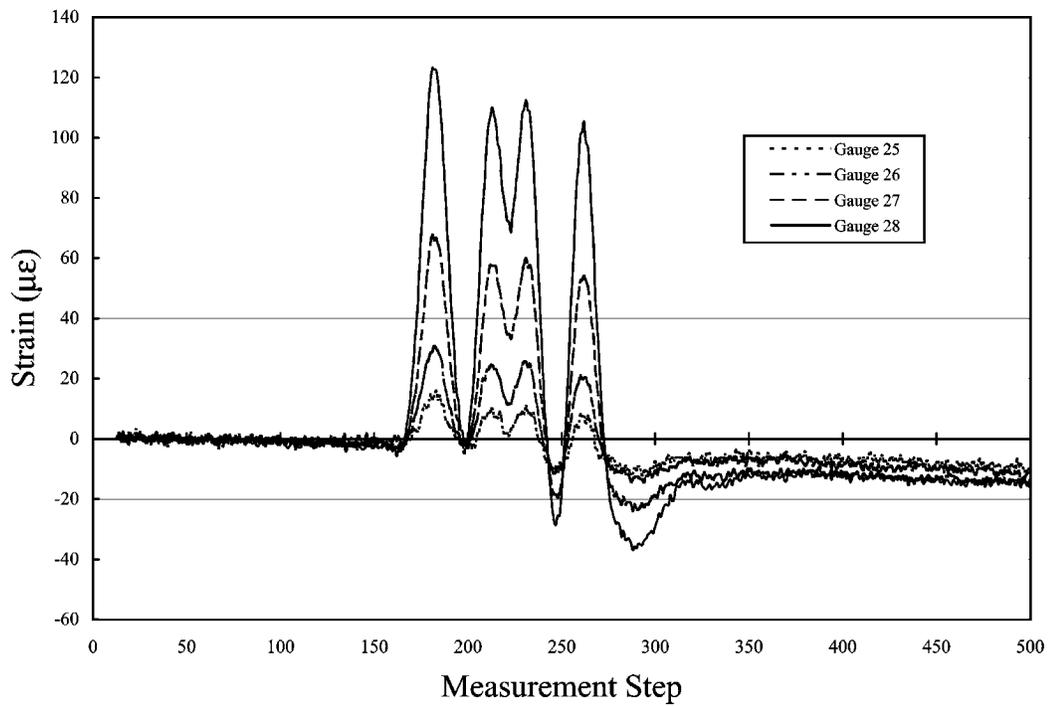
Figure 4–24 Measured Dynamic Strain vs. Time Step – Gauges 25 Through 28, Girder 4 North

57
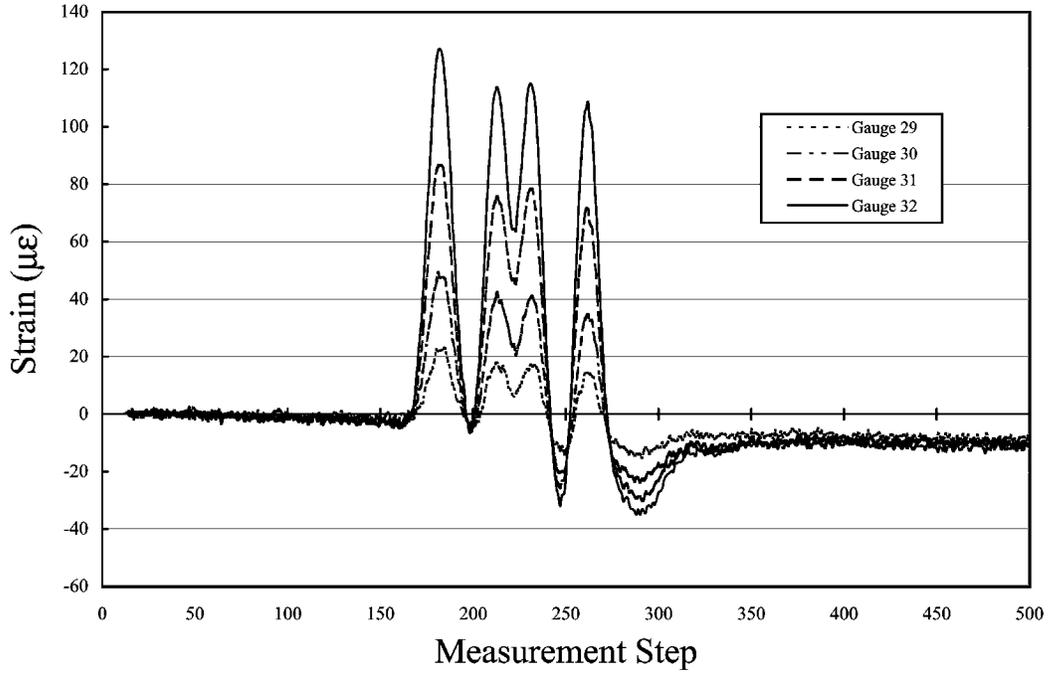
Figure 4–25 Measured Dynamic Strain vs. Time Step – Gauges 29 Through 32, Girder 4 South
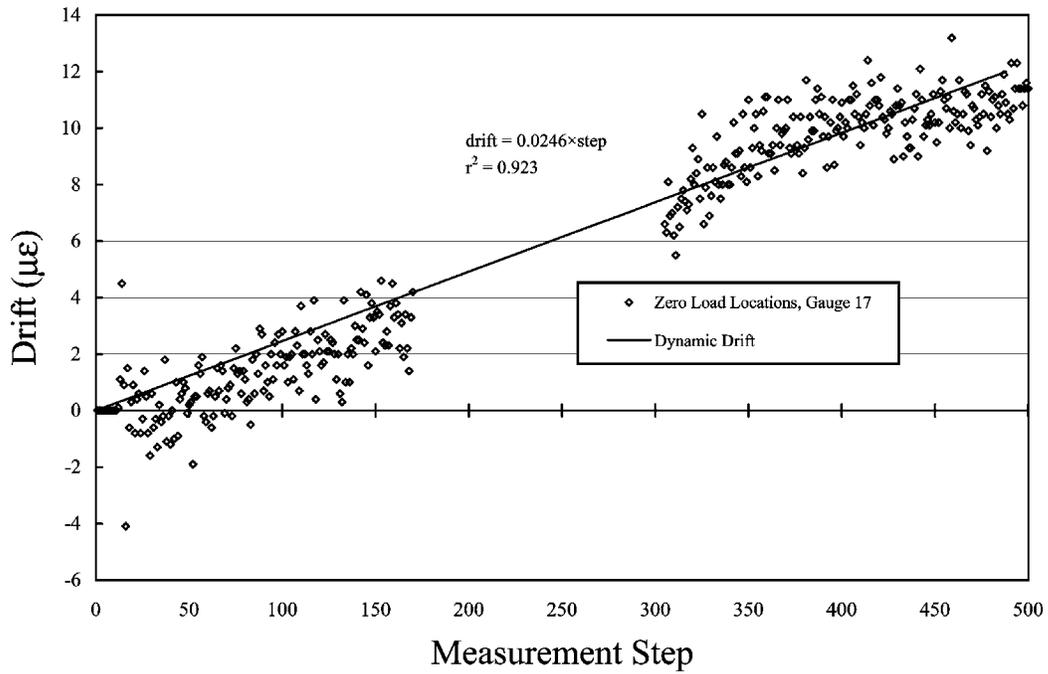
Figure 4-26 Drift vs. Step, Gauge 17

58
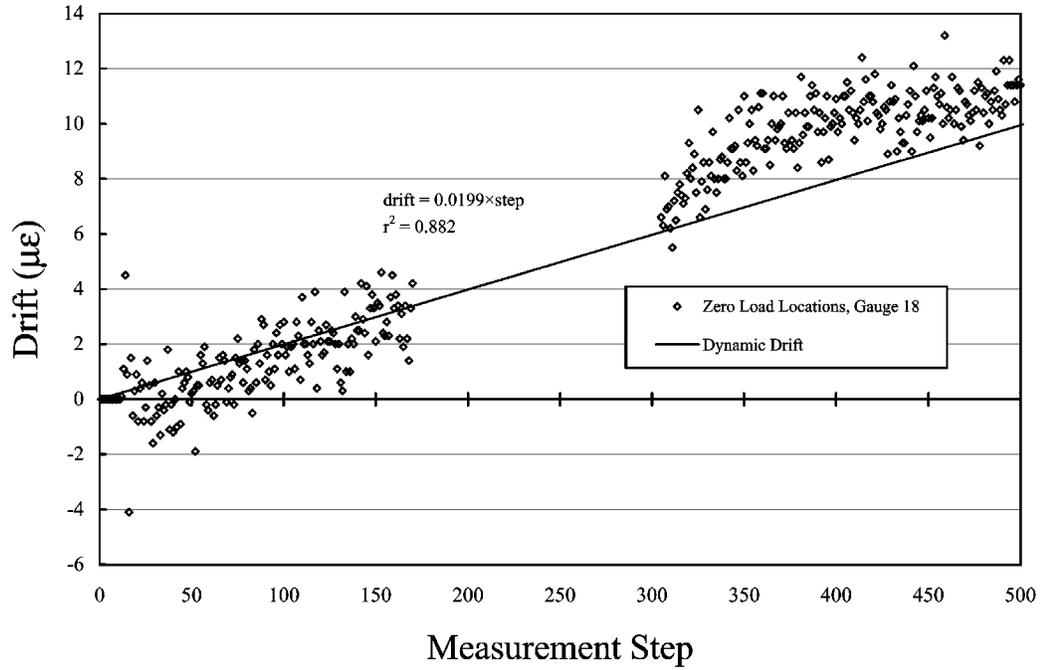
Figure 4–27 Drift vs. Step, Gauge 18
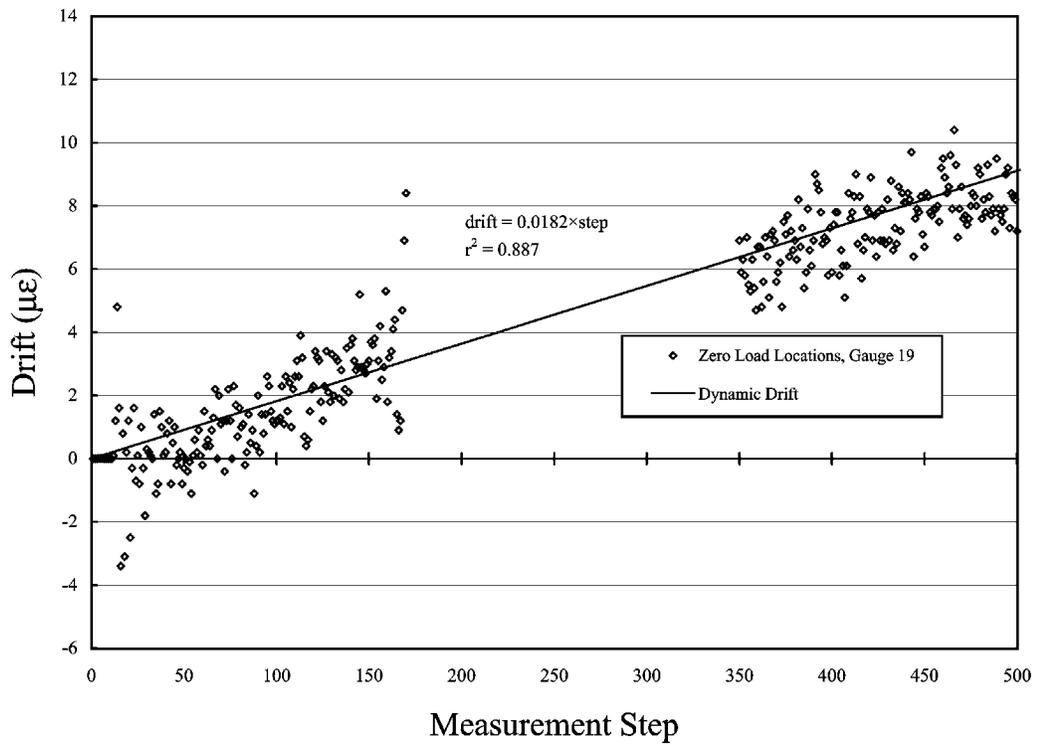
Figure 4–28 Drift vs. Step, Gauge 19
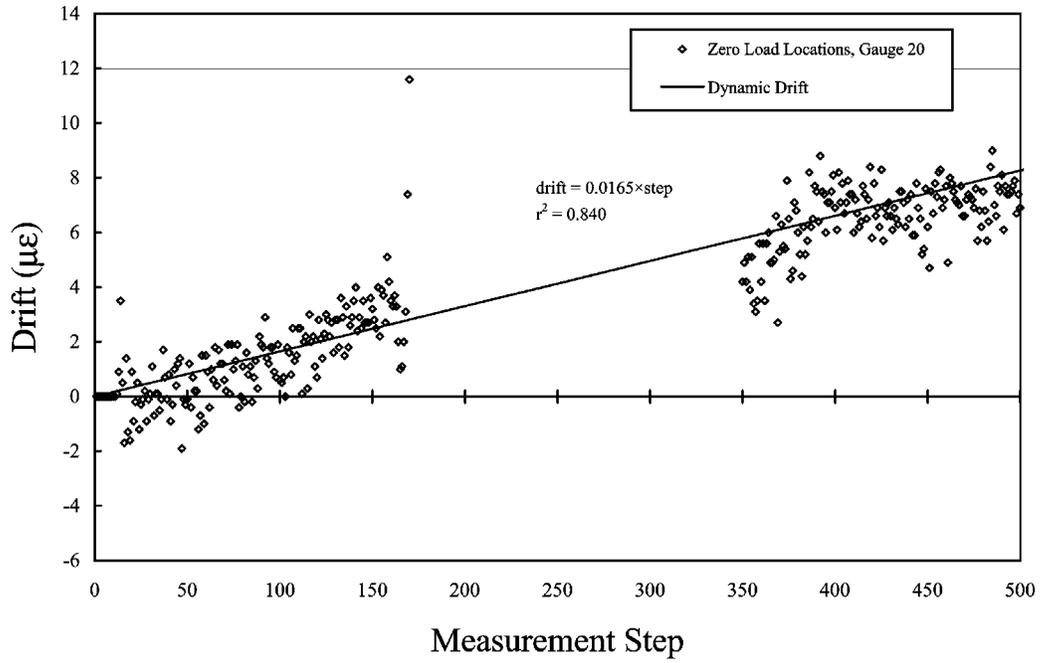
Figure 4–29 Drift vs. Step, Gauge 20
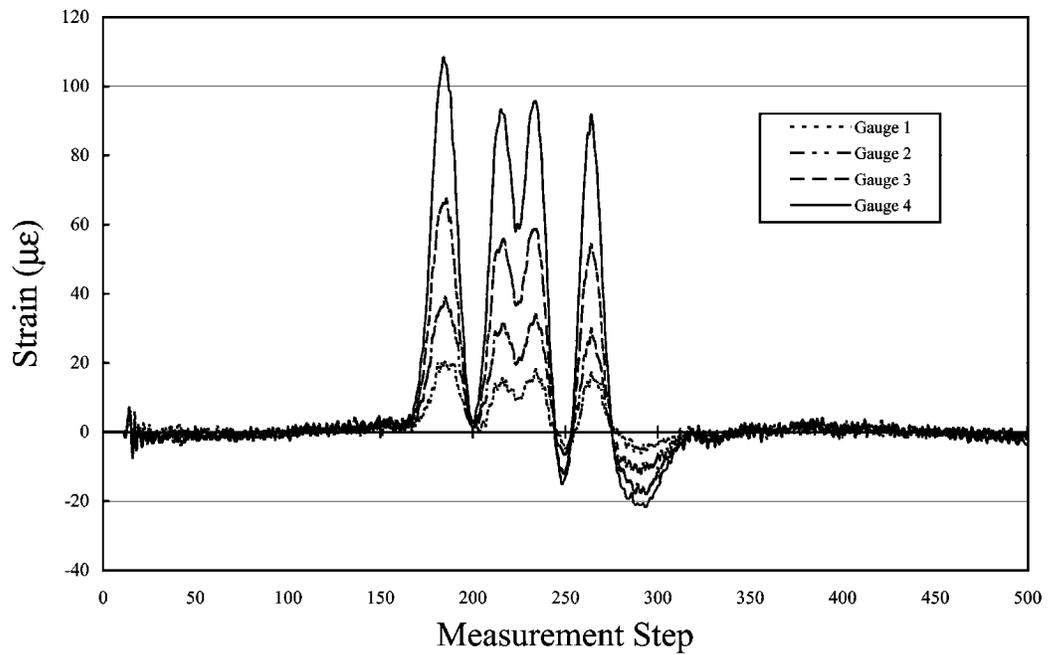
Figure 4–30 Revised Dynamic Measurements, Gauges 1 Through 4, Girder 1 North
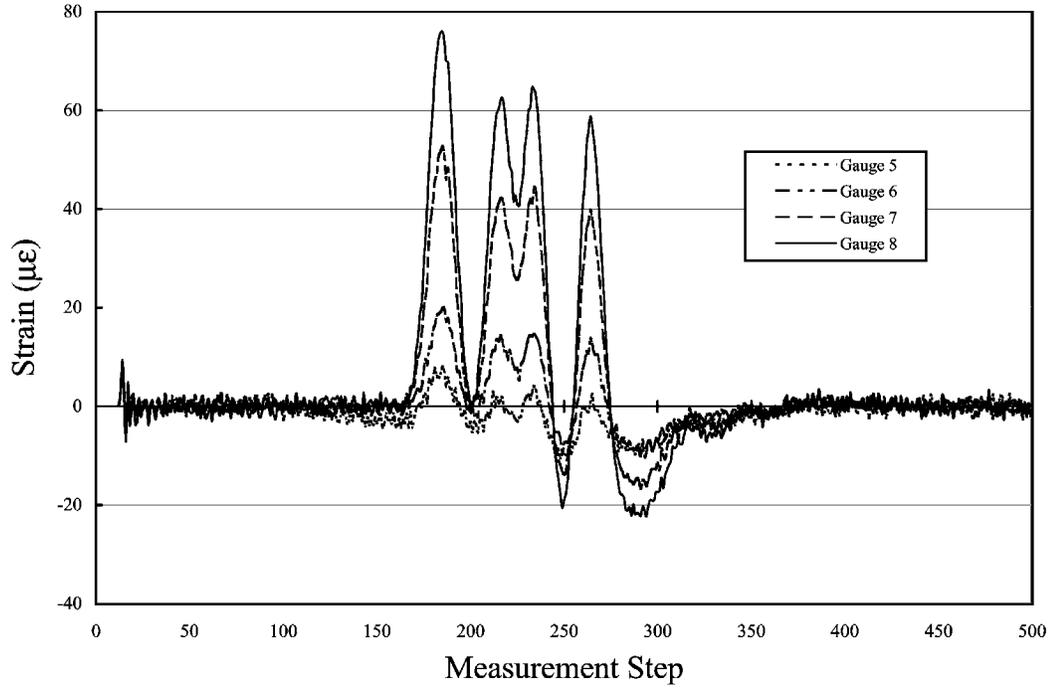
Figure 4–31 Revised Dynamic Measurements, Gauges 5 Through 8, Girder 1 South
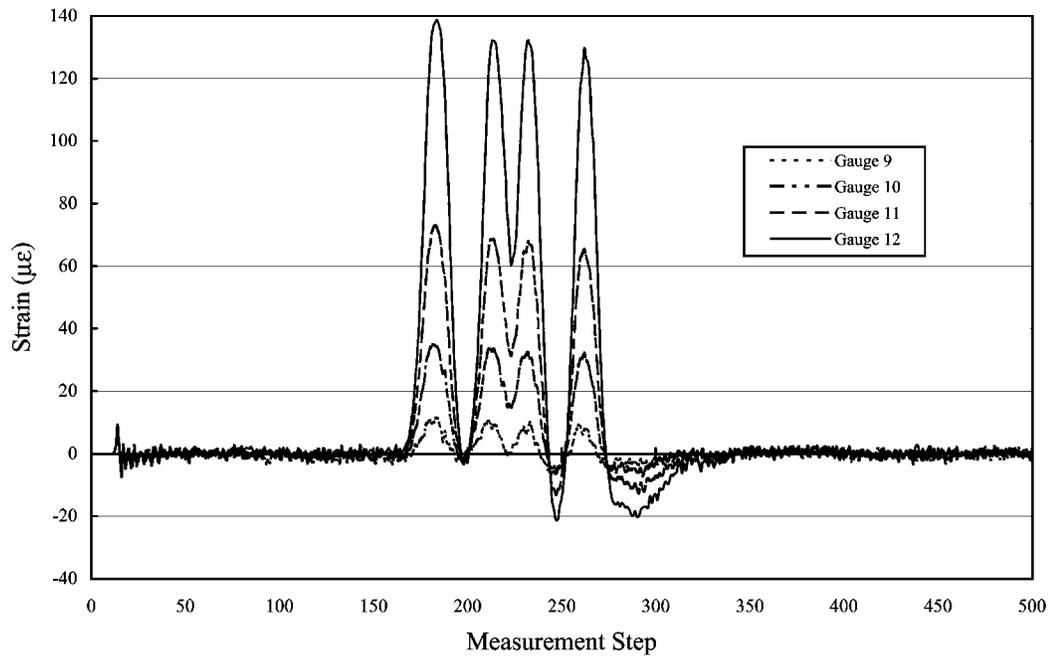
Figure 4–32 Revised Dynamic Measurements, Gauges 9 Through 12, Girder 2 North

61
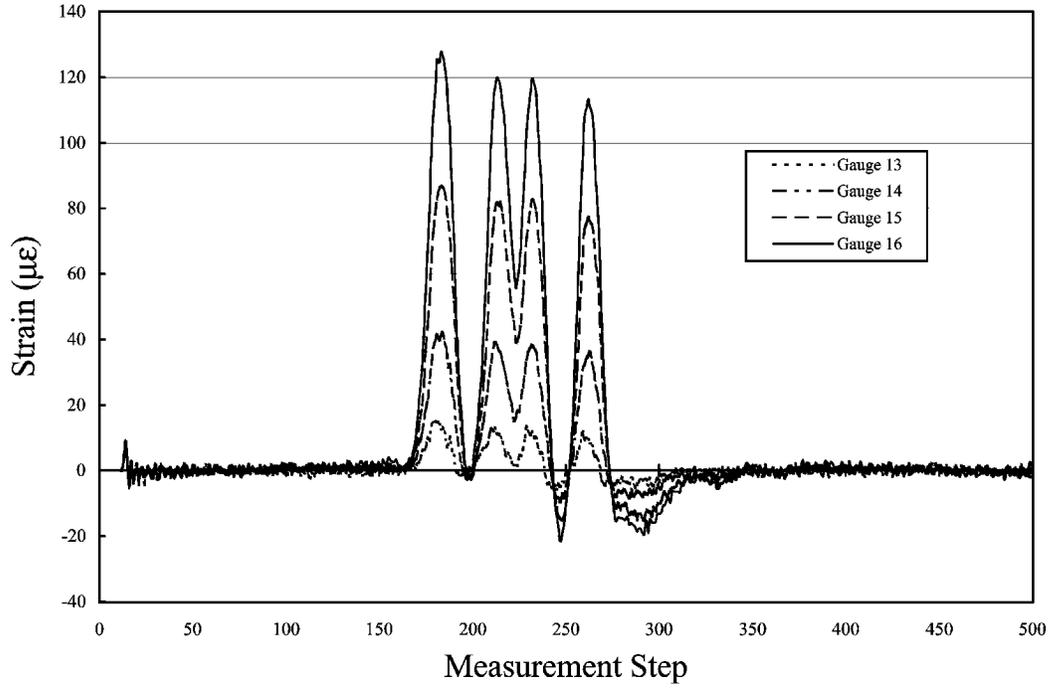
Figure 4–33 Revised Dynamic Measurements, Gauges 13 Through 16, Girder 2 South
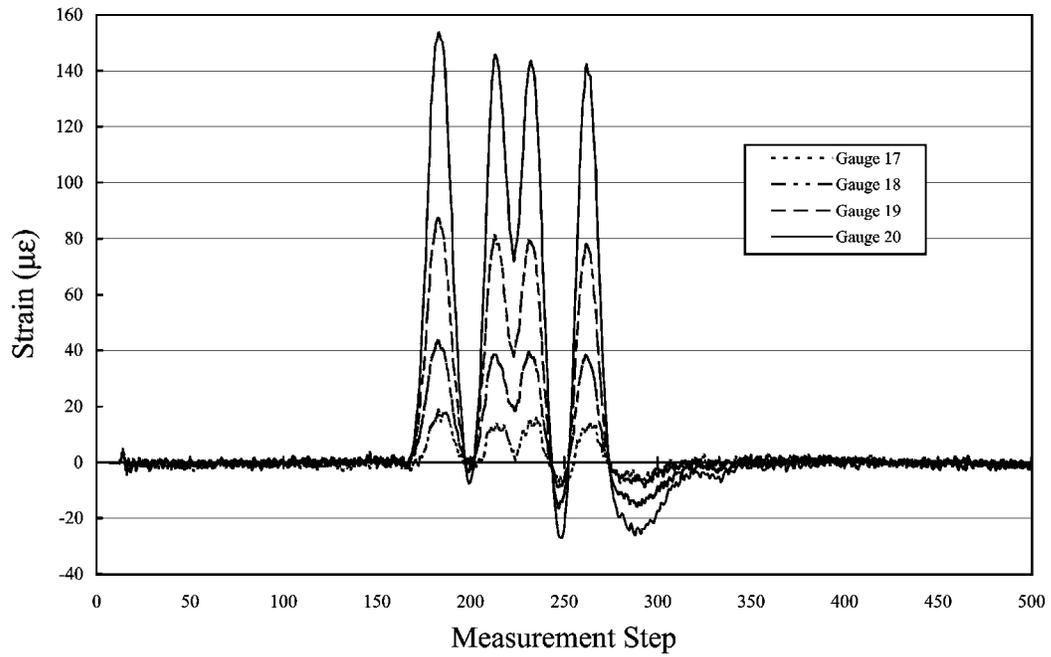
Figure 4–34 Revised Dynamic Measurements, Gauges 17 Through 20, Girder 3 North

62
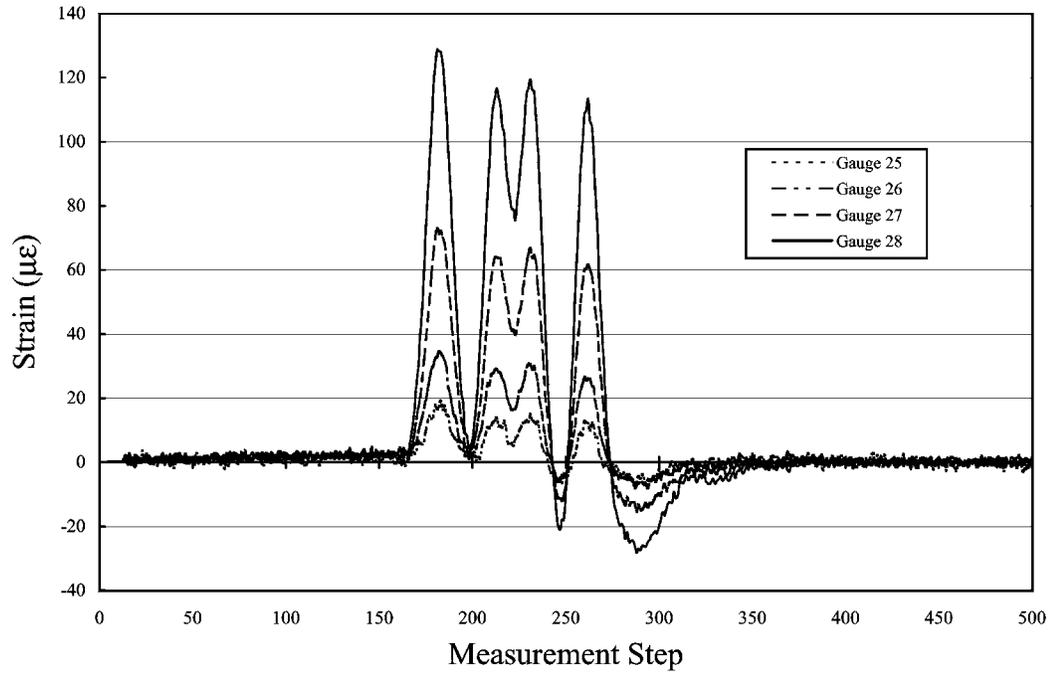
Figure 4–35 Revised Dynamic Measurements, Gauges 25 Through 28, Girder 4 North
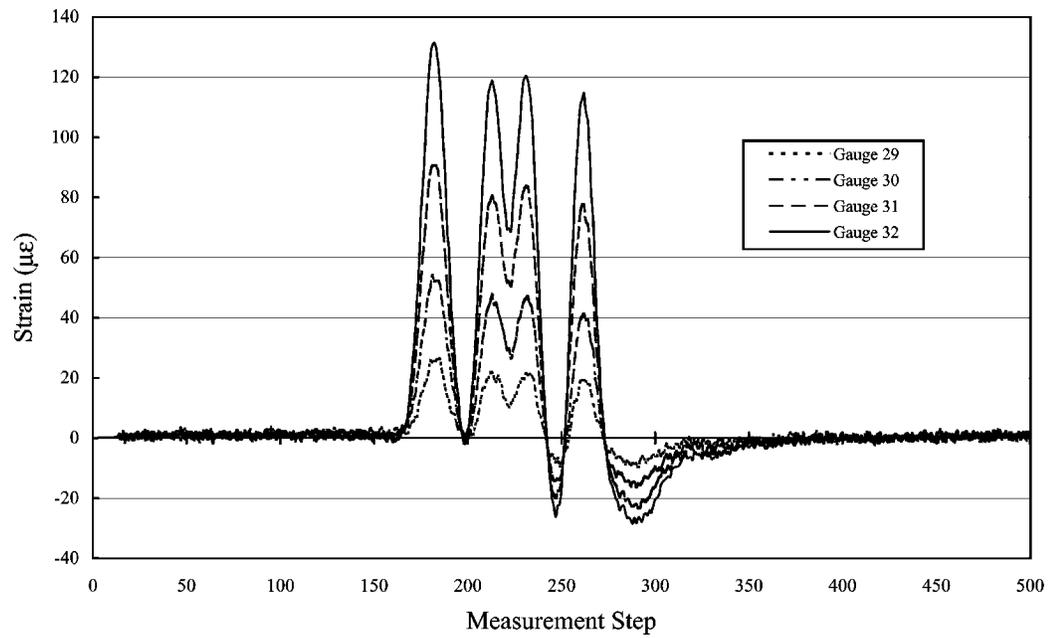
Figure 4–36 Revised Dynamic Measurements, Gauges 29 Through 32, Girder 4 South
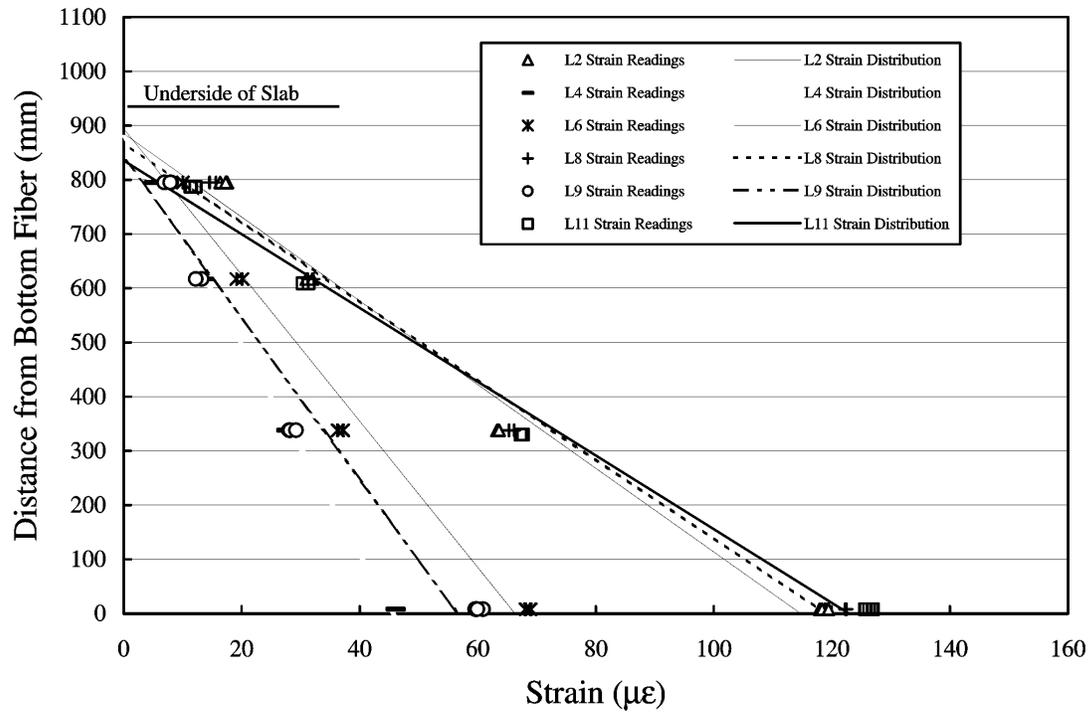
Figure 4–37 Static Strain Distributions, Locomotives Advancing Westward,Girder 3 North
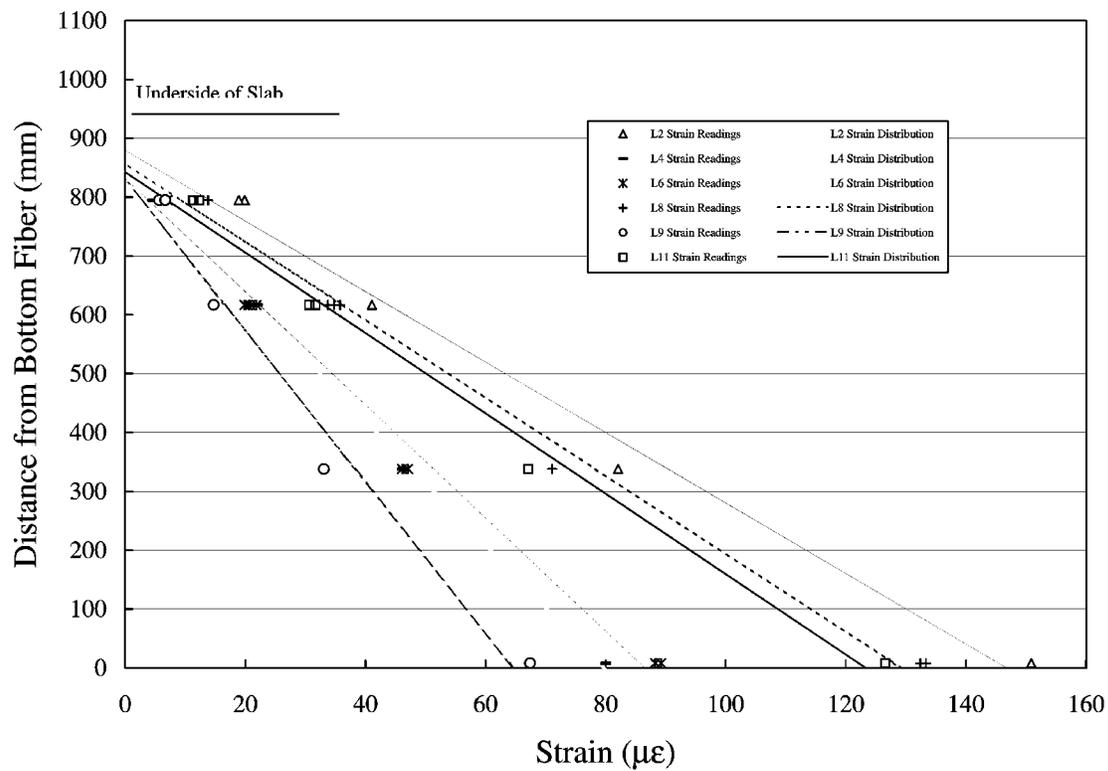
Figure 4–38 Static Strain Distributions, Locomotives Advancing Eastward, Girder 3 North
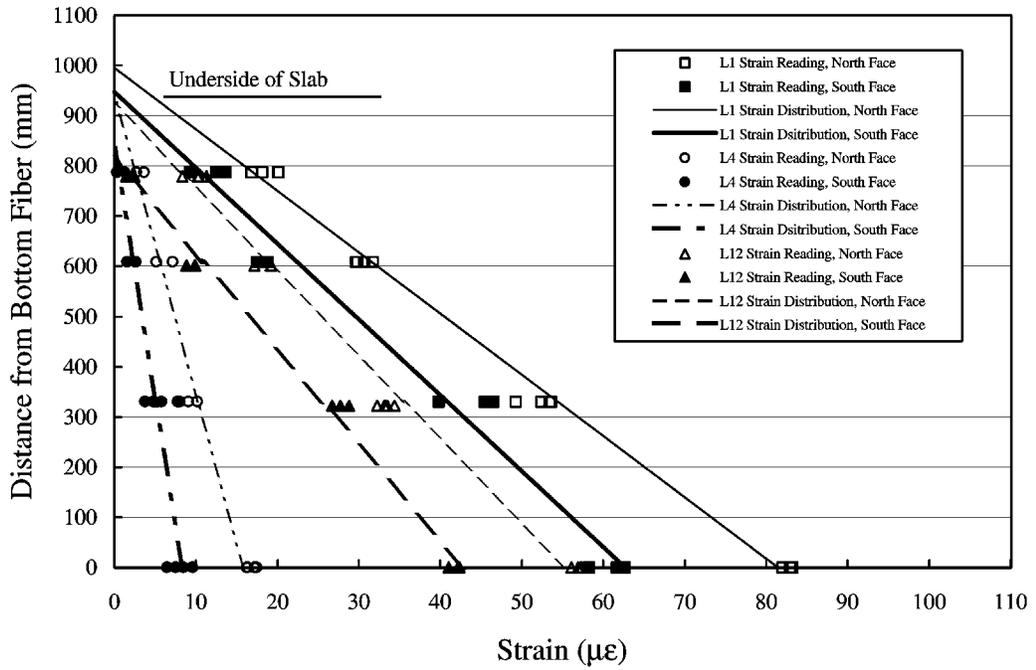
Figure 4–39 Strain Distribution on the North and South Face of Girder 1
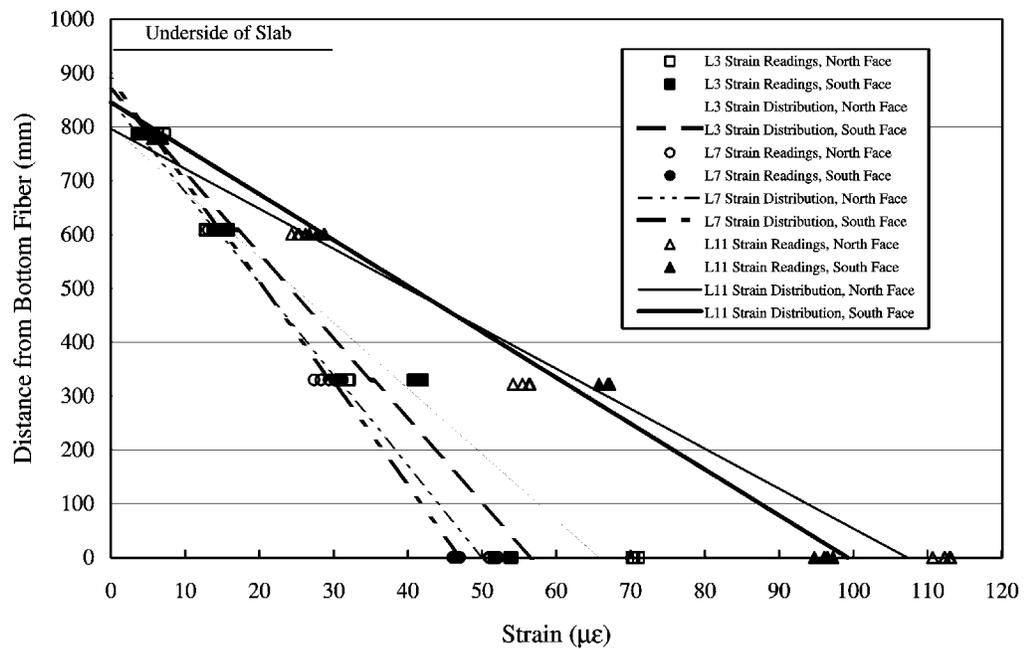
Figure 4–40 Strain Distribution on the North and South Face of Girder 2
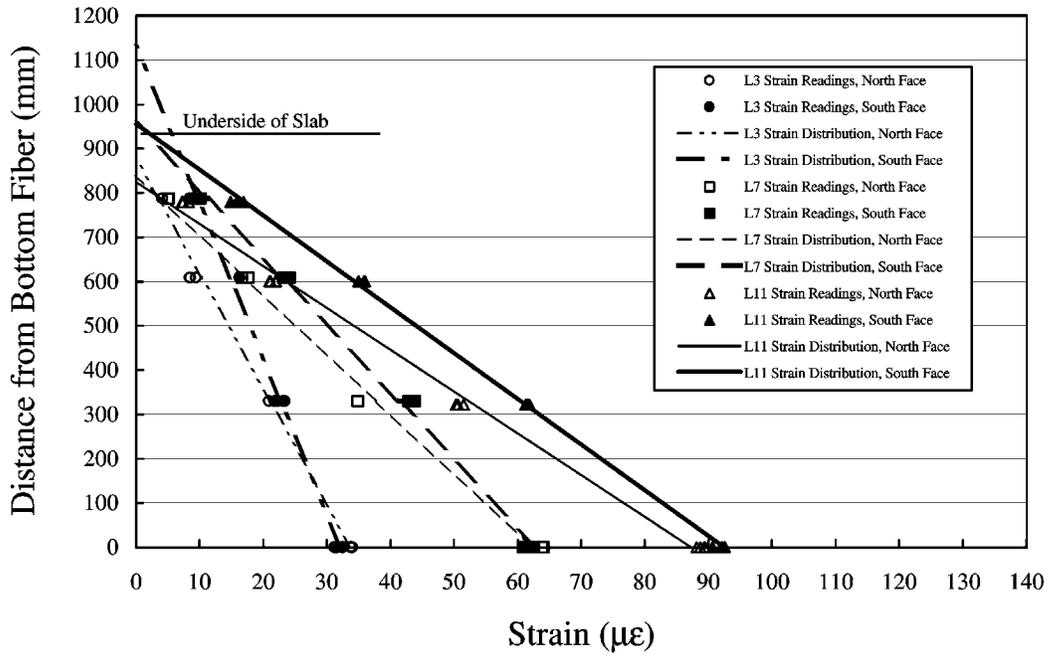
Figure 4–41 Strain Distribution on the North and South Face of Girder 4
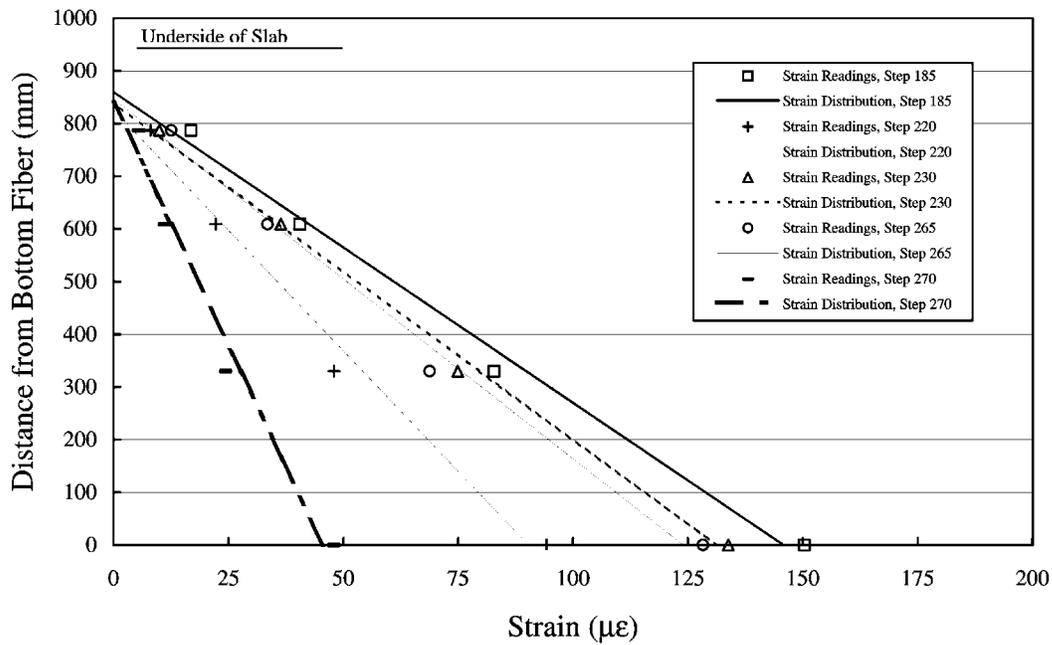
Figure 4–42 Dynamic Strain Distributions, Girder 3 North

66
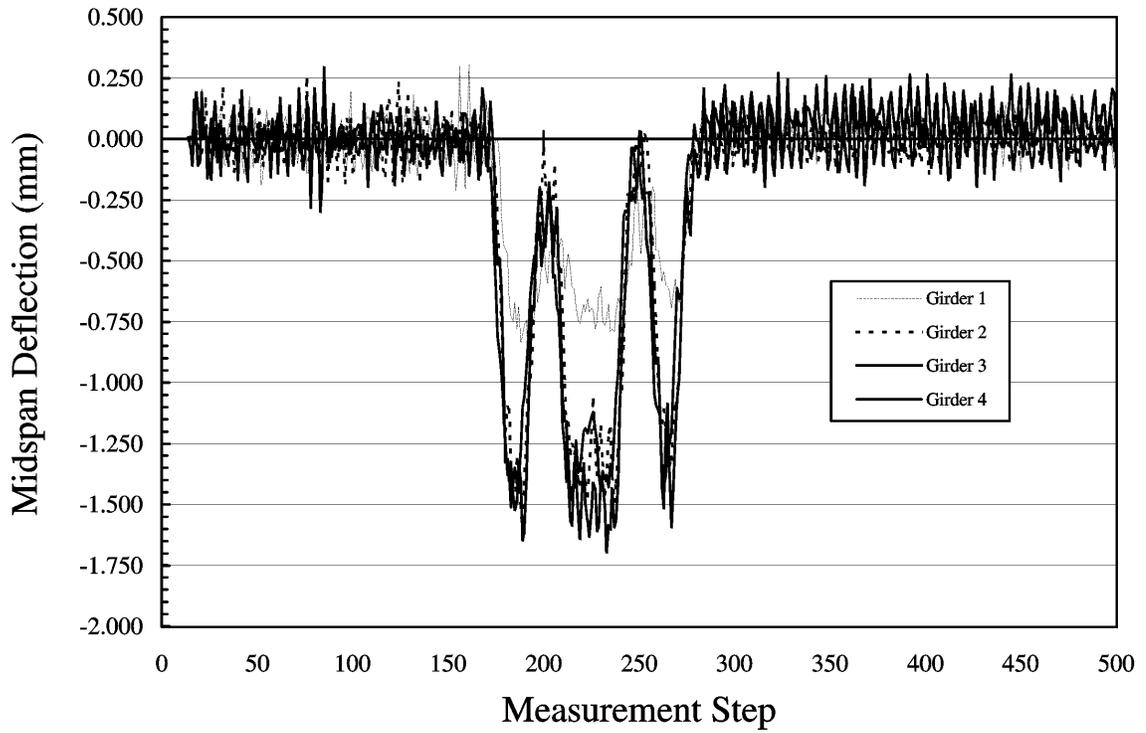
Figure 4–43 Dynamic Vertical Displacement at Midspan of Girders
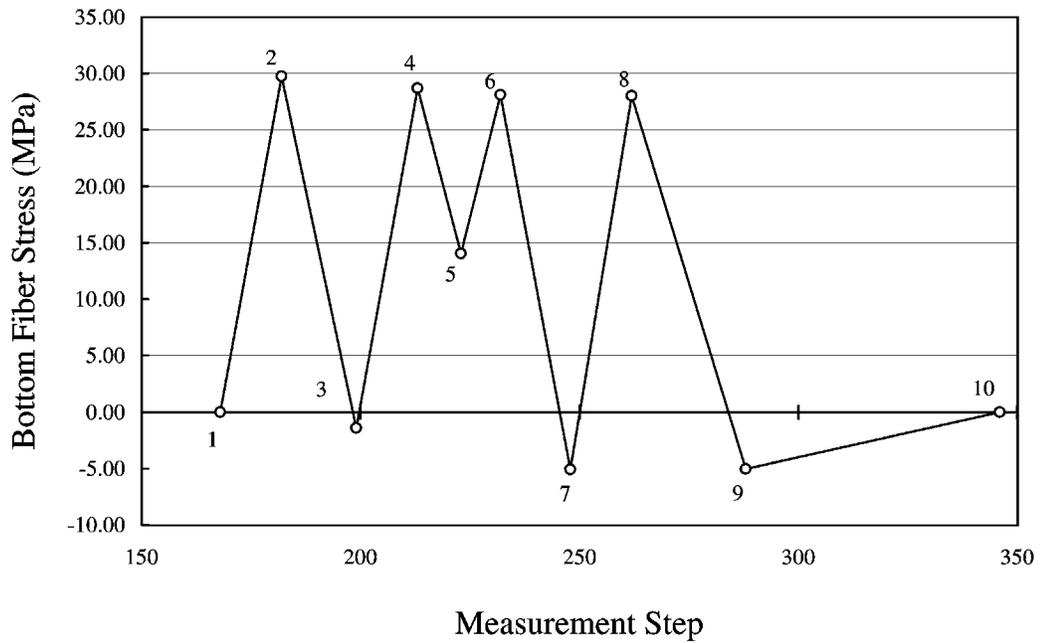
Figure 4–44 Bottom Fiber Stress vs. Dynamic Measurement Step, Girder 3
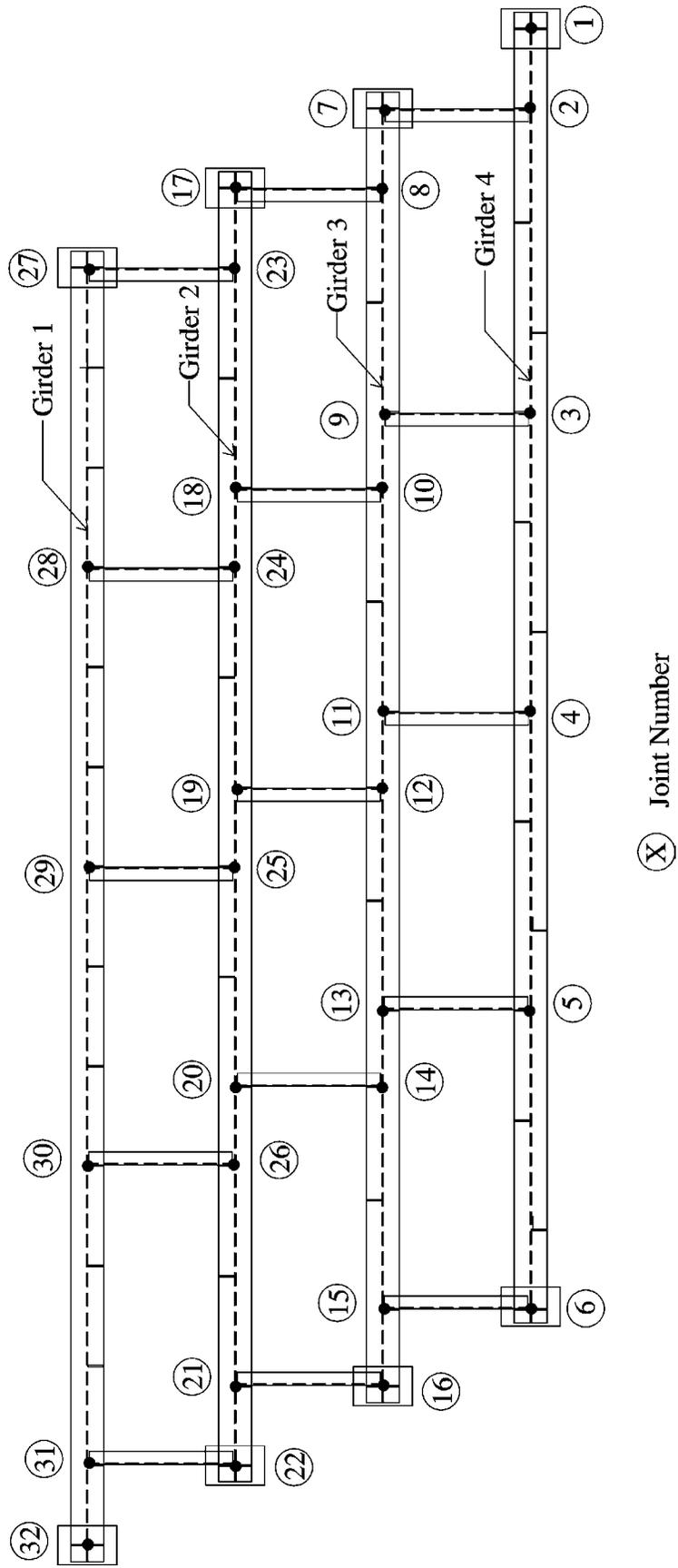
Figure 4-45 Joint Numbering System Employed in Numerical Model of Test Span
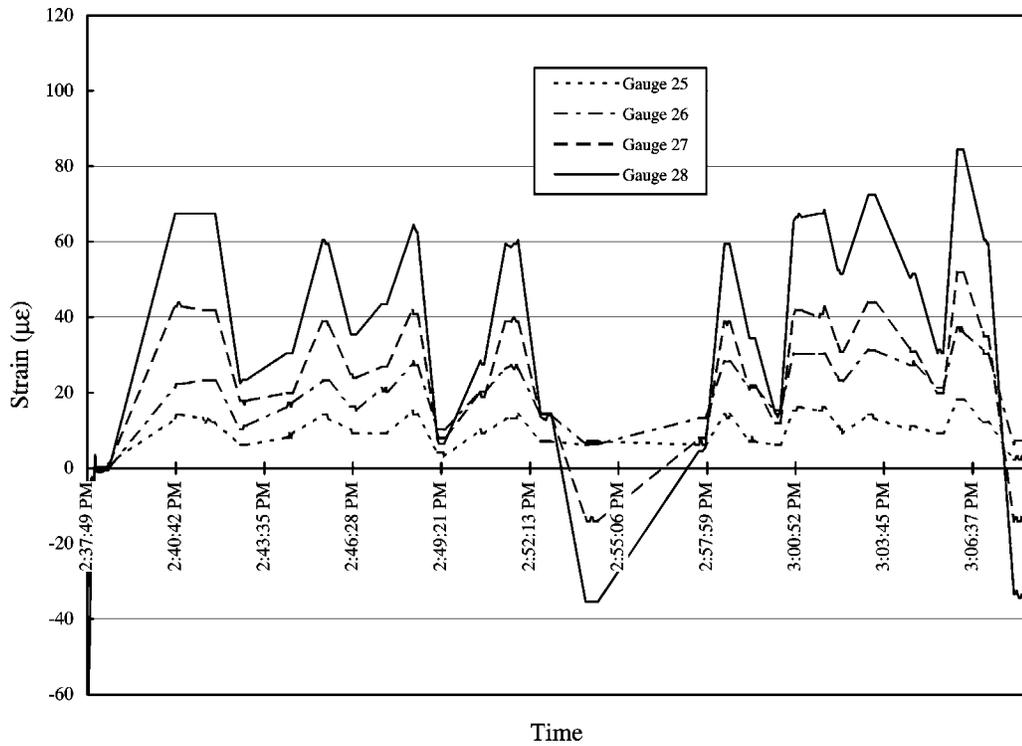
Figure 4–46 Out-of-Plane Web Distortions Measured During Dynamic Field Testing
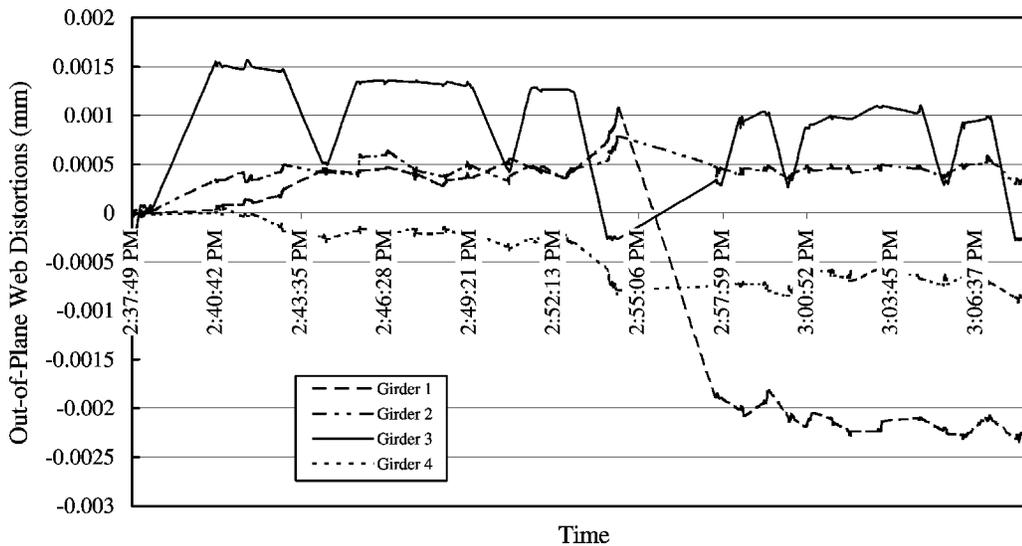
Figure 4–47 Out-of-Plane Web Distortions Measured During Static Field Testing

CHAPTER 5

EXPERIMENTAL PROGRAM

5.1 Design of Laboratory Test Based on Field Test Results

An experimental testing program was undertaken to study the remaining fatigue life of three of the girders obtained from the CN Mile 5.09 Edson Subdivision Bridge. The test specimens were tested under conditions similar to the measured service behaviour of the most heavily loaded girder, referred to as Girder 3 in Chapter 4. The tests were performed to assess the behaviour of distortion-induced fatigue cracks under simulated extreme winter conditions. This yields valuable information for the management of similar existing bridges.

The information obtained from the analysis of the field test data was used to design the experimental program. Several aspects of the behaviour were taken into consideration in the design of the laboratory test set-up. These aspects include the position of the neutral axis and composite moment of inertia of an interior girder, the stress range at the midspan extreme bottom fiber, the span moment-to-shear ratio at the critical dynamic load step, and the differential displacements between adjacent girders at diaphragm positions.

5.1.1 Properties of Composite Girder

Using the results of the field test data presented in Chapter 4, the neutral axis position, measured from the bottom fiber of the steel girder, and the moment of inertia of a typical composite interior member were determined to be $847\,\text{mm}$ and $6\,240 \times 10^6\,\text{mm}^4$, respectively. The concrete slab was removed during dismantling of the bridge. Therefore, in order to simulate in the lab the in-situ composite girder properties determined during field testing, the test specimens had to be reinforced. Several options were considered for the design of this reinforcing section including a reinforced concrete slab, a steel plate, and a rolled steel section.

After consideration of the various alternatives, the steel girders were reinforced with a W250x167 steel wide flange section. This brought the centroid of the reinforced section to within three percent of the location of the neutral axis observed in the field and the moment of inertia to within less than one percent of the calculated value for the composite section. It also provided the added advantage that the reinforcing beam could be reused for several tests.

In order to facilitate the attachment of the W250×167 to the top flange of the test specimens, all shear studs were removed from the top flange of the girders by flame cutting and grinding. The studs were located above the centroid of the composite section; thus, in the compression zone when subjected to bending, any disturbance to the girders caused by removing the studs was deemed acceptable. Of course, care was taken during the removal process to minimize damage to the girders.

The reinforcing beam was connected to the steel girder with two rows of 7/8 in. diameter A325 bolts. Bolt spacing was determined based on the parameters presented in Clause 13.12.2 of CAN/CSA-S16.1-94 for slip critical connections (CSA, 1994). Calculation of the slip resistance of the bolts was based on the assumption that the contact surface of the bolted parts was a Class A surface (clean mill scale, or blast-cleaned with Class A coatings). The maximum shear flow in the beam–girder interface was determined based on the theoretical properties of the built-up section and a maximum shear force of 250 kN, which is approximately double the maximum shear in the girder during cyclic testing of the specimens. This large factor of safety was used to ensure that slip between the two planes would not occur during the tests. The analysis showed that the maximum allowable bolt spacing in the shear span was 533 mm. Bolts were also placed in the constant moment region at spacing similar to that calculated for the shear span. This was done for two reasons. First, since the calculated bolt spacing was reasonable, adding bolts in the constant moment region was not a time-consuming job. Second, during the freeze tests a load case was adopted in which the load was applied with only one jack, thus creating shear over the full length of the girder. Figure 5–1 shows the detail for the connection used to provide 100% composite action between the girder and W250×167 reinforcing section.

When the reinforcing beam was placed on top of each girder, it was noticed that the girders were sagging at midspan, probably because of permanent deformations that occurred in service. For each test specimen, the resulting gap between the two steel sections ranged from zero at the ends of the girder to a maximum of 13 mm near the girder midspan. Shims were used at each bolt hole location to ensure that the proper normal force between the two contact surfaces was present to develop the slip resistance between the test girder and the reinforcing beam. The surfaces of the shims were roughened such that the surface roughness was close to that of a mill scale, Class A, surface.

5.1.2 Orientation and Magnitude of Laboratory Test Loads

The bottom fiber stress range measured in the field was used in conjunction with the maximum service shear and moment values to determine the magnitude and position of the test loads. The bottom fiber stress range chosen for testing purposes was the

maximum in-situ stress range of 35 MPa, located at the midspan in Girder 3. This stress range was chosen instead of the result of an equivalent stress range analysis for several reasons. The Class EF-644a locomotives provided for field testing were both the heaviest locomotives in CN Rail's locomotive fleet and were one of the heaviest repetitive service loads on the bridge during its service life. CN officials informed University of Alberta researchers that significantly heavier rail car loads were driven over the bridge during its service life, but only on the order of once every 10 years. Hence, these infrequent stress cycles, produced by the heavier rail cars, are an ultimate limit state concern, rather than a fatigue limit state concern. Since 12 specimens in total are available for testing, it was felt that the girders would be tested at different stress ranges throughout the testing program. Therefore, testing the first three girders at the highest stress range measured during field testing was appropriate. Furthermore, testing the first set of girders at essentially an upper bound service stress range would produce a lower bound solution for the remaining life of similar girders in service. One of the primary concerns with this type of fatigue cracking is the stability of the fatigue cracks at low temperature. Therefore, starting the program by testing at a high service stress range would provide an immediate conservative answer to this concern.

The maximum bottom fiber stress measured in the test girders during field testing was 29.8 MPa at dynamic load step 184. An analysis of the structure at this load step was carried out to determine the service load effects in the girders. The maximum service moment was calculated to be 222 kN m (located at midspan of Girder 3) and the corresponding service shear was computed to be 69 kN (located at the ends of Girder 3). In order to replicate the moment-to-shear ratio in the test specimens, the length of the constant moment region, i.e. the distance between the two test actuators, would have to be 2 680 mm. If this length was adopted only two web gaps at diaphragm positions would be located within the constant moment region. Consequently, the field moment-to-shear ratio was abandoned and the constant moment region was increased to 4 000 mm in order to incorporate more defects within the constant moment region. The choice of a 4 000 mm constant moment region was made since this placed the test loads very close to two diaphragm positions, thus creating a maximum moment and shear situation in the girder at these critical locations. Furthermore, the distance between the outside axles of the locomotive trucks is 4 013 mm. This made the number of critical diaphragm locations surrounded by the locomotive axles virtually the same as the number surrounded by the loads during laboratory testing.

With the position of the loads established, the loads required to achieve the 35 MPa stress range and the correct differential displacements (see Table 4–7) at the diaphragm positions were calculated. In order to simplify the test setup, stress reversal during testing was not desirable. Hence, the maximum and minimum stresses of 30 MPa and -5 MPa needed to be raised so as to maintain the same range but ensure that the bottom fiber of

the girder remained in tension throughout the duration of the test. Maximum and minimum stresses were therefore chosen to be 47 MPa and 12 MPa, respectively. Since theoretically the ram heads of each actuator would always be in contact with the girder during testing, no positive connection was provided between the girder and actuators. Therefore, a minimum test load greater than 0 kN was desired so as to reduce the chance of the jacks lifting away from the beam and then impacting the beam on the following load excursion.

The theoretical test loads were determined using a numerical model that considered the load distribution through the diaphragms (see Section 5.1.3, below). Results indicated that the magnitude of the theoretical test loads required to achieve the chosen midspan bottom fiber stresses and the correct differential displacements at diaphragm positions were a maximum load of 150 kN and a minimum load of 45 kN. To correct for inertia forces during dynamic testing, the minimum dynamic load to achieve the 12 MPa midspan stress was determined to be approximately 15 kN for each of the three tests conducted. The 15 kN loads were as close to the null load condition as desired, which is why the minimum and maximum stresses were chosen to be 12 MPa and 47 MPa, respectively.

5.1.3 Design of Diaphragm Spring Supports

Initially, attempts were made to design the laboratory test as a three-girder setup with three interconnected girders supported and loading only the middle girder. A model of the three-girder test setup was generated using S-Frame® and several attempts were made to correlate the calculated differential displacements to the differential displacements measured during the field test. The results showed that the differential displacements at each diaphragm location would be considerably larger in the test if stiff supports were used at the ends of all three girders while loading only the middle girder of a set of three girders. If the W250×167 reinforcing section was bolted to the loaded girder only and if flexible springs were used at the ends of the exterior girders the expected differential displacements during the test would still be larger at most diaphragm locations. Furthermore, under this test configuration, a reversal of differential displacements near the supported girder ends would result because of the presence of the exterior girder spring supports.

In order to ensure that both the stress range and differential displacements in the laboratory test were representative of field conditions, it was determined that all girders in a set had to be loaded or that the girders had to be separated and individually tested with their diaphragms. The former option was rejected because it would take a great deal of effort and precision to properly load all three girders. The latter option was therefore chosen and the analysis required to assess the required spring stiffness to support the free

74

ends of the diaphragms was carried out. Under this single-girder test configuration, all unattached diaphragm ends needed to be supported in such a manner as to obtain the correct differential displacements. The required spring stiffness was obtained using two HSS 51×25×3.2 members oriented so as to produce weak axis bending of the sections and loaded at midspan through the vertical HSS member. Figure 5–3 shows a typical cross-section of the test setup as well as a section view of a typical diaphragm spring supported location. Using span lengths of 500 mm and 1 500 mm and the tabulated properties of the section, the range of practical spring stiffness values were determined using a numerical model of the test setup. Results indicated that the range of spring stiffness values was from 3 070 N/mm to 114 N/mm.

The required spring stiffness at each diaphragm position was determined such that the correct differential displacements and bottom fiber midspan stresses were obtained. At Joint 6 and Joint 17, the required spring stiffness was determined to be 5 960 N/mm. At all other diaphragm locations, essentially the same spring stiffness (1 740 N/mm) was found to be required. These stiffness values corresponded to approximate HSS member span lengths of 500 mm and 760 mm, respectively. At this stage, the calculated span lengths were approximate values since fine adjustments would be required to achieve the correct behaviour on the test floor. The actual spring member span lengths are presented in Chapter 6 when the static test results to acquire the desired test behaviour are discussed.

The maximum stress and maximum stress range in the HSS sections were calculated to be 190 MPa and 133 MPa, respectively. Connection of the HSS beam sections to the HSS verticals was made through pin connections, which penetrated through the HSS beam member webs above the neutral axis position in the compression zone. Hence, based on the provisions of Clause 14 of CAN/CSA-S16.1-94, it was determined that the HSS beam members were Category A details at their extreme fibers and that the 133 MPa maximum stress range was below the 165 MPa constant amplitude threshold limit for this detail (CSA, 1994).

It should be noted that a total of ten diaphragms were attached to each interior girder in the field and to each girder during laboratory testing. Since very small differential displacements could take place in the diaphragms near the ends of the girder, stiff supports were provided at the ends of the end diaphragm locations in the lab. Figure 5–2 shows a plan view of the test specimen indicating the joint numbering system used in the numerical model, all relevant dimensions, and the test load positions.

5.2 Description of the Test Specimens and Setup

The bridge girders obtained for laboratory testing comprised the east and west 9.9 m spans beneath the north service and main lines (Figure 1–1). The specimens used for this part of the experimental investigation consisted of the northeast set of girders located under the service line. The north girder in the set of four girders was the fascia girder, which was removed at the time of bridge replacement, leaving the three other girders available for laboratory testing. Figures 5–1 and 5–3 show the dimensions of the girder and diaphragm test sections. After the girders and diaphragms were dismantled, the shear studs were removed using an oxy-acetylene torch and a hand grinder was used to make the upper surface of the top flange surface plane. Two W250×167 reinforcing sections, each of which had a steel grade meeting the requirements of CAN/CSA-G40.21-M92 350W grade, were acquired and used interchangeably in successive tests to reinforce the test specimens. For each test, a reinforcing section was positioned on the top flange of the test girder so that the centerline of the section was positioned as close as possible to the vertical centerline of the girder section at both the end support positions and the test load positions. The 24 mm diameter pre-drilled holes in the reinforcing section were then used to mark the center position of the holes that were punched through the top flange of the girder. The reinforcing beam was then bolted to the test specimen using 7/8 in. diameter grade A325 bolts and a one-half turn was provided to preload each bolt.

The test specimen was positioned in the load frame so that the hydraulic actuators were located in the desired positions along the span. The test specimens were also aligned so that the loads were applied through their centerline. Spherical surface bearing blocks ("load cups") were then secured to the test specimen so that the ends of the actuator rams fit into the cups and essentially provided a pin support at each actuator position during testing.

Roller supports were provided at the north and south end reactions of the test specimen and lateral bracing was provided to the top and bottom flanges of the girder at two locations. The lateral bracing on the top flange was provided to simulate the lateral support of the concrete slab. The bottom flange lateral bracing was provided since the diaphragm supports were incapable of providing the lateral support that was present in service by the diaphragms and adjacent girders. One set of lateral bracing was positioned between the two diaphragm positions located north of the girder midspan in the constant moment region. The other set was located between the other two diaphragms in the constant moment region that were oriented south of midspan of the girder. Figure 5–2 shows the orientation of the test specimen in the load frame and the positions of the lateral bracing along the girder span.

76

The diaphragms had to be removed in order to position the test specimens in the test frames. They were subsequently re-attached to the test specimens. The diaphragm sections were connected to the test girder using the original 7/8-in. diameter A325 bolts. All diaphragm-to-stiffener bolts were preloaded using the turn-of-nut method. The end of each diaphragm was then attached to the flexible end supports. Both the diaphragm-to-girder connection and the diaphragm spring support details are shown in Figure 5–3. Figure 5–4 and Figure 5–5 show different views of the overall test setup.

In order to carry out the low temperature tests, insulated chambers were built around the diaphragm locations where the longest cracks were observed during laboratory testing. Each chamber was built using 51 mm Styrofoam SM-C sheets and all joints were sealed using an all-purpose silicone epoxy that was rated to -54ºC. The chambers enclosed the full depth of the built-up test section over a 460 mm length of the girder. Figure 5–6 and Figure 5–7 show the front and backside of the insulated chambers mounted around the crack at Joints 11 and 13, respectively, during the second test. To decrease the temperature inside the insulated chambers to -50ºC, CO_2 dry ice pellets were placed on shelves within in the chambers. Figure 5–8 shows the dry ice in the bottom shelf of the chamber that surrounded the crack at Joint 13 during the final freeze test performed on the second test specimen. Fans were used during the low temperature fracture tests to circulate the cold air throughout the insulated chambers that surrounded the crack locations.

5.3 Instrumentation

Two 530 kN actuators, each with 150 mm stroke, along with the associated servo-valves, actuator controllers, and high volume pump (530 lpm), were used to apply the cyclic loads on the test specimens. The applied loads were measured using load cells that were mounted to each actuator. Two other load cells were used to measure the support reactions at the north and south ends of the test specimens.

Twelve 120 ohm, 5 mm gauge length electrical resistance strain gauges were mounted on each test specimen at midspan to monitor the strain distribution over the depth of the section and the out-of-plane displacement effects. From the strain gauge data, the girder properties and load effects at midspan were assessed during laboratory testing and compared to the results of the field test data. Figure 5–9 shows the position of the strain gauges mounted at the midspan section of each test specimen.

Six 120 ohm, 2 mm gauge length strain rosettes were mounted around the bottom of the transverse stiffener located at Joint 12, as indicated in Figure 5–10. Three rosettes were mounted on both the east and west faces of the girder to measure the strain field around the end of the stiffeners prior to the formation of cracks. It should be noted that strain

rosettes were mounted on the first two specimens only because cracking and stop-holes were present in the third specimen at Joint 12 prior to testing. The orientation of the strain rosettes is shown in Figure 5–10.

LVDTs were mounted beneath the web of the girder and beneath the spring-supported end of the diaphragm to measure the differential displacements at each diaphragm. Figure 5–11 shows the orientation of the LVDTs at a typical diaphragm location.

The out-of-plane web distortions were measured at the diaphragms located within the constant moment region with two LVDTs and a single rotational variable differential transducer (RVDT). The manner in which these instruments were mounted is shown in Figure 5–12. The need to share instrumentation with other research projects made it necessary to prioritize the measurements taken during the testing program. In test one, the out-of-plane web distortions were measured at all four diaphragm positions within the constant moment region in the early stages of the test. For test two, out-of-plane distortions were not measured because much of the required instrumentation was being used on other research projects. For test three, more instrumentation was available and the out-of-plane web distortion at two diaphragm locations was measured. The two locations monitored were the web gaps at Joints 11 and 12.

All instrumentation was monitored using National Instruments SCXI–1100 high-speed data acquisition system. All gauges and instruments were sampled at a rate of 1000 Hz and data were collected using Lab View® software. As was the case during field testing, excitation of the strain channels was provided by signals sent directly from the high-speed data acquisition, whereas external power supplies provided the excitation voltage for the LVDTs and RVDTs.

The temperature distribution within the insulated chambers was measured using 330 kilo-ohm thermistors mounted over the girder depth. Thermistor resistance readings were measured using an ohmmeter and were then converted to temperature values (in ºC) using the calibration tables provided with the thermistors. The locations of the thermistors in each of the three tests are shown in Figure 5–13.

5.4 Test Procedure

The procedure adopted for the testing of each bridge girder was as follows:

1. The reinforcing section was secured to the top flange of each girder and the specimen was placed into the load frame and positioned beneath the actuators into the testing position.

2. The end and lateral supports were mounted and the diaphragm sections were bolted to the test girder.

3. The spring supports were attached to the free ends of each diaphragm. The span lengths of the HSS beam members were set to the lengths determined from the theoretical analysis.

4. All instrumentation was mounted and the girder areas around the diaphragm positions were cleaned of paint and brushed with whitewash so that the cracks could be readily observed and measured.

5. Static tests were performed to determine the actuator loads and spring member span lengths that created the 47 MPa and 12 MPa midspan bottom fiber stresses and differential displacements representative of those presented in Table 4–7. The desired stresses were monitored by averaging the bottom fiber stresses measured on either side of the girder. The resulting load magnitudes and spring member span lengths are presented for each test in Chapter 6.

6. Dynamic testing was started using a sinusoidal waveshape and a load frequency of 2 Hz. In order to compensate for inertia forces, the maximum dynamic loads were increased and the minimum loads were decreased until the maximum and minimum test stresses and the 35 MPa stress range were achieved. The revised dynamic test load values are presented in Chapter 6. With the dynamic loads set to values that achieved the target maximum and minimum test stresses, the displacements at the ends of each diaphragm were monitored. The resulting differential displacements were then calculated to ensure that they were still representative of the values determined from the field test data. Once the displacement measurements were obtained, all the LVDTs were removed. Load control was used during fatigue testing at room temperature: in service the girder would be subjected to imposed loads rather than imposed displacements. It was assumed that small changes in stiffness due to cracking would not change the in-situ load distribution results significantly. On the other hand, the change in displacements that resulted from changes in stiffness would surely result in an unwanted change in applied loads if displacement control were adopted.

7. Monitoring of the cracks at each diaphragm location was carried out during fatigue testing in order to determine the crack patterns and the crack growth rates at each location.

8. The insulated chambers were mounted around the diaphragm locations where extensive cracking of the girder web took place and low temperature tests were performed at different stages throughout the duration of each test. During each freeze test, the chamber shelves were filled with dry ice, the fans were placed in the chambers to circulate the air, and the temperature distribution was monitored until the

temperature over the tested portion of the specimen dropped to -50ºC. The girder was loaded and the cracks were monitored. The load cases adopted during each low temperature test depended on the stage at which it was performed. For all tests carried out before the end of fatigue testing, static loads were applied to achieve a 33 MPa stress (10% higher than the maximum stress measured during field testing) in the girders at the bottom fiber-midspan position. The static loads were maintained for approximately 10 minutes and strain readings were recorded before, after, and during load application.

9. The criterion to determine when each test was completed was based on the maximum crack length present in the girders. When the maximum crack length grew to a length greater than 150 mm, it was considered that the crack was progressing at a relatively fast rate. In the field, girders with such large cracks would have to be repaired or taken out of service before this point. Final low temperature tests were performed at the end of each test under several different load cases. For the second and third specimens tested, fatigue testing of the girders was continued and the cracks were monitored after the temperature in the chamber dropped to -50ºC. This was done so that the behaviour of the cracks during low temperature cyclic loading conditions could also be assessed. For the third specimen, dynamic testing was continued for several hours while the temperature inside the chamber surrounding the crack at Joint 13 was held close to -50ºC. The crack length at this location was measured throughout the test to see if the crack growth rate changed due to the low temperature conditions. Two final static load tests were performed while the temperature in the chambers was maintained at -50ºC. The first load case performed was the application of equal loads from each actuator until the midspan bottom fiber stress reached 60 MPa. This load case simulated the situation in which the infrequent heavy rail car loads, mentioned in Section 5.2, advance across the girder in -50ºC weather when cracks in the girder have extended to lengths greater than 150 mm. The other static load test was performed while loading the girder with only one actuator until the midspan bottom fiber stress reached 60 MPa. This extreme load case was adopted to observe the effects of combined shear and moment present in the girder at the crack location during simulated winter conditions. The final two load cases were not performed until the end of each test because applying these extreme load cases at increments throughout the dynamic testing phase may have altered the measured crack growth rate in an unconservative manner.

10. Before dismantling, a final static test was performed while monitoring the strain gauges at midspan and the LVDTs measuring differential displacements at the diaphragm positions to observe the behaviour of the specimen at the end of the test.

5.5 Ancillary Tests

Material properties for the girder steel were determined using tension coupon tests and Charpy V-notch impact tests. Two tension coupons from two of the three test specimens were tested to confirm the grade of steel used for the girders. All tension coupon specimens were obtained from the web of the girders and testing was conducted in accordance to ASTM standard A370-92 (ASTM, 1992). An MTS 1000 universal testing machine was used to carry out the tension coupon tests, which were conducted at a strain rate of approximately 10 $\mu\varepsilon$/s in the elastic range and 50 $\mu\varepsilon$/s in the plastic range. Static stress values were obtained at regular intervals during the tests.

Charpy V-notch specimens were also obtained from the web of two of the three test specimens. Because the thickness of the girder web was smaller than 10 mm, the standard cross-sectional dimension for Charpy specimens, subsize specimens had to be used. The specimens had cross-sectional dimensions of 7.5 mm x 10 mm and conformed to ASTM standard A370-97a (ASTM, 1997) for three-quarter size Charpy specimens. In accordance with ASTM A370-97a, the notch was oriented so that the notch front was in the direction of the minimum dimension, i.e., in the through-thickness direction. The impact tests were conducted at three different temperatures, namely, +20° C, -25° C, and –50° C. Required test temperatures for railway bridge steel are specified in Chapter 15 of the AREA code and vary from 20° C to –23° C for grades of steel similar to the one used in the St. Albert Trail bridge (G40.8 Grade B is specified on the as-built drawings). The -50° C test temperature was selected to match the test temperature used in the full-scale specimens low temperature tests. The impact tests were conducted by a commercial laboratory.
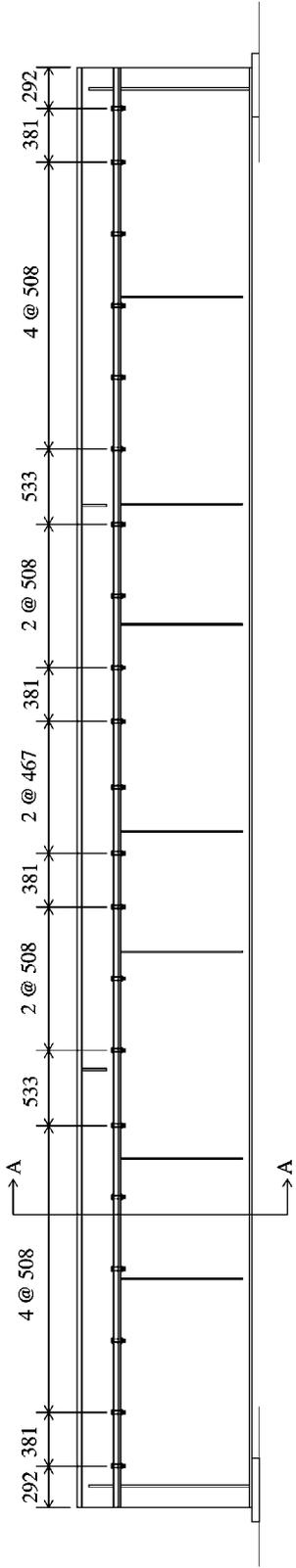
Typical Test Girder Section
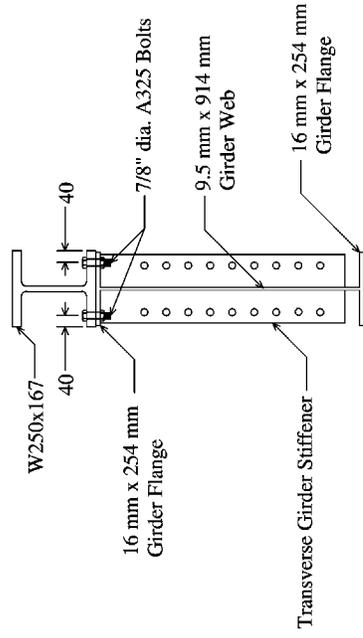
Section A-A

All dimensions in mm

Figure 5–1 Connection Details for Built-Up Test Section

82

619

1 701

619

1 701

10 204

619

1 701

619

2 950

4 000

2 950

N

② ①

Diaphragm

Base Plate at South End
Reaction Position

South Actuator

Reaction Frame Beams
(MC460x86)

North Actuator

Reaction Frame Column
(W310x143)

Column Base Plate

Reaction Frame Distributing
Beam (457 mm Deep
Built-Up Section)

Test Girder

1 062   1 062
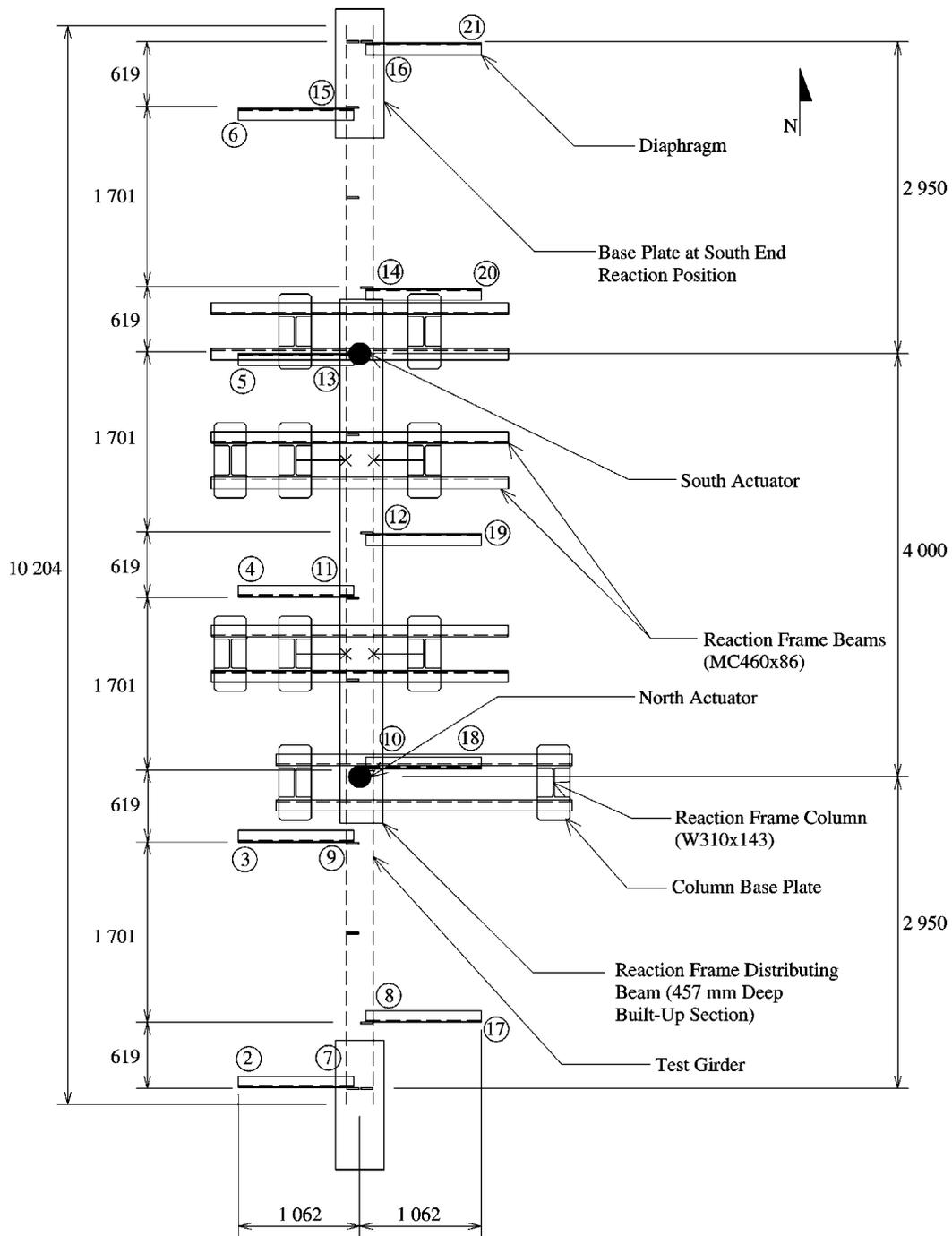
All dimensions in mm

⟶✕ Indicates position of lateral bracing along girder span

Ⓧ   Indicates joint numbering system employed in numerical
model of test setup

Figure 5–2 Plan View of Test Setup

7/8" dia. A325 Bolts

Diaphragm

Diaphragm

737

HSS 51 x 25 x 3.2
Vertical

3/4" dia.
A325 Bolts

End Roller Support

6 mm dia.
Steel Pins

1 062

1 062

Cross-Section

9.5 mm x 686 mm
Diaphragm Web Plate

6 ⟋ 75

L 102 x 102 x 9.5 Diaphragm
Flange Sections

6
6

HSS 51 x 25 x 3.2
Spring Members

Connector Plates (NS & FS)

Angle Supports

EQ

EQ

Varies

Section A-A

All dimensions in mm
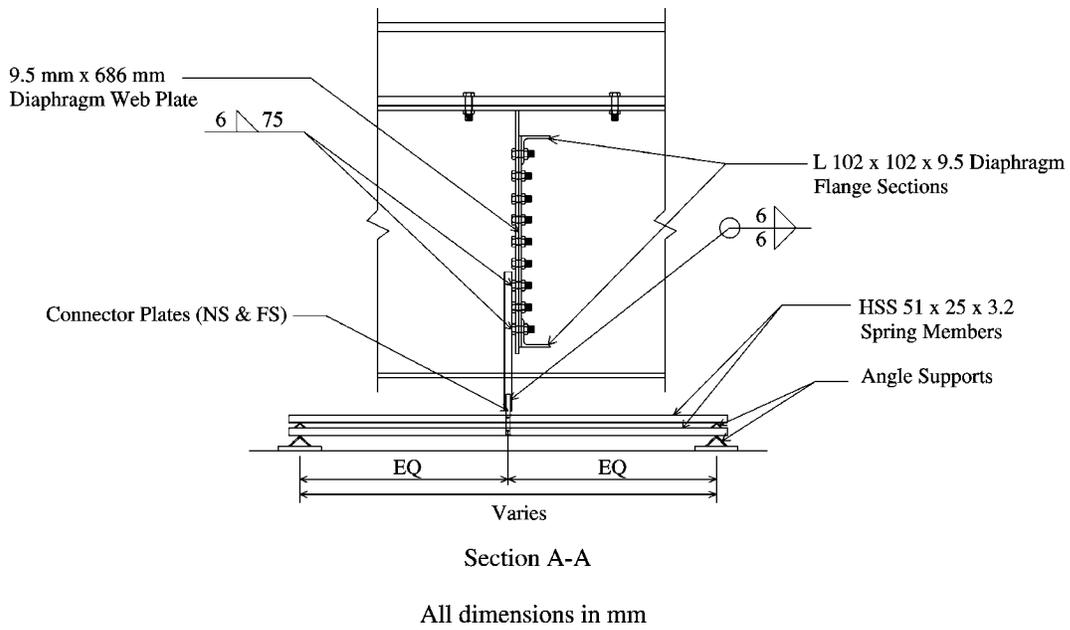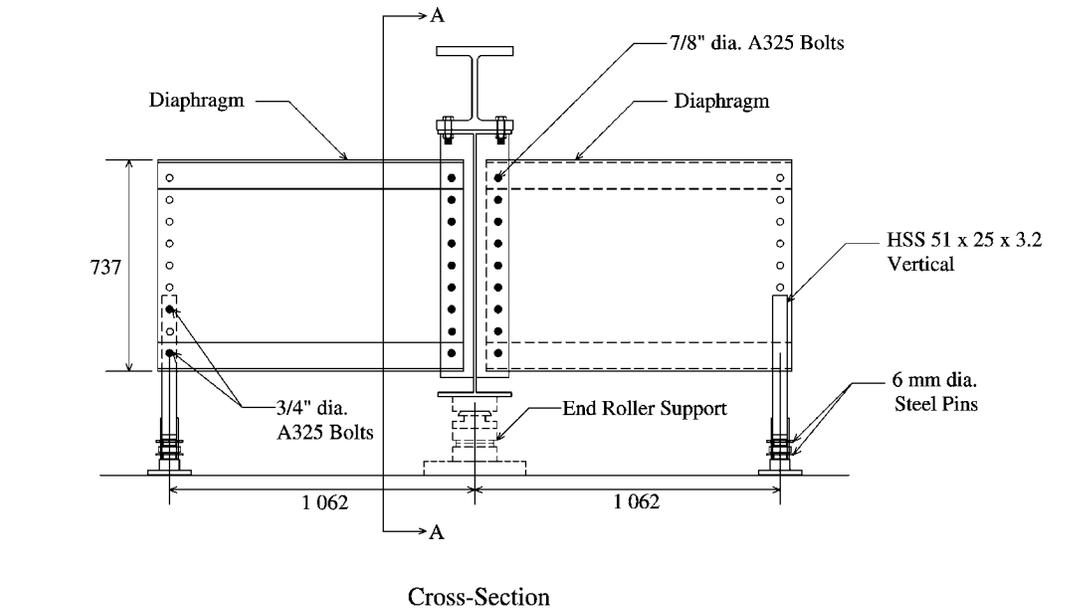
Figure 5–3 Typical Cross-Section and Spring Support Details
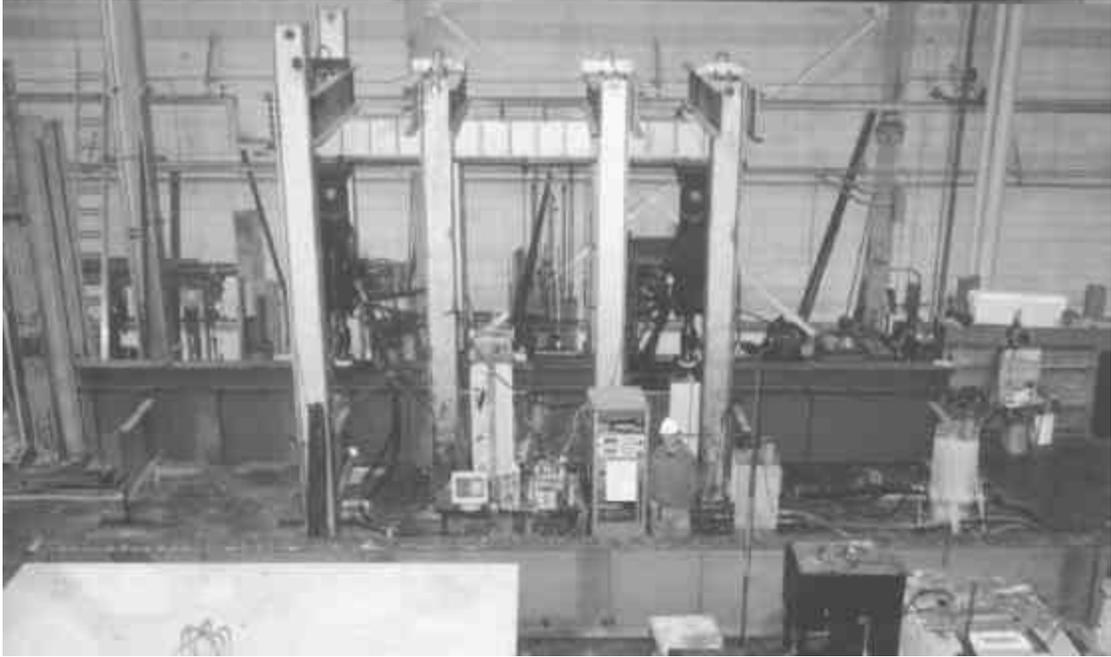
Figure 5–4 Test Specimen 1 Looking East
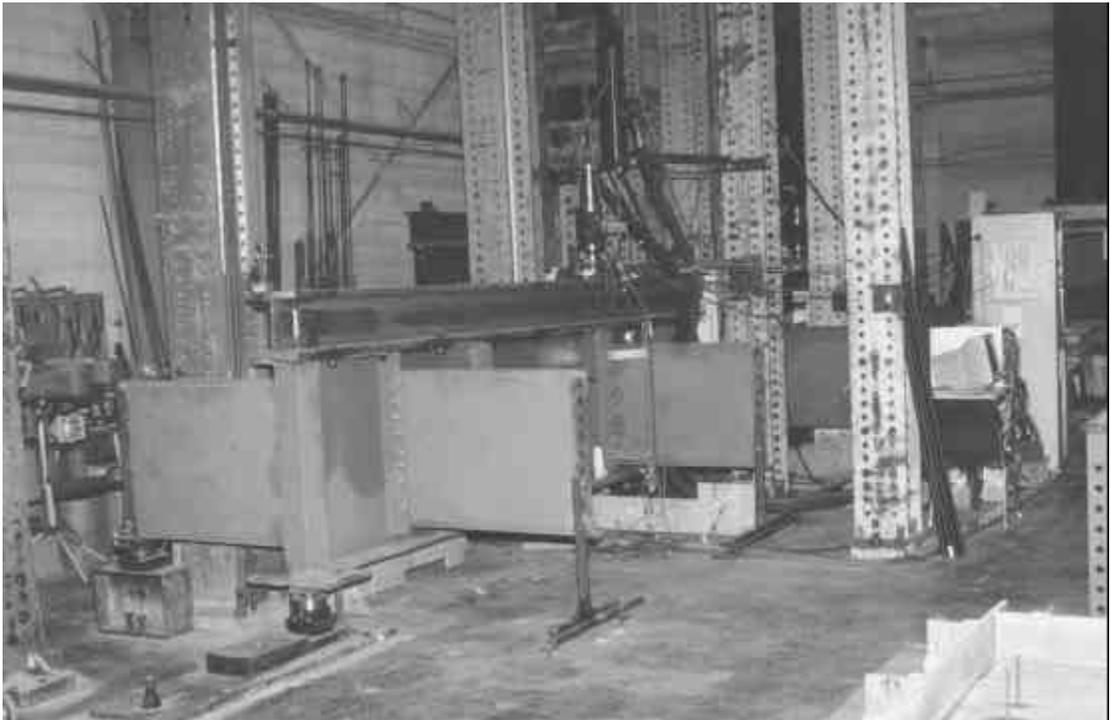
Figure 5–5 Test Specimen 1 Looking South
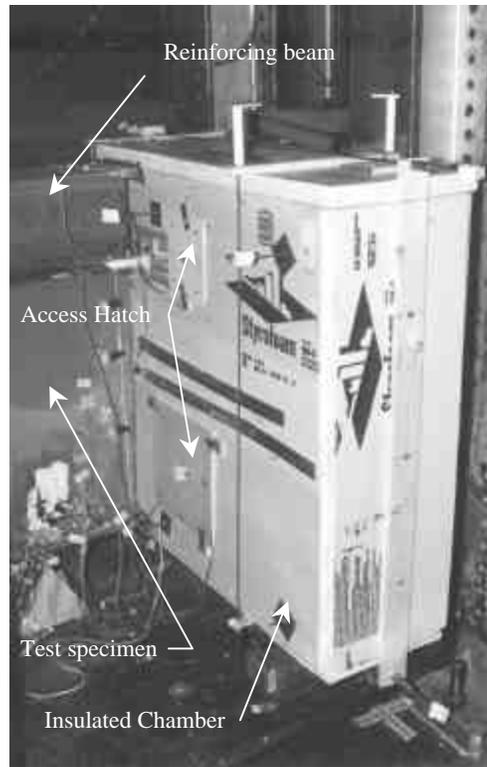
Figure 5–6 East Side of Insulated Chamber Surrounding Joint 11, Test Specimen 2
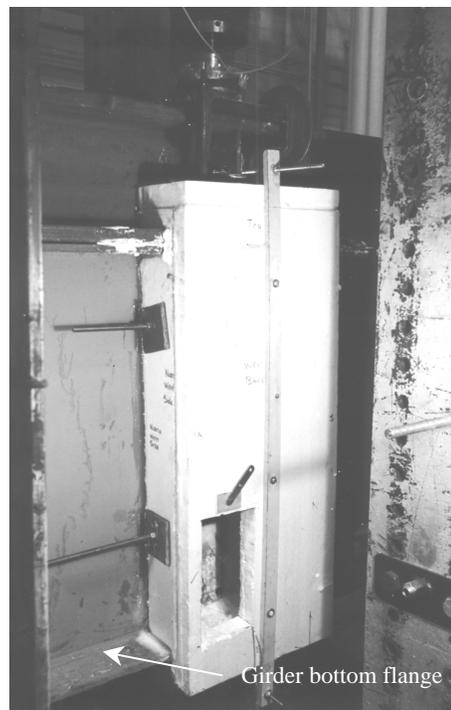
Figure 5–7 West Side of Insulated Chamber Surrounding Joint 13, Test Specimen 2

Figure 5–8 View Inside Chamber Surrounding Joint 13 During Freeze Test
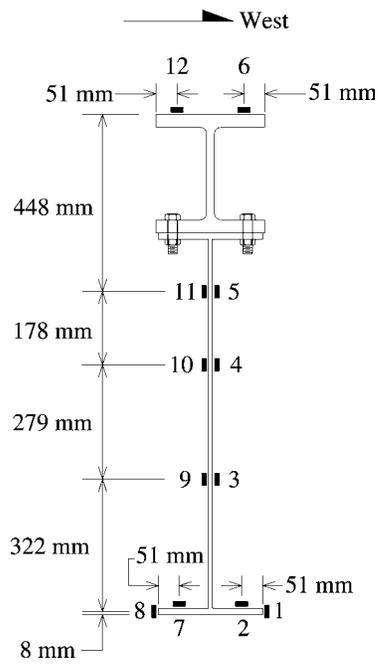
Figure 5–9 Location of Strain Gauges Mounted at Midspan of Test Specimen
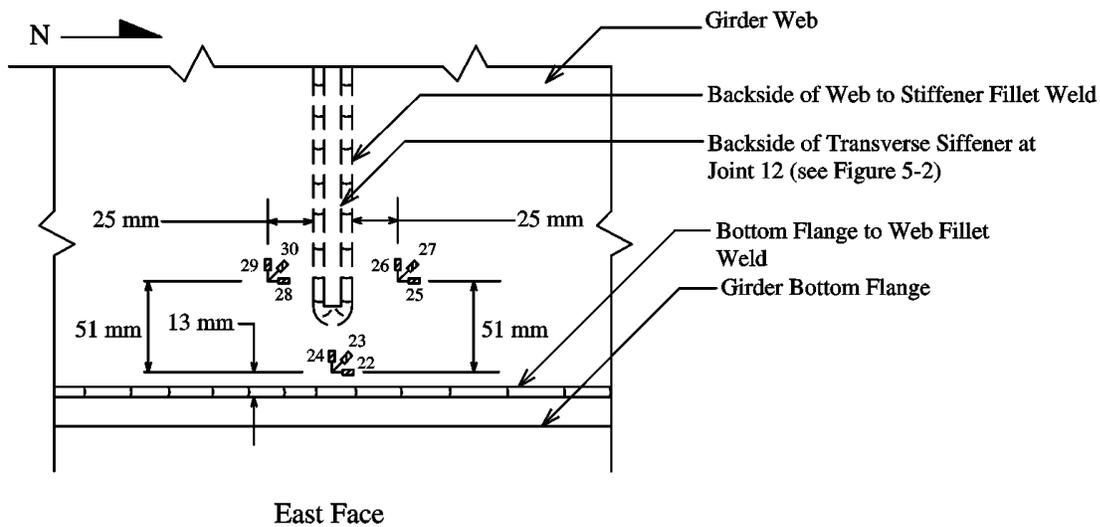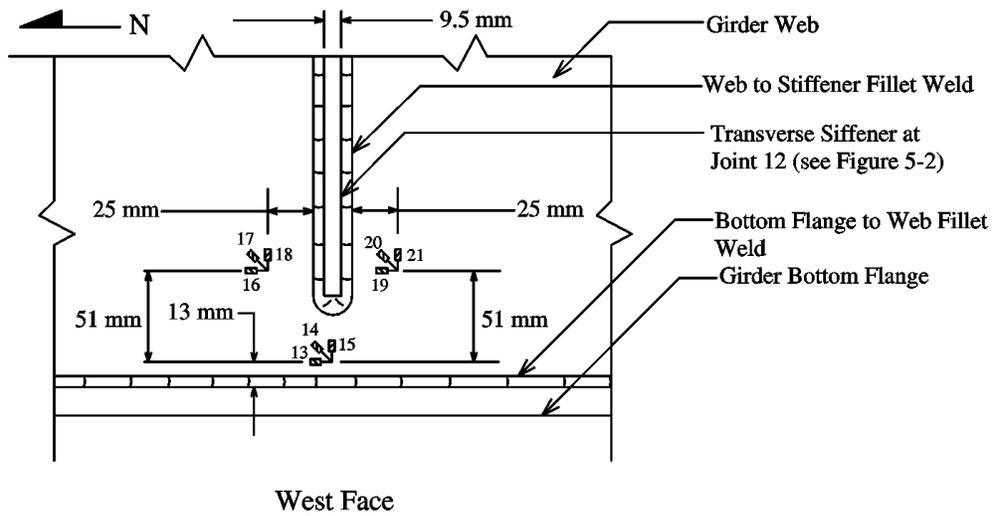
Figure 5–10 Location of Strain Rosettes at Joint 12
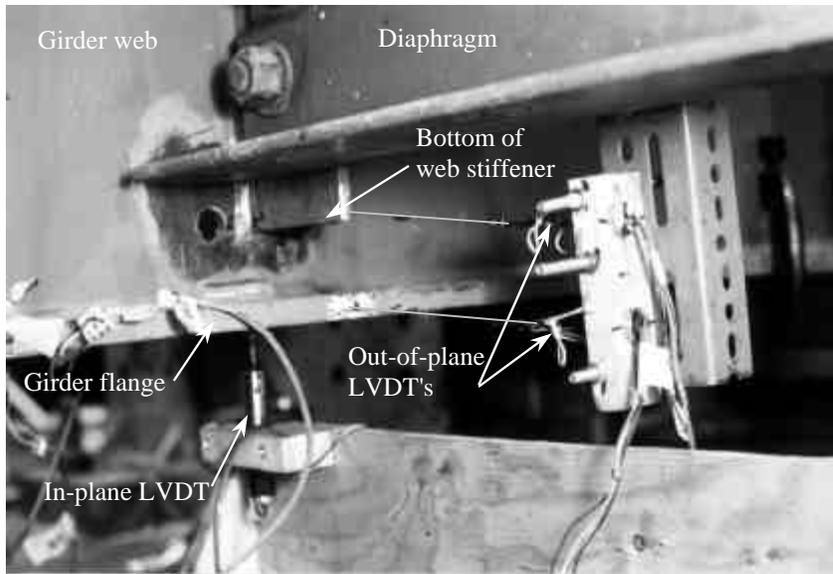
Figure 5–11 Typical Orientation of LVDT's Mounted Beneath Diaphragm Locations
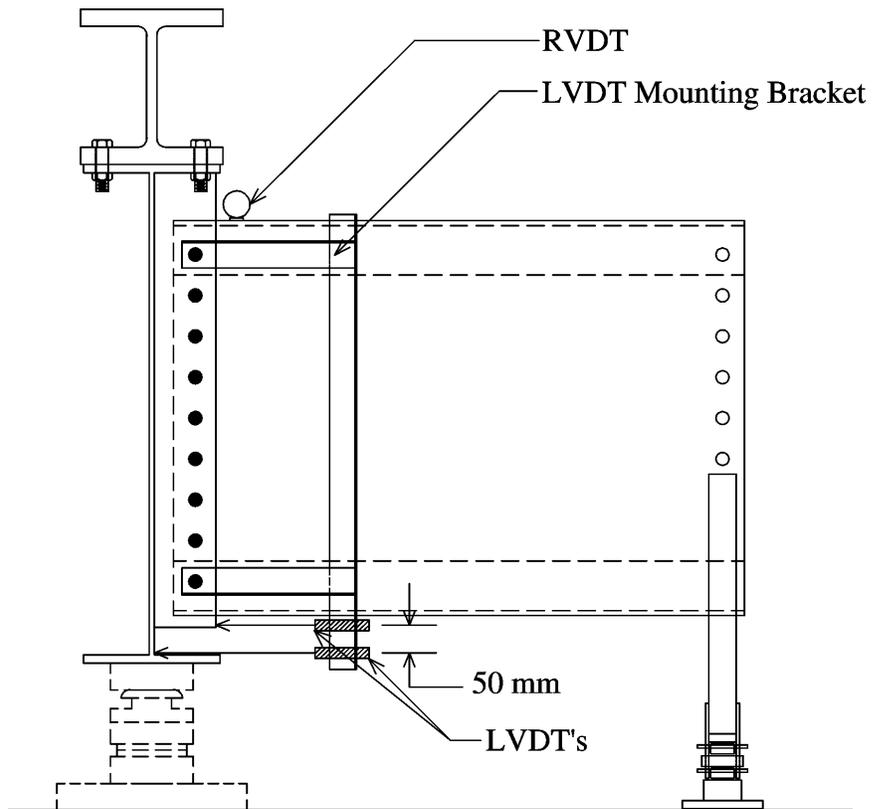
Figure 5–12 Instruments Used to Measure Out-of-Plane Web Distortion
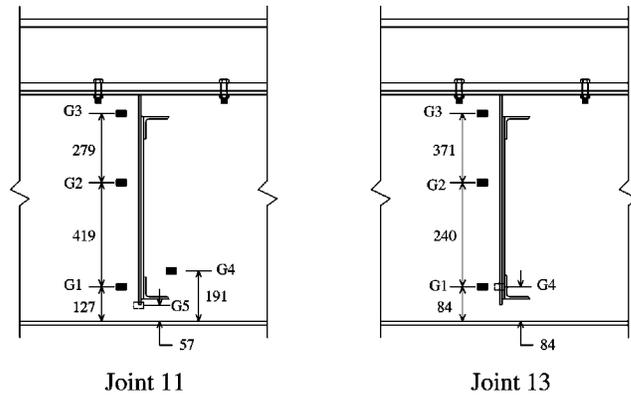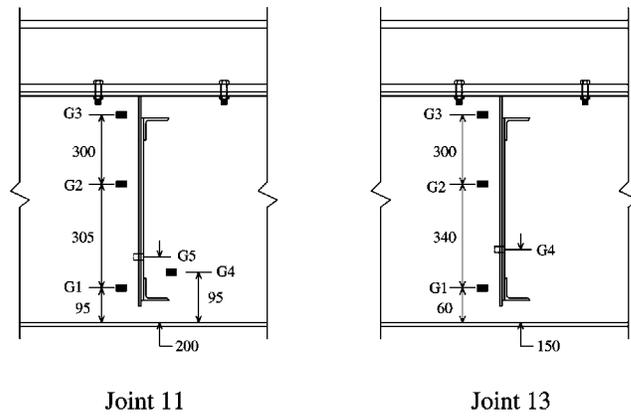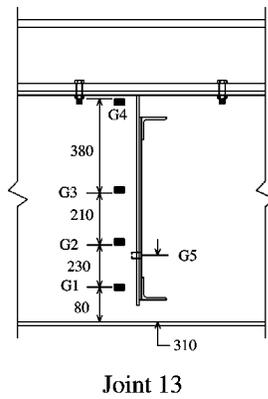
Figure 5–13 Location of Thermistors in Insulated Chambers

CHAPTER 6

TEST RESULTS, OBSERVATIONS AND DISCUSSION

6.1 Results of Full-Scale Testing Program

6.1.1 Visual Inspection of Test Specimens

The test specimens were inspected visually prior to fatigue testing in order to determine the extent of existing cracking and to identify the repairs that had been made in the girder web at each diaphragm location. The inspection for existing cracks was carried out using dye penetrant and a magnifying glass. The results are summarized in Tables 6–1 through 6–3 and the joint numbers used in the tables are shown in Figure 5–2. Figure 6–1 outlines the dimensions L1 to L4 used to describe the location of the drilled holes in Tables 6–1 through 6–3. Typical cracks and repairs on the east and west faces of a girder are presented in Figures 6–2 and 6–3. The inspection for cracks did not reveal any cases where a crack had extended past the drilled holes. As will be seen subsequently, once fatigue testing started cracks were observed beyond the drilled holes. The length, location and orientation of these cracks will be discussed later in the chapter.

6.1.2 Initial Test Conditions and Specimen Behaviour

A series of static tests were performed at the beginning of each test in order to establish the applied loads required and the span lengths of the HSS 51×25×3.2 end diaphragm supports that created the desired racking motion at the diaphragm positions. Measurements of the girder end reactions, the distortions in several of the web gap regions, and the strain field at one of the web gap locations was also recorded during static testing. The results of the initial static tests performed on each of the three test specimens are presented in the following.

Test Specimen 1

Figure 6–4 shows a typical plot of the strain readings on the east and west girder faces versus distance from the bottom flange (see Figure 5–9 for the location of strain gauges). The regression lines obtained from the test data recorded at a load level of 150 kN per actuator are also shown in the figure. The position of the neutral axis, calculated from the regression line, was determined to be 827 mm on the east face of the girder and 814 mm on the west face. The bottom fiber strain of 231 $\mu\varepsilon$ (at mid-width of the flange) was also determined from the regression analysis. Using a modulus of elasticity, E, of 200 000 MPa, the bottom fiber stress at mid-width of the flange was calculated as

46.2 MPa. The position of the neutral axis and the bottom fiber stress were both close to the experimental design values of 819 mm and 47 MPa, as outlined in Chapter 5. Since the position of the neutral axis on each girder face was close to the desired value for full composite action, the number of bolts used to attach the reinforcing beam to the test specimen (see Figure 5–1) was considered sufficient to provide 100% composite action. Furthermore, the good agreement between the theoretical and measured position of the neutral axis indicates that the moment of inertia of the built-up test section is representative of the moment of inertia of an interior composite girder in the bridge before dismantling (see Section 4.3.1). The minimum static load required to achieve a bottom fiber stress of 12 MPa at midspan was determined to be 45 kN from each actuator.

Table 6–4 lists the displacements and the resulting differential displacements measured using LVDTs mounted at each diaphragm position (see Figures 5–2 and 5–11) at the peak testing load of 150 kN per actuator. Also tabulated in Table 6–4 are the actual span lengths of the HSS members used to support the ends of the diaphragms. A comparison between the differential displacements determined from the field data (see Table 4–7) and those measured in the lab shows that the lab values were representative of the field values. A comparison of the lab and field vertical deflections indicates that the displacements measured in the lab specimens were significantly larger than the corresponding field values. There are two main reasons for this. First, the bottom fiber stress at midspan was increased from a service maximum value of 30 MPa to 47 MPa for testing purposes in order to ensure there would be no stress reversal in the test specimens during testing. Second, the maximum girder service effects occurred while three locomotive axles were on the test span during the field test whereas in the laboratory the effects from these three axle loads were replicated with only two hydraulic actuators. Hence, the service loads were better distributed along the girder span than the test loads, which would result in smaller field deflections for the same bottom fiber stress.

For the maximum test loads of 150 kN per actuator, the north and south girder end reactions were measured to be 127 kN and 130 kN, respectively. Using the displacements measured at each diaphragm end support and the tabulated moment of inertia for the sections used for the diaphragm supports, the reaction force at each diaphragm support was calculated. Table 6–5 summarises the calculated diaphragm end reactions. The total load transferred through the diaphragms and down into the diaphragm end supports was determined to be 48 kN (24 kN north of midspan and 24 kN south of midspan). If these diaphragm end reactions are added to the measured beam end reactions, the total reaction is 305 kN, compared to the 300 kN force applied to the test specimen. The measured and calculated reactions are therefore in good agreement with the applied loads.

92

The stresses in the web gap region at Joint 12 are presented in Table 6–6. The stresses were obtained by multiplying the measured strains by the modulus of elasticity (see Figure 5–10 for the orientation of the rosettes). Table 6–6 also presents the principal stresses and direction of the major principal plane at each strain rosette location. The results presented in Table 6–6 show that the vertical stresses near the top of the web gap (gauges 18 and 21 on the west face and gauges 27 and 30 on the east face) are tensile on the west face (stiffener side) and compressive on the east face. Near the bottom of the web gap (13 mm up from the bottom flange of the girder) the calculated east and west face vertical stresses were 21.0 MPa (gauge 24) and 14.3 MPa (gauge 15), respectively. These tensile stresses were on the order of one-half the vertical stresses measured near the top of the web gap. The smaller magnitude of these stresses and the fact that both faces were in tension suggest that the bottom strain rosettes were probably mounted near a point of inflection in the web gap. The maximum value of major principal stress determined from the strain rosettes (gauges 19 through 21) was 66.2 MPa, which is well within the typical 10 MPa and 97 MPa range of web gap stresses reported by Fisher and Keating (1989).

Distortion measurements at the top and bottom of the web gap at Joint 12 are consistent with the measured web gap stresses presented above. At the maximum static load level, the out-of-plane displacement of the web at the top and bottom of the gap, measured relative to the stiffener, is 0.00053 mm to the west and 0.0455 mm to the east. This corresponds to a web gap distortion of 0.046 mm. These measurements show that the top of the web gap was being pulled westward toward the end of the diaphragm and that the bottom of the web gap was restrained from westward movement by the relatively stiff girder bottom flange. The resulting distorted shape is similar to the web distortion shown in the web gap of the most heavily deflected girder shown in Figure 2–1 (i.e. the right girder). This observed web distortion should give rise to compressive strains on the east face of the web at the top of the web gap and tensile strains on the east face at the bottom of the gap, which is consistent with the strain measurements presented above.

The measured web gap distortion of 0.046 mm at Joint 12 is larger than the 0.025 mm maximum distortion measured by Fisher and Keating (1989) on similar web gap details in highway bridges under normal truck traffic. The reason for this discrepancy can be attributed to several factors, including the detail of the web gap (length of the web gap, web thickness, restraint provided by the flange and stiffener), the extent of cracking in the gap region, the applied loads on the bridge structure, and the racking motion in the diaphragm (a direct effect of the relative displacement between two adjacent girders).

The web gap distortions were also measured at the other diaphragm locations between the two load actuators (Joints 10, 11, and 13). At Joints 10, 11, and 13, the gap distortions were 0.0034 mm, 0.047 mm, and 0.1214 mm, respectively. All gap distortion

measurements showed that at the top of the gap the web was being pulled towards the diaphragm and at the bottom of the gap the web was being restrained by the girder bottom flange. This is consistent with the boundary conditions and loading conditions used in the tests (downward displacement at the girder-diaphragm junction relative to the supported end of the diaphragm).

Test Specimen 2

Figure 6–5 shows the strain gauge readings (recorded at a load level of 152 kN per actuator) plotted versus the distance from the bottom flange of the built-up test section at midspan. The figure also shows the linear regression lines obtained from both the east and west face strain readings. The position of the neutral axis was found to be 827 mm on the east face of the girder and 780 mm on the west face. These values are in good agreement with the theoretical position of the neutral axis (819 mm). The bottom fiber stress at mid-width of the flange was determined to be 46.6 MPa, which also is very close to the experimental design value of 47 MPa. The loads required to achieve a 12 MPa midspan bottom fiber stress were determined to be 43 kN per actuator. The maximum and minimum actuator loads of 152 kN and 43 kN, respectively, are in good agreement with the corresponding 150 kN and 45 kN loads that were determined for the first lab test.

Table 6–7 lists the displacements and the resulting differential displacements at each diaphragm position at the peak-testing load of 152 kN per actuator. The span lengths of the diaphragm end support members are also listed in Table 6–7. Both the displacements and differential displacements in Table 6–7 are similar to those tabulated in Table 6–4 for the first test specimen. The differential displacements outlined in Table 6–7 are also in good agreement with those determined from the field test data (see Table 4–7). At the maximum static load level of 152 kN per actuator, the north and south girder end reactions were measured to be 126 kN and 127 kN, respectively. Table 6–8 summarises the findings from the diaphragm end support reaction analysis at the maximum static load level. The total load transferred through the diaphragms and down into the diaphragm end supports was determined to be 51.9 kN, making the total reaction load equal to 304.9 kN, which is essentially equal to the 304 kN force applied to the test specimen with the actuators.

The stresses in the web gap region at Joint 12 are presented in Table 6–9. A comparison of the stresses in the first test (Table 6–6) and the second test indicates that the vertical stresses at the top of the web gap (gauges 18 and 21 on the west face and gauges 27 and 30 on the east face) were noticeably larger in the first test than in the second test. The difference in the measured web gap stresses can be attributed to such factors as small variations in the mounting positions of the strain rosettes and the difference in restraint at

the web gap boundaries, mainly due to the degree of initial cracking in each test specimen. Although the magnitude of the stresses were different in the two tests, the stresses in the second test were still compressive on the east face and tensile on the west face at the top of the web gap, and tensile near the bottom of the gap on the west face. (Gauge 24, mounted on the east face at the bottom of the gap, was not responding during the test.) The top gap stress directions reflect the theoretical stresses expected at this location (see Figure 2–1). Lastly, the maximum value of the major principal stress determined from the strain rosettes (gauges 16 through 18) was 46.1 MPa, which is also well within the range of web gap stresses reported by Fisher and Keating (1989).

Test Specimen 3

Figure 6–6 shows the strain readings and linear regression lines from a representative initial static test performed on the third test specimen. At a static load level of 150 kN per actuator, the neutral axis position obtained from the strain gauges on the east and west face of the girder web was 821 mm and 830 mm, respectively. Furthermore, the bottom fiber stress at the center of the flange was calculated to be 45.8 MPa from extrapolation of the regression curves. The position of the neutral axis and the bottom fiber stress are both representative of the theoretical design values and the values obtained from the initial static tests performed on the first two test specimens.

Table 6–10 presents the span length for the diaphragm end supports, and the deflections and differential displacements at each diaphragm position. Comparisons between Tables 6–4, 6–7, and 6–10 indicate that the displacements at each of the spring supported diaphragms at the beginning of all three tests were very similar and the resulting differential displacements of the diaphragm ends are representative of field conditions (see Table 4–7).

At the maximum static load level, the girder end reactions were each measured to be 129 kN. Table 6–11 summarises the analysis that was done to determine the loads resisted by the spring supports at the ends of the diaphragm members. The total load resisted by the diaphragm end supports is 48.9 kN, yielding a total reaction of 307 kN when added to the girder end reactions. This is in good agreement with the total applied load of 300 kN.

The web gap distortions at Joints 11 and 12 were also monitored during initial static testing. At Joint 12, the measured out-of-plane displacement of the web at the top and bottom of the web gap are 0.0012 mm to the west and 0.0780 mm to the east, respectively, yielding a web gap distortion of 0.0899 mm. Once again, the measured distortions fit the theoretical model shown in Figure 2–1 since the top of the gap was being pulled westward towards the end of the diaphragm and the bottom web gap region

was restrained by the girder bottom flange. Even though the distorted shape of the web gap was the same as the shape observed in the first test, the magnitude of distortions at Joint 12 in the first and third tests were significantly different. The distortion at Joint 12 in test specimen 3 is about twice that of test specimen 1, even though similar racking motions, which produces the concentrated distortions in the gap regions were present in each test. From the initial inspection results at Joint 12 (see Table 6–1 and Table 6–3), it can be seen that the web gap region was more flexible in the third test specimen because of the presence of cracks and drilled holes near the top of the gap boundary. Hence, it is plausible that the measured distortions at Joint 12 in the third test specimen would be larger than those measured in the first specimen.

The web gap distortion measurements made at Joint 11 in the third test were found to be highly unreliable and therefore they are not presented here. The measurements showed that the distortions were larger than the distortions measured in all other gaps during the testing program and that the bottom of the web gap was being pulled towards the diaphragm and the top of the web gap was moving westward away from the diaphragm. The displaced directions at the top and bottom of the web gap are not representative of the conditions at the gap location (downward displacement at the girder-diaphragm junction relative to the supported end of the diaphragm), nor are they representative of the theoretical distortion model (see Figure 2–1) or the measurements made in the other web gaps. The difficulty in mounting the LVDTs in the web gap region is likely the reason why the measurements are unreliable.

A comparison of the web gap distortions measured in the test specimens with the distortion measured near the midspan of Girder 3 during the field test (see Section 4.3.5) shows a poor correlation between the field and lab measured values. The manner in which the LVDTs were mounted during field testing is likely to be the main source of discrepancy in these measurements. In the field, a single LVDT was attached to the girder web on the backside of the stiffener and mounted to a magnetic base that rested on the girder bottom flange. Under load, it is possible that the girder bottom flange rotated relative to the web and, subsequently caused the measured distortion of the web gap to be less than it actually was. In the laboratory, two LVDTs were used at each location to measure the distortions at the top and bottom of the web gap. Also, the LVDT mounting bracket shown in Figure 5–12 eliminated any effect of the relative rotation of the girder bottom flange to the web.

The fact that the web distortions are very small makes it very difficult to measure these displacements with a reasonable level of accuracy. Even though the accuracy of the web gap distortions measured during field testing are suspect, the lab test setup was designed to replicate the in-situ in-plane girder stresses and the racking motion of the diaphragm members. As mentioned in Section 2.4, the magnitude of the web gap distortions are not

only small, but like the web gap stresses they are highly dependent on the localised conditions (such as fatigue cracking) in the gap region. On the other hand, the diaphragm racking motions, which induce the distortions and secondary stresses in the gap region, are caused by the global response of the structure and correlating these differential displacements in the lab to the field values is more practical.

6.1.3 Fatigue Testing

After it was established that the behaviour of each test specimen was representative of field conditions, fatigue testing was started at a load cycle frequency of 2 Hz. As explained in Chapter 5, the maximum and minimum actuator loads had to be adjusted to achieve the desired stress range without reversal of stress. At a cycling frequency of 2 Hz, the maximum and minimum actuator loads were 195 kN and 15 kN, respectively. This corresponded to maximum and minimum bottom fiber stresses of 47 MPa and 12 MPa, respectively. After the dynamic loads were set, the displacements and resulting differential displacements at diaphragm positions were checked to ensure that they remained unchanged from those determined during initial static tests. In each test, the end displacements of the diaphragms were observed to be virtually the same as the static values presented in Tables 6–4, 6–7, and 6–10.

The fatigue crack growth rates and the locations and orientations of the observed fatigue cracks are presented for each of the three test specimens in the following. In each test, multiple fatigue cracks were observed in the girder web at the diaphragms located between the north and south actuators (Joints 10, 11, 12, and 13). Only the results for the critical cracks are presented in this chapter. The crack growth rate curves for all non-critical fatigue cracks are presented in Appendix A.

Test Specimen 1

At the start of fatigue testing the extent of initial cracking in the girder at each diaphragm position was visually inspected using a magnifying glass. The results indicated that the initial crack inspection results, outlined in Table 6–1, were accurate. From the onset of cyclic testing until approximately 1.2 million cycles, when new cracks started to form, crack movement at each web gap location was restricted to the opening and closing ("working") of existing cracks. The observed tearing deformation of the distortion-induced fatigue cracks in all three-laboratory tests suggests that Mode III loading (tearing, or antiplane shear mode) was the dominant mode initiating and propagating cracking in the girder web gaps.

At 1.2 million cycles the cracks at Joints 11 and 13 began to propagate past the drilled holes and up the web on the east face of the girder. Up to approximately 3.27 million

cycles all cracks were part-through thickness cracks and the crack growth rate at both Joint 11 and 13 were determined from regression analysis of the first portion of the crack length versus load cycle plots presented in Figure 6–7 to be about 1 mm per 50 000 load cycles. Shortly after 3.27 million cycles, the cracks at Joints 11 and 13 advanced through the web thickness and became through thickness cracks. At this stage the crack growth rate increased to approximately 5 mm per 50 000 load cycles at both locations. Figure 6−7 shows the growth rates of the fatigue cracks at Joints 11 and 13 measured on the east and west faces of the web. A comparison of the east and west face crack growth rates indicates that the rates are essentially equal, but the west face cracks are shorter than the east face cracks. This suggests that the crack fronts were inclined through the web thickness. The orientation of the cracks on the east and west faces of Joints 11 and 13 are shown in Figures 6–8 through 6–11.

It should be noted that the zero crack positions reported on the crack growth rate curves represent the position of the cracks at the start of the fatigue test. The crack lengths reported in Figure 6–7 were measured from the edge of the drilled holes. The actual position of the crack tip at the start of fatigue testing is shown in Figures 6–8 through 6−11. At 4.23 million cycles, the cracks at Joints 11 and 13 had grown to 170 mm and 152 mm, respectively. These crack lengths met the end of test criteria outlined in Section 5.4, and so fatigue testing was stopped and final, low temperature tests were performed. Results and discussions on all low temperature tests carried out for the first test specimen are presented in Section 6.1.4.

Test Specimen 2

Shortly after fatigue testing started, the extent of initial cracking in the second test specimen was assessed visually with a magnifying glass and results similar to those tabulated in Table 6–2 were found at all joint positions except at Joint 11. On the east face of Joint 11 existing cracks on both the north and south sides of the transverse stiffener were observed to have advanced past the drilled holes and up the web-to-stiffener weld toe. On the north side of the stiffener, the crack had advanced past the hole by about 10 mm prior to the start of the fatigue test, and on the south side of the stiffener the crack was found to have advanced 13 mm past the point of intersection of the drilled hole and the crack.

During the initial stage of fatigue testing, crack movement was limited to the "working" of existing cracks. Although fatigue cracks had propagated beyond the drilled holes at Joint 12 at the beginning of the test, it was not until 850 000 cycles that the cracks began to propagate noticeably up the east face of the web on both the north and south sides of the stiffener. A possible reason why the cracks did not propagate from the start of fatigue testing is that the area surrounding the cracks may have been overloaded during handling

of the test specimen in the field and during transportation to the laboratory. An overload of the specimen would have caused a retardation of the fatigue cracks at the start of testing.

At 2.8 million load cycles, the crack on the north side of the stiffener at Joint 11 stopped and additional crack growth from that point onward was restricted to the crack on the south side of the transverse stiffener. At Joint 13, noticeable crack movement was restricted to the existing through thickness lateral crack (see Figures 6–15 and 6–16) until 2.6 million cycles, when a large vertical crack was observed on the east face of the web. As was the case in the first test, the cracks at Joints 11 and 13 advanced through the thickness of the web to the west face and became through thickness cracks at about 3.2 million cycles. Figure 6–12 shows the crack growth rate curves for the cracks at Joints 11 and 13. At Joint 11, the crack on the west face of the web remained shorter than the crack on the east face, suggesting that the crack front was not at a right angle to the web surface. On the other hand, the crack front at Joint 13 was essentially perpendicular to the web surface since the length of the crack on the east and west faces was essentially equal. After the crack at Joint 11 first surfaced on the west face and became a through thickness crack, the crack growth rate increased from 1 mm per 50 000 cycles to 2 mm per 50 000 cycles. A rate increase from 1 mm per 50 000 cycles to approximately 3.5 mm per 50 000 cycles was observed at Joint 13 after the part-through thickness crack surfaced on the west face and became a through thickness crack. The orientations of all cracks at each of these joints are shown in Figures 6–13 through 6–16. The zero positions, representing the position of the crack tip at the start of fatigue testing, are shown in these figures.

Fatigue testing was stopped at 4.71 million cycles when the east face crack at Joint 13 reached a length of 192 mm, well beyond the 150 mm length chosen as the minimum crack length required to stop each test. After the insulated chambers were removed from Joints 11 and 13, final crack inspections were performed. At Joint 11 a vertical crack that originated where the initial crack intercepted the bottom of the north drilled hole and extended 45 mm downward to the flange-to-web junction was detected (see Figures 6−15 and 6−16). Since the crack was not observed during testing, the crack surface was obtained to determine whether fatigue or fracture under low temperature conditions was the cause of crack initiation and propagation. The crack surface appeared very similar to all other fatigue crack surfaces obtained from the testing program, which suggested that crack growth was due to high-cycle fatigue.

Test Specimen 3

Once again, a visual inspection was conducted at the beginning of fatigue testing to determine the extent of initial cracking in the test specimen. At Joint 13, it was noticed

that the initial crack had extended past the drilled hole and up the toe of the web-to-stiffener weld on the south side of the stiffener by 23 mm. This crack began to propagate noticeably along the weld toe shortly after fatigue testing started (at approximately 150 000 cycles). This is much earlier than the cycle at which the cracks in the first and second test specimens were first observed to have started to propagate past their initial positions.

Figure 6–17 shows the crack length versus load cycles for the cracks at Joint 13. In Figure 6–19 it can be seen that the crack propagated through the thickness of the web and surfaced on the west face at approximately two million cycles. The precise cycle at which the crack surfaced on the west face of the girder is unknown since it occurred overnight. At two million cycles the crack had not surfaced, but at 2.22 million cycles the crack on the west face had already reached a length of 80 mm. After the crack at Joint 13 surfaced on the west face of the girder web and became a through thickness crack, the crack growth rate increased from 2 mm per 50 000 cycles to approximately 4.5 mm per 50 000 cycles. From Figure 6–17, it can be seen that the crack on the east and west faces grew at essentially the same rate. The crack front also appeared to remain perpendicular to the web surface since the crack was essentially the same length on the east and west faces each time crack length measurements were made.

Fatigue testing was stopped at 3.71 million cycles because the crack at Joint 13 had reached a length of 247 mm. The orientation of the crack on the east and west faces of Joint 13 were observed to be the same as those observed at Joint 11 during the first test (see Figures 6–8 and 6–9). It should be noted that the maximum crack length measured in the third test specimen at all other diaphragm locations was 75 mm. As previously mentioned, the crack growth rates for these smaller cracks are presented in Appendix A.

Comparison of Fatigue Test Results

In the first and second tests, the following similarities in the behaviour of the critical fatigue cracks were observed:

1. The critical cracks were located at Joints 11 and 13;

2. The initial crack growth rate was approximately 1 mm per 50 000 cycles;

3. The crack growth rate increased significantly at about 3.2 million cycles;

4. The critical cracks did not reach a length of 150 mm (chosen failure criteria) until after four million load cycles were applied to the test specimen.

Differences in the behaviour of the cracks in the first and second tests were also observed. In the first test, the cracks at Joints 11 and 13 began to propagate at 1.2 million

cycles, whereas in the second test the cracks at Joint 11 started at 850 000 cycles and at Joint 13 crack propagation did not start until 2.6 million cycles. The cracks at Joints 11 and 13 in the first test specimen propagated along the toe of the web-to-stiffener fillet weld, whereas in the second specimen the cracks were inclined at an angle of about 15° from the axis of the stiffener. Also, cracking was present on both the north and south sides of the transverse stiffener at Joint 11 in the second test. Lastly, the vertical fatigue crack that extended downward from the north stop hole to the flange-to-web junction was only present at Joint 11 in Test Specimen 2 (Figure 6–13). The cracks on the north side of the stiffener extending above and below the drilled hole may have relieved the driving force on the crack on the south side of the stiffener, thus resulting in smaller crack lengths at Joint 11 in the web of Test Specimen 2 (see Figures 6–7 and 6–12).

A comparison of the results of all three tests shows a number of significant differences in the behaviour of Test Specimen 3. These differences are outlined below.

1. Crack extension was noticed from the start of fatigue testing, almost 1 million cycles before crack extension was observed in the first and second test specimens;
2. The critical crack developed at Joint 13;
3. The initial crack growth rate was 2 mm per 50 000 cycles, which is double the initial crack growth rate observed in the other two tests;
4. The sharp increase in the crack growth rate occurred at approximately 2 million cycles, whereas, in the other tests this rate increase was observed at over 3 million cycles;
5. A crack length of 150 mm was reached at 2.9 million cycles, over one million cycles before the cracks in the other test specimens reached the same length.

These differences in crack behaviour in Test Specimen 3 can be attributed to the relatively long fatigue crack (23 mm) that had already formed above the repair hole before the start of testing.

Some similarities in crack growth behaviour in all three specimens were observed. The sharp increase in the crack growth rates occurred when the part-through thickness cracks finally surfaced on the west face of the girder web (backside of the stiffener/diaphragm position) and became through thickness cracks. Furthermore, all critical fatigue cracks occurred at joints where repair holes had been drilled at the crack tips. This indicates that hole drilling was not effective at arresting distortion-induced fatigue cracks in these girders. Lastly, crack initiation and propagation was observed to be mainly due to Mode III loading (tearing or antiplane shear mode).

6.1.4 Results of Low Temperature Tests

As described in Section 5.4, a series of low temperature tests was performed during the fatigue testing process in order to assess the stability of the fatigue cracks at low temperature. In the first test, two overload tests, described in Section 5.4, were performed at Joint 11 and at Joint 13 at the end of fatigue testing and five other low temperature tests were performed at regular intervals during fatigue testing. All the cracks tested at low temperature remained stable. This suggests that fatigue crack growth remained sub-critical, even at the end of the test when the crack lengths at Joints 11 and 13 were 152 mm and 170 mm, respectively. The loading and temperature conditions used during each low temperature test are summarised in Table $6-12$.

The number of low temperature tests performed on the second and third specimens was reduced since the low temperature tests carried out during the first test did not induce fracture. In the second test, the insulated chambers were once again installed around Joints 11 and 13 and a total of six low temperature tests were performed. The last low temperature test, which was carried out at the end of the fatigue test (at 4.71 million cycles), consisted of lowering the temperature in the chamber surrounding Joint 11 to approximately -50° C and loading the beam cyclically under the same load range employed during the room temperature fatigue test. The low temperature cyclic test was conducted for approximately 45 minutes and no crack growth was observed. (At the crack growth rate measured at room temperature, the expected crack extension over 45 minutes would have been 0.5 mm, which would have been very difficult to detect in the cold chamber.) Static loads were applied to the second test specimen during the other five low temperature tests. The conditions during each of these tests are presented in Table $6-13$. Once again, the cracks at Joints 11 and 13 remained stable during the low temperature tests.

A total of three low temperature tests were performed on the third test specimen. Since significant cracking was only observed at Joint 13, the low temperature tests were only performed at this location. All tests were performed near the end of fatigue testing and the last two tests consisted of the overload static cases outlined in Section 5.4. The load and temperature conditions during the low temperature static tests are summarised in Table 6–14. The 247 mm long crack present in the girder web remained stable under both simulated extreme service temperature conditions and extreme service loading conditions.

The first low temperature test performed on the third specimen consisted of fatigue testing the girder for 3.5 hours while the temperature in the chamber at Joint 13 was maintained near -50° C. The temperature in the chamber stabilised near -50° C at 3 553 960 cycles and was maintained up to 3 579 800 cycles. Figure 6–18 shows the

temperature readings taken throughout the test for each of the thermistors mounted on the east and west faces of the girder in the chamber. (See Figure 5–13 for the location of the thermistors in the chamber.) The large fluctuation in the temperature measured by gauge 5 is not a concern since this gauge was mounted near the top of the built-up section, approximately 570 mm from the crack front. Before the test started, the cracks were marked so that the rate of crack growth during the low temperature cyclic test could be assessed. The fatigue crack extended 2.8 mm during the low temperature cyclic test, which corresponds to a crack growth rate of 5.4 mm per 50 000 cycles. This rate is only marginally greater than the 4.5 mm per 50 000 cycle rate determined for the same crack at the end of room temperature fatigue testing. Considering the fact that the crack growth rate would likely continue to increase rapidly as the fatigue cracks got longer, the small increase in crack growth rate observed during the cyclic low temperature test is probably not significant.

6.1.5 Specimen Behaviour at End of Tests

At the end of fatigue testing a room temperature static test was performed at the maximum initial static test load (refer to Section 6.1.2) to observe the change in behaviour of each specimen after significant fatigue cracking. The strain gauges mounted at midspan of each girder, the load cells measuring the end reactions of the girders, and the LVDTs used to measure the diaphragms displacements were monitored during this final static test. The results obtained from the final static tests included the position of the neutral axis on each face of the girder web, the bottom fiber stress at midspan, the girder end reactions, and the displacements and differential displacements at each diaphragm position.

For the first test girder, the position of the neutral axis was determined to be 832 mm from the extreme tension fiber on the east face of the girder and 833 mm on the west face. The position of the neutral axis is less than 2% higher than the value determined from the initial static test. This indicates that the large fatigue cracks present in the girder web at the end of the test had essentially no effect on the flexural stiffness of the built-up section. The girder end reactions were measured as 128.3 kN at the north end of the girder and 130.7 kN at the south end. Each of these values is also less than 2% larger than the corresponding values measured during the initial static test. The bottom fiber stress at mid-width of the flange was 49.2 MPa, an increase of 6.5% from the bottom fiber stress determined during the initial static test. The increases in the bottom fiber stresses and in the girder end reactions indicates that the cracks had the effect of decreasing the ability of the diaphragms to provide some support to the girder. The displacements measured at each diaphragm support this observation: see Table 6 – 15. Comparison between Table 6–4 and Table 6–15 show that the fatigue cracks had the effect of decreasing the

displacements at the spring-supported ends of the diaphragms while increasing the girder displacements a marginal amount. These effects resulted in significant increases in the differential displacements of the diaphragms where cracks formed. Since the stiffness of the diaphragm end supports was constant during the test, the decrease in the diaphragm end displacements indicates that the amount of load transferred through the diaphragms was less at the end of the test than at the start.

Similar conclusions about the change in girder behaviour at the end of testing can be drawn from the results of the final static tests performed on the second and third test specimens. For the second test specimen, the neutral axis position was 826 mm from the extreme tension fiber on the east face and 777 mm on the west face. The position of the neutral axis was virtually unchanged from the position determined from the initial static test (see Figure $6-5$), which suggests that the flexural stiffness of the girder did not change significantly, even though large fatigue cracks were present at the end of the test. The bottom fiber stress was 49.4 MPa, an 8.2% increase from the corresponding value determined from the initial static test. The north and south end reactions were 130.3 kN and 129.1 kN, respectively, which are marginally larger than the reactions measured during the initial static test. The increase in stresses and end reactions indicates that the cracks in the web did have an effect on magnitude of load transferred from the girder to the diaphragms. The displacement results shown in Figure 6–16 support this point since the displacements at several of the diaphragm ends at the end of the test were less than at the start of the test.

For the third test specimen, the neutral axis position was calculated from the final static test strain measurements to be 816 mm from the extreme tension fiber on the east face and 832 mm on the west face. The bottom fiber stress was also calculated from the strain data to be 47.7 MPa at the mid-width position of the flange. North and south end reactions of 133.3 kN and 134.1 kN were measured. Once again, the position of the neutral axis was virtually unchanged during the test, and the bottom fiber stress and girder end reactions were all marginally larger in magnitude than the corresponding values at the beginning of the test (see Section 6.1.2). This suggests that the flexural stiffness of the girder remained unchanged during fatigue testing and the magnitude of load transferred through the diaphragms decreased due to the presence of the cracks. Once again, the displacement results at the diaphragm positions outlined in Table 6–17 show that the load transferred through the diaphragms was reduced due to the presence of fatigue cracks at the diaphragm-to-girder connections.

6.2 Ancillary Test Results

Tension coupon tests were performed on material obtained from the web of two of the three test specimens, namely, girders 1 and 2. Two coupons were tested from each girder

and the results are reported in Table 6–18. Although the variation within each girder is very small, there is a significant difference in yield strength between the two girders. The steel grade specified on the as-built drawings is CSA G40.8 Grade B (CSA, 1960), which has a nominal yield strength of 260 MPa. Although Girder 1 shows a yield strength consistent with the specified grade of steel, Girder 2 seems to be of a higher grade steel.

Table 6-19 presents the results of the Charpy V-notch (CVN) impact tests conducted at temperatures varying from room temperature to –50° C. Both the energy absorbed (CVN value) and the percent shear fracture are reported in the table. Figure 6–19 shows the appearance of the fracture surface of all the test specimens from which the percent shear fracture was obtained. Again, the difference between the two girders is noticeable, both in terms of energy absorption and percentage of fracture surface consisting of shear failure. Girder 2 shows a lower CVN value at all three test temperatures. The minimum energy absorption requirement set by the American Railway Engineering Association is 34 J at various test temperatures down to –25° C. Since the coupons used for the tests were three-quarter size and the AREA requirement is set for full size coupons, the equivalent energy absorption requirement is 26 J, as specified by ASTM A370-97a. Table 6–19 indicates that both girders satisfied this requirement.

6.3 Examination of Fracture Surfaces

The fracture surface for each test specimen was examined with a low magnification stereomicroscope and a scanning electron microscope. The main objectives of these examinations were to determine the origin of the fatigue cracks, to assess whether there were any unusual features on the fracture surfaces, and to determine whether cracks had initiated from the repair holes or whether the crack tip had not been intercepted by the repair holes. In all the crack surfaces examined, the fatigue cracks had initiated at the edge of the drilled hole, as shown in Figure 6–20, where the dark area encloses the crack origin. In all the specimens examined there was no evidence to indicate that the crack tip might have been missed when the repair holes were drilled. All surfaces contained traces of corrosion products. As expected, there was more corrosion product build-up on the specimens that already had cracks at the start of the tests. In general, corrosion that had taken place in the field had obliterated the fatigue striation marks, but the corrosion that had taken place during the low temperature tests did not damage the striations significantly. A typical appearance of the fracture surface at high magnification is shown in Figure 6–21 where fatigue striations and traces of corrosion products can be seen.

TABLE 6–1

Results of Visual Inspection of Test Girder 1

Joint**	Distances to Stop Holes (mm) (see Figure 6–1)				Notes on Initial Cracks:
	L1	L2	L3	L4	
9	N/A*	N/A	N/A	N/A	No apparent cracking.
11	48	48	0	0	*East Face[†]:* crack extended across bottom of stiffener similar to cracks in Figure 6–2. *West Face:* crack extends laterally across holes similar to crack shown in Figure 6–3.
13	51	0	47	0	*East Face:* crack extended across bottom of stiffener similar to cracks in Figure 6–2. *West Face:* crack extends laterally across holes similar to crack shown in Figure 6–3.
15	N/A	N/A	N/A	N/A	No apparent cracking.
8	N/A	N/A	N/A	N/A	No apparent cracking.
10	45	45	5	5	*West Face:* crack extended across bottom of stiffener similar to cracks in Figure 6–2. *East Face:* no apparent cracking.
12	N/A	N/A	N/A	N/A	Small cracks in welds at bottom of transverse stiffener.
14	N/A	N/A	N/A	N/A	No apparent cracking.

* N/A indicates that no holes were drilled at the joint.
** Refer to Figure 5–2 for joint location.
[†] The east face of odd numbered joints is on the web surface on the diaphragm side and vice-versa for even numbered joints.

TABLE 6–2

Results of Visual Inspections of Test Girder 2

	Distances to Stop Holes (mm) (see Figure 6–1)				
Joint**	L1	L2	L3	L4	Notes on Initial Cracks:
9	N/A*	N/A	N/A	N/A	No apparent cracking.
11	40	46	0	0	*East Face[†]:* crack extended across bottom of stiffener similar to cracks in Figure 6–2. *West Face:* no apparent signs of cracking.
13	35	45	20	15	*East Face:* crack extended across bottom of stiffener similar to cracks in Figure 6–2. *West Face:* crack extends laterally across holes similar to crack shown in Figure 6–3.
15	N/A	N/A	N/A	N/A	No apparent cracking.
8	N/A	N/A	N/A	N/A	No apparent cracking.
10	N/A	N/A	N/A	N/A	No apparent cracking.
12	N/A	N/A	N/A	N/A	Small cracks in welds at bottom of transverse stiffener.
14	35	35	7	10	*West Face:* crack extended across bottom of stiffener similar to cracks in Figure 6–2. *East Face:* no apparent signs of cracking.

* N/A indicates that no holes were drilled at the joint.
** Refer to Figure 5–2 for joint location.
[†] The east face of odd numbered joints is on the web surface on the diaphragm side and vice-versa for even numbered joints.

TABLE 6–3

Results of Visual Inspections of Test Girder 3

	Distances to Stop Holes (mm) (see Figure 6–1)				
Joint**	L1	L2	L3	L4	Notes on Initial Cracks:
9	N/A*	N/A	N/A	N/A	No apparent cracking.
11	38	45	6	6	*East Face[†]:* crack extended across bottom of stiffener similar to cracks in Figure 6–2. *West Face:* no apparent signs of cracking.
13	52	54	0	0	*East Face:* crack extended across bottom of stiffener similar to cracks in Figure 6–2. *West Face:* crack extends laterally across holes similar to crack shown in Figure 6–3.
15	58	60	0	0	*West Face:* crack extended across bottom of stiffener similar to cracks in Figure 6–2. *East Face:* no apparent signs of cracking.
8	N/A	N/A	N/A	N/A	No apparent cracking.
10	N/A	N/A	N/A	N/A	Small cracks in welds at bottom of transverse stiffener.
12	50	47	0	0	*West Face:* crack extended across bottom of stiffener similar to cracks in Figure 6–2. *East Face:* no apparent signs of cracking.
14	N/A	N/A	N/A	N/A	No apparent cracking.

* N/A indicates that no holes were drilled at the joint.
** Refer to Figure 5–2 for joint location.
[†] The east face of odd numbered joints is on the web surface on the diaphragm side and vice-versa for even numbered joints.

Table 6–4

Diaphragm End Support Details – Test Girder 1

Joint*	Length of Diaphragm End Support (mm)	Vertical Displacement (mm)	Differential Displacements Designation	Displacement(mm)
3	770	-3.0508		
			$\Delta_{3\text{-}9}$	0.1234
9		-2.9274		
4	730	-3.7401		
			$\Delta_{4\text{-}11}$	-0.2847
11		-4.0248		
5	715	-3.1247		
			$\Delta_{5\text{-}13}$	-0.3844
13		-3.5091		
6	520	-1.1640		
			$\Delta_{6\text{-}15}$	-0.1534
15		-1.3174		
8		-1.1053		
			$\Delta_{8\text{-}17}$	-0.3708
17	490	-0.7345		
10		-3.3775		
			$\Delta_{10\text{-}18}$	-0.3358
18	710	-3.0417		
12		-3.9945		
			$\Delta_{12\text{-}19}$	-0.1853
19	760	-3.8092		
14		-2.9848		
			$\Delta_{14\text{-}20}$	0.0907
20	790	-3.0755		

* Refer to Figure 5–2 for joint location.

TABLE 6–5

Diaphragm End Reactions at Maximum Static Load, Test 1

Joint	Span Length (mm)	Diaphragm End Deflection (mm)	Support Reaction Force (kN)
3	770	3.051	5.13
4	730	3.740	7.38
5	715	3.125	6.57
6	520	1.164	6.36
17	490	0.734	4.79
18	710	3.042	6.53
19	760	3.809	6.66
20	790	3.076	4.79
		Total Load (kN):	48.2

TABLE 6–6

Web Gap Stresses on the East and West Face of Joint 12 – Test Girder 1

Gauge**	Stress (MPa)	Major Principal Stress (MPa)	Minor Principal Stress (MPa)	Angle to Major Principal Axis[†] (degrees)
13	46.6			
14	25.3	60.4	0.43	28.75
15	14.3			
16	52.9			
17	N/R*	—	—	—
18	41.7			
19	57.6			
20	17.2	66.2	23.2	26.61
21	31.8			
22	48.0			
23	24.7	62.7	6.31	30.67
24	21.0			
25	31.7			
26	2.6	31.8	-42.8	2.02
27	-42.8			
28	28.9			
29	-15.7	32.2	-46.6	-11.76
30	-43.3			

* N/R denotes gauge not responding.

[†] Angle from horizontal (counterclockwise rotation positive).

** See Figure 5–10 for the location of the rosettes.

Table 6–7

Diaphragm End Support Details – Test Girder 2

Joint*	Length of Diaphragm End Support (mm)	Vertical Displacement (mm)	Differential Displacements Designation	Differential Displacements Displacement (mm)
3	780	-2.9937		
			Δ_{3-9}	0.0377
9		-2.9560		
4	740	-3.7429		
			Δ_{4-11}	-0.3431
11		-4.0860		
5	710	-3.1450		
			Δ_{5-13}	-0.4401
13		-3.5851		
6	500	-1.1428		
			Δ_{6-15}	-0.1534
15		-1.2962		
8		-1.3078		
			Δ_{8-17}	-0.1982
17	490	-1.1096		
10		-3.5089		
			Δ_{10-18}	-0.3913
18	700	-3.1176		
12		-4.1628		
			Δ_{12-19}	-0.2216
19	750	-3.9412		
14		-2.9668		
			Δ_{14-20}	0.1056
20	790	-3.0724		

* Refer to Figure 5–2 for joint location.

Table 6–8

Diaphragm End Reactions at Maximum Static Load, Test 2

Joint	Span Length (mm)	Diaphragm End Deflection (mm)	Support Reaction Force (kN)
3	780	2.994	4.84
4	740	3.743	7.09
5	710	3.145	6.75
6	500	1.143	7.02
17	490	1.109	7.24
18	700	3.118	6.98
19	750	3.941	7.17
20	790	3.072	4.79
		Total Load (kN):	51.9

TABLE 6–9

Web Gap Stresses on the East and West Face of Joint 12 – Test Girder 2

Gauge	Stress (MPa)	Major Principal Stress (MPa)	Minor Principal Stress (MPa)	Angle to Major Principal Axis[†] (degrees)
13	32.6			
14	14.7	40.8	6.3	29.24
15	14.5			
16	40.7			
17	10.4	46.1	20.9	27.73
18	26.4			
19	29.4			
20	15.2	39.3	6.2	33.14
21	16.1			
22	N/R*			
23	15.4	—	—	—
24	N/R			
25	26.2			
26	-0.7	26.2	-38.4	-0.62
27	-38.4			
28	35.5			
29	-10.3	37.0	-39.3	-7.83
30	-37.9			

* N/R denotes gauge not responding.

[†] Angle from horizontal (counterclockwise rotation positive).

** See Figure 5–10 for the location of the rosettes.

TABLE 6–10

Diaphragm End Support Details – Test Girder 3

Joint*	Length of Diaphragm End Support (mm)	Vertical Displacement (mm)	Differential Displacements	
			Designation	Displacement (mm)
3	820	-2.9001		
			$\Delta_{3\text{-}9}$	-0.0601
9		-2.9602		
4	740	-3.9291		
			$\Delta_{4\text{-}11}$	-0.3415
11		-4.2706		
5	730	-3.3556		
			$\Delta_{5\text{-}13}$	-0.3962
13		-3.7518		
6	500	-1.2633		
			$\Delta_{6\text{-}15}$	-0.2068
15		-1.4701		
8		-1.2169		
			$\Delta_{8\text{-}17}$	-0.1169
17	500	-1.1000		
10		-3.5191		
			$\Delta_{10\text{-}18}$	-0.4059
18	720	-3.1132		
12		-4.2193		
			$\Delta_{12\text{-}19}$	-0.2889
19	740	-3.9304		
14		-3.1434		
			$\Delta_{14\text{-}20}$	0.0490
20	830	-3.1924		

* Refer to Figure 5–2 for joint location.

Table 6–11

Diaphragm End Reactions at Maximum Static Load, Test 3

Joint	Span Length (mm)	Diaphragm End Deflection (mm)	Support Reaction Force (kN)
3	820	2.900	4.04
4	740	3.929	7.45
5	730	3.356	6.62
6	520	1.217	6.65
17	520	1.100	6.01
18	720	3.113	6.41
19	740	3.930	7.45
20	830	3.192	4.29
		Total Load (kN):	48.9

Table 6–12

Conditions During Low Temperature Tests Performed on Test Girder 1

Low Temp. Test	Joint	Cycle (×10⁶)	Crack Length (mm)	Actuator Load (kN)		Midspan Bottom Fiber Stress (MPa)	Temperature Readings (°C)[†]				
				North	South		Gauge 1	Gauge 2	Gauge 3	Gauge 4	Gauge 5
1	11	1.27	32	101	101	33	-50	-43	-39	-50	-47
2	11	2.29	55	101	101	33	-50	-40	-44	-47	-44
3	11	3.28	75	101	101	33	-50	-47	-35	-50	-47
4	13	3.28	50	101	101	33	-46	-46	-40	-38	—
5	11	3.93	138	101	101	33	-50	-50	-50	-50	-47
6	11	4.22	170	175	175	60	-50	-42	-46	-50	-45
7	11	4.22	170	335	0	60	-50	-42	-46	-50	-45
8	13	4.22	152	175	175	60	-50	-43	-50	-40	—
9	13	4.22	152	0	335	60	-50	-43	-47	-35	—

[†] See Figure 5–13 for orientation of thermistors in insulated chamber.

115

Table 6–13

Conditions During Low Temperature Static Tests Performed on Test Girder 2

Low Temp. Test	Joint	Cycle (×10^6)	Crack Length (mm)	Actuator Load (kN) North	South	Midspan Bottom Fiber Stress (MPa)	Temperature Readings (°C)† Gauge 1	Gauge 2	Gauge 3	Gauge 4	Gauge 5
1	13	4.39	158	101	101	33	-50	-50	-47	-43	—
2	13	4.7	195	175	175	60	-50	-50	-48	-48	—
3	13	4.7	195	0	335	60	-50	-50	-48	-48	—
4	11	4.7	130	175	175	60	-50	-45	-20	-34	-44
5	11	4.7	130	342	0	60	-50	-46	-23	-50	-43

† See Figure 5–13 for orientation of thermistors in insulated chamber.

Table 6–14

Conditions During Low Temperature Static Tests Performed on Test Girder 3

Low Temp. Test	Joint	Cycle (×10^6)	Crack Length (mm)	Actuator Load (kN) North	South	Midspan Bottom Fiber Stress (MPa)	Temperature Readings (°C)† Gauge 1	Gauge 2	Gauge 3	Gauge 4	Gauge 5
1	13	3.71	247	175	175	60	-50	-48	-45	-40	-45
2	13	3.71	247	0	370	63	-50	-50	-44	-36	-42

† See Figure 5–13 for orientation of thermistors in insulated chamber.

Table 6–15

Diaphragm End Support Details at End of Test – Test Girder 1

Joint*	Length of Diaphragm End Supports (mm)	Vertical Displacement (mm)	Differential Displacements	
			Designation	Displacement (mm)
3	770	-3.1050		
			$\Delta_{3\text{-}9}$	0.1123
9		-2.9927		
4	730	-3.1006		
			$\Delta_{4\text{-}11}$	-0.9936
11		-4.0942		
5	715	-3.2307		
			$\Delta_{5\text{-}13}$	-0.4360
13		-3.6667		
6	520	-1.1349		
			$\Delta_{6\text{-}15}$	-0.1160
15		-1.2509		
8		-1.1567		
			$\Delta_{8\text{-}17}$	-0.1325
17	490	-1.0242		
10		-3.3875		
			$\Delta_{10\text{-}18}$	-0.3977
18	710	-2.9898		
12		-4.0156		
			$\Delta_{12\text{-}19}$	-0.4624
19	760	-3.5532		
14		-3.0112		
			$\Delta_{14\text{-}20}$	0.0708
20	790	-3.0820		

* Refer to Figure 5–2 for joint location.

Table 6–16

Diaphragm End Support Details at End of Test – Test Girder 2

Joint*	Length of Diaphragm End Support (mm)	Vertical Displacement (mm)	Differential Displacements	
			Designation	Displacement (mm)
3	780	-2.9000		
			$\Delta_{3\text{-}9}$	-0.0600
9		-2.9600		
4	740	-3.5959		
			$\Delta_{4\text{-}11}$	-0.5462
11		-4.1421		
5	710	-2.8614		
			$\Delta_{5\text{-}13}$	-0.8090
13		-3.6704		
6	500	-1.2769		
			$\Delta_{6\text{-}15}$	-0.0118
15		-1.2887		
8		-1.1997		
			$\Delta_{8\text{-}17}$	0.0147
17	490	-1.2144		
10		-3.6493		
			$\Delta_{10\text{-}18}$	-0.4904
18	700	-3.1589		
12		-4.2481		
			$\Delta_{12\text{-}19}$	-0.3803
19	750	-3.8678		
14		-3.0599		
			$\Delta_{14\text{-}20}$	-0.0139
20	790	-3.0460		

* Refer to Figure 5–2 for joint location.

Table 6–17

Diaphragm End Support Details at End of Test – Test Girder 3

Joint*	Length of Diaphragm End Support (mm)	Vertical Displacement (mm)	Differential Displacements	
			Designation	Displacement (mm)
3	820	-3.0740		
			$\Delta_{3\text{-}9}$	-0.0284
9		-3.1024		
4	740	-4.0891		
			$\Delta_{4\text{-}11}$	-0.2131
11		-4.3022		
5	730	-2.8200		
			$\Delta_{5\text{-}13}$	-0.9000
13		-3.7200		
6	500	-1.2009		
			$\Delta_{6\text{-}15}$	-0.1586
15		-1.3595		
8		-1.3900		
			$\Delta_{8\text{-}17}$	-0.1600
17	500	-1.2300		
10		-3.6124		
			$\Delta_{10\text{-}18}$	-0.4959
18	720	-3.1165		
12		-4.3900		
			$\Delta_{12\text{-}19}$	-0.3200
19	740	-4.0700		
14		-3.2138		
			$\Delta_{14\text{-}20}$	0.0364
20	830	-3.2502		

* Refer to Figure 5–2 for joint location.

Table 6–18

Tension Coupon Test Results

Specimen	Coupon	Modulus of Elasticity (MPa)	Static Yield Strength (MPa)	Static Ultimate Strength (MPa)
Girder 1	1	196 000	288	450
	2	198 000	288	454
Girder 2	1	199 000	345	475
	2	203 000	338	469

Table 6–19

Charpy V-Notch Impact Test Results

Specimen	Test Temperature	Girder 1 CVN value (J) (% shear fracture)	Girder 2 CVN value (J) (% shear fracture)
1	+20° C	89 (95-100%)	81 (85-90%)
2	+20° C	91 (95-100%)	81 (85-90%)
3	-25° C	88 (90-95%)	57 (55-60%)
4	-25° C	91 (90-95%)	56 (55-60%)
5	-50° C	62 (65-75%)	24 (20-25%)
6	-50° C	73 (65-75%)	26 (20-25%)
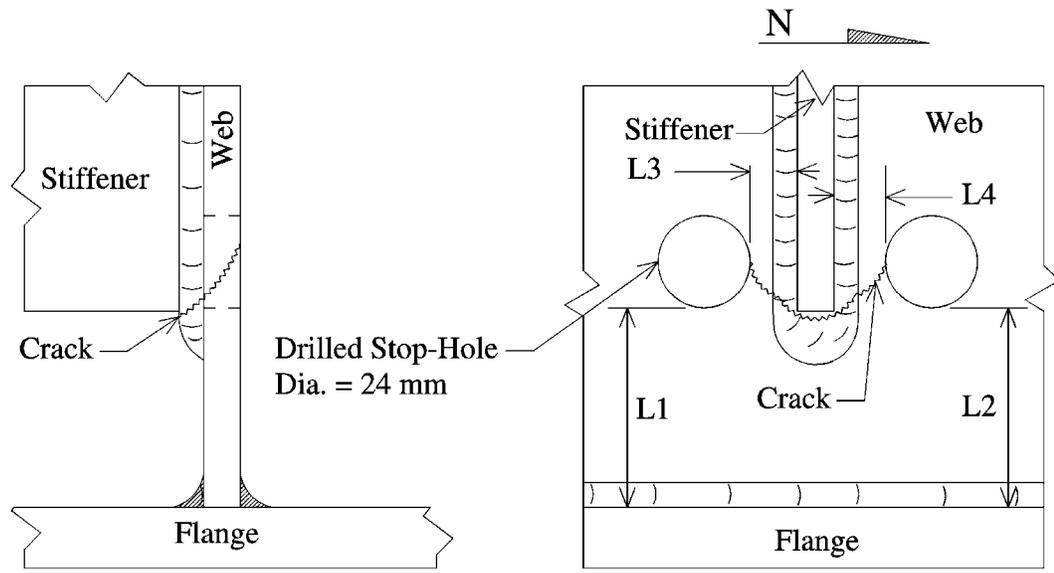
Figure 6–1 Typical Orientation of Stop Holes and Cracks in Test Girder Sections
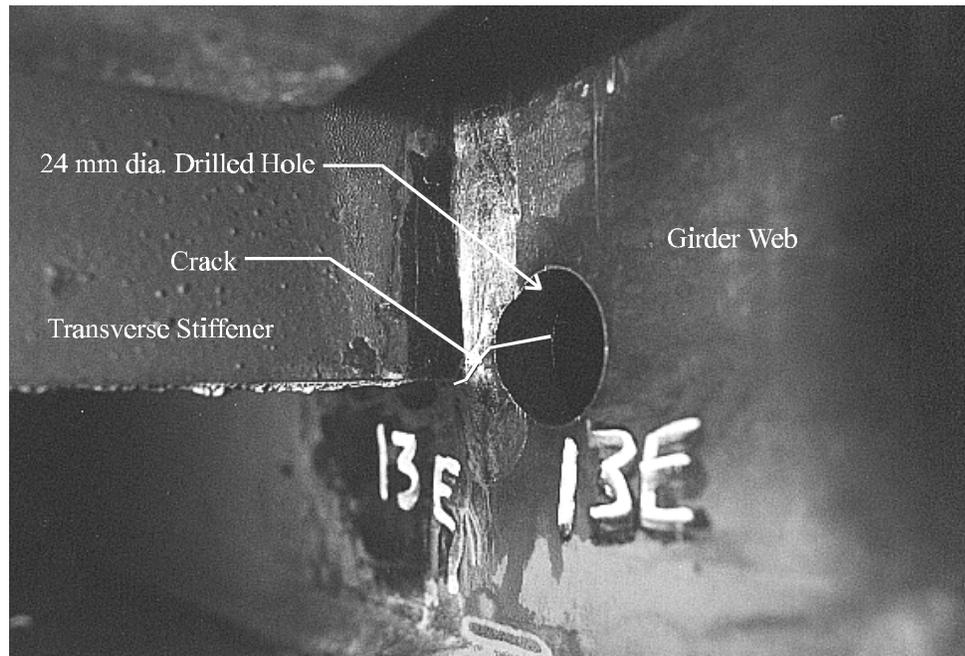
Figure 6–2 Initial Cracks and Stop Holes on East Face of Joint 13, Test Girder 1
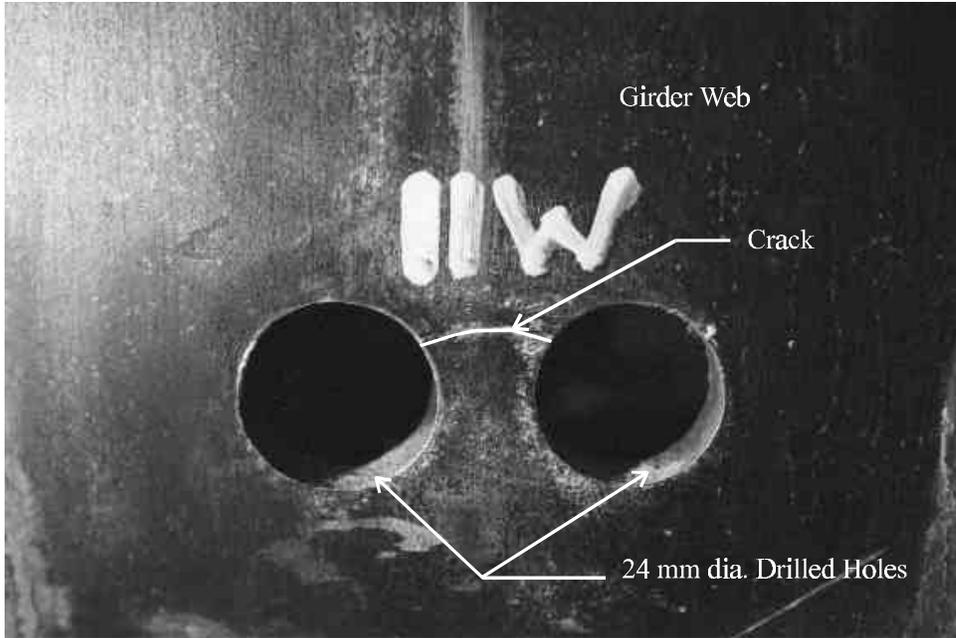
Figure 6–3 Initial Cracks and Stop Holes on West Face of Joint 11, Test Girder 1
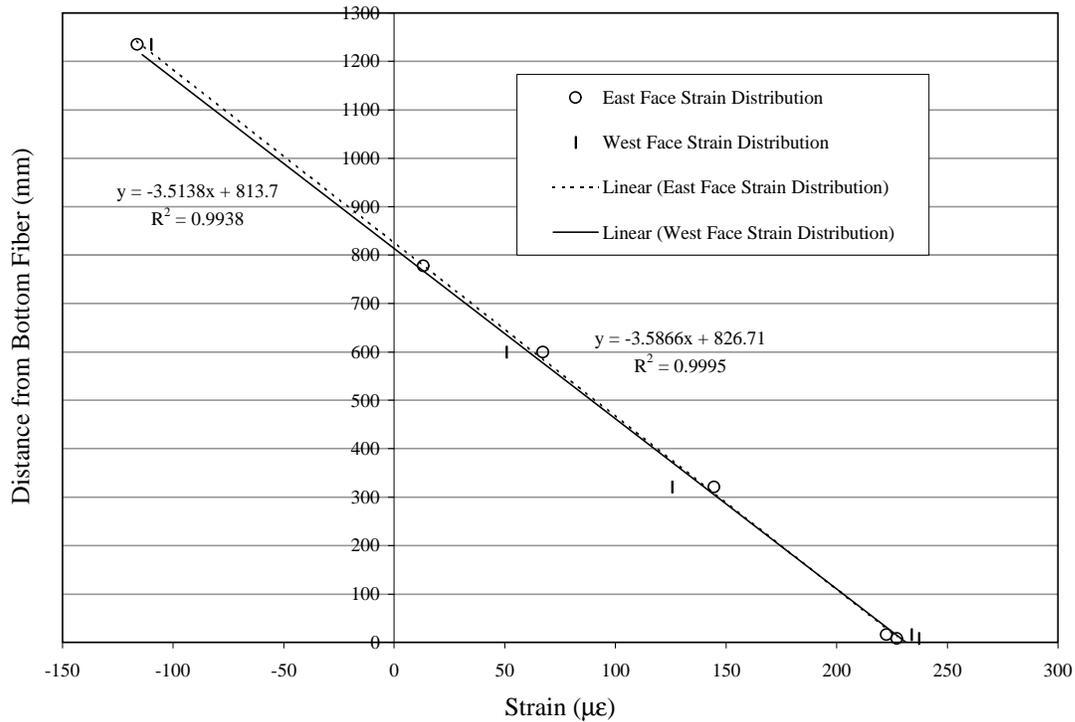
Figure 6–4 Strain Distributions at Midspan of Test Specimen 1 (P_{static}=150 kN/actuator)
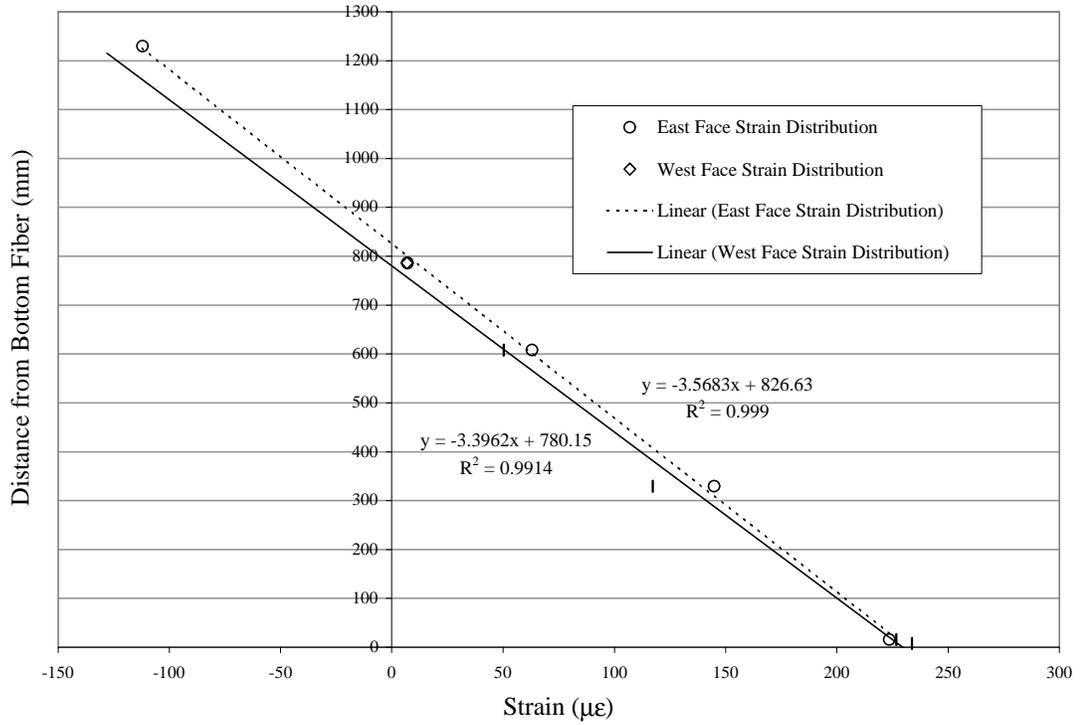
**Figure 6–5** Strain Distributions at Midspan of Test Specimen 2 (P_{static}=152 kN/actuator)
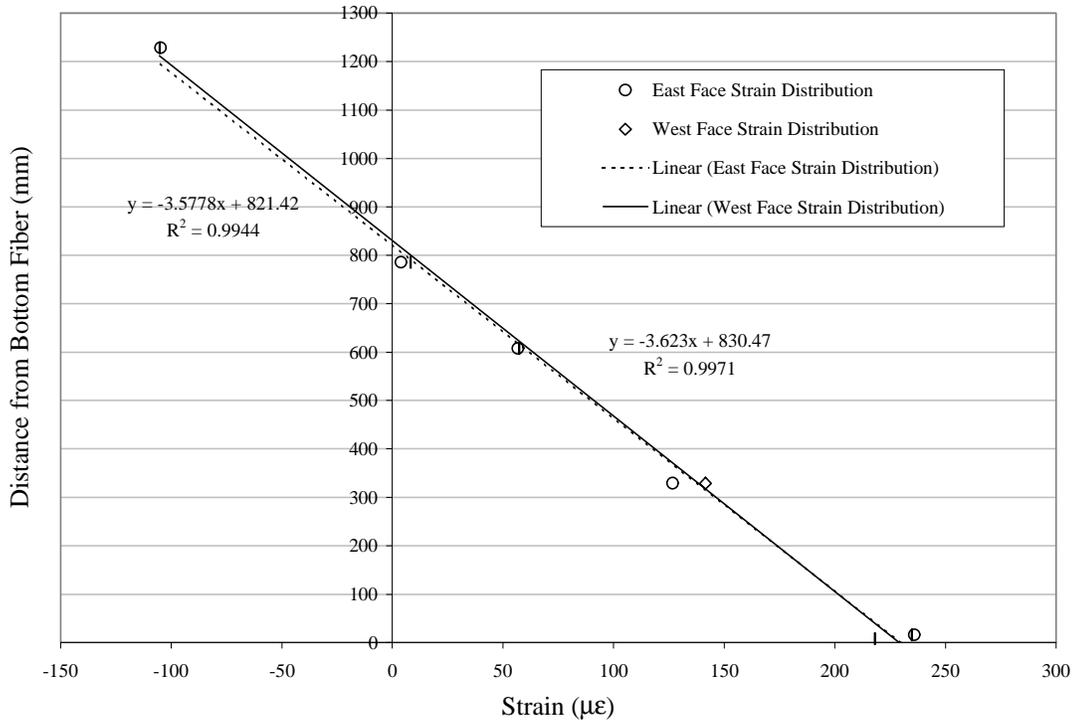
Figure 6–6 Strain Distributions at Midspan of Test Specimen 3 (P_{static}=150 kN/actuator)
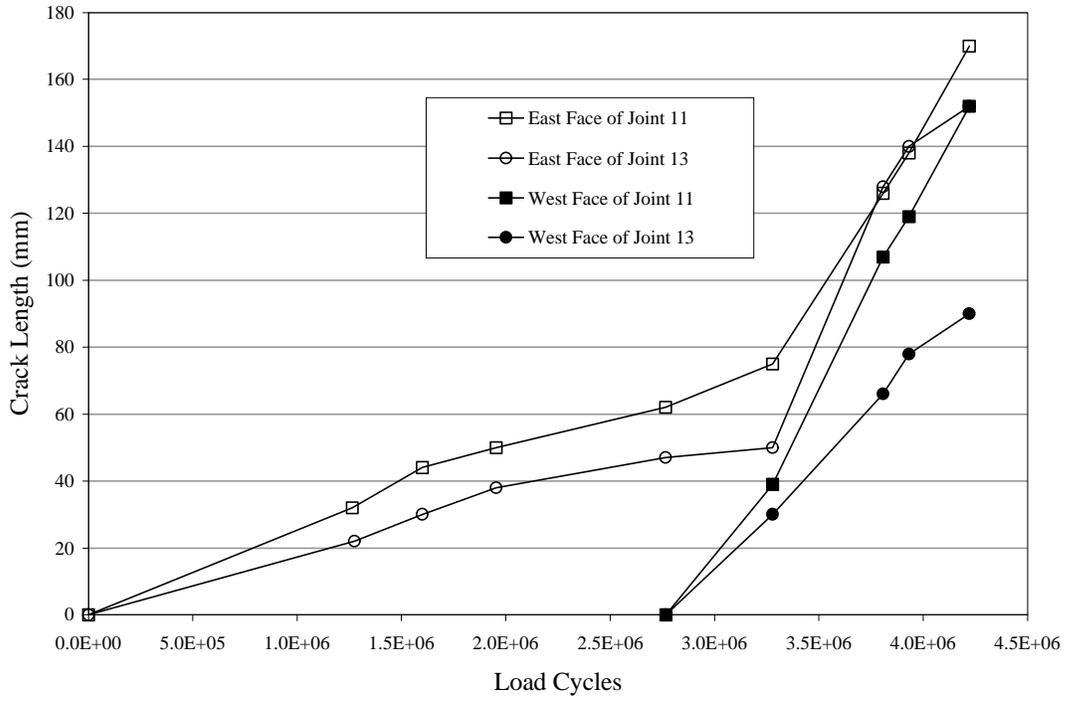
Figure 6–7 Crack Lengths vs. Load Cycles, Test 1
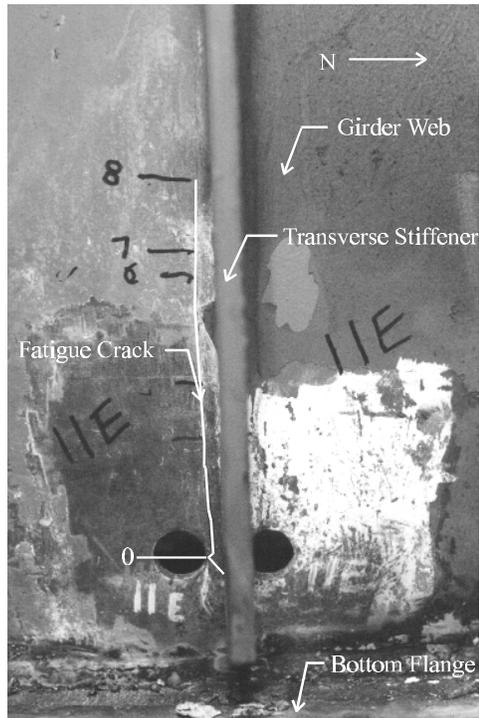
Figure 6–8 Fatigue Crack in Web on East Face of Joint 11, Test 1
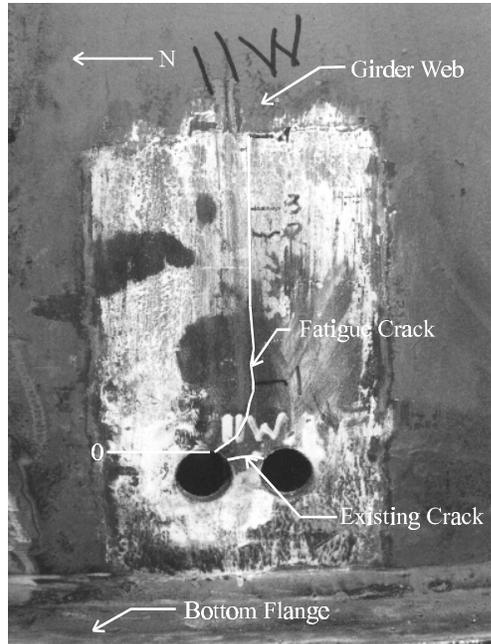
**Figure 6–9** Fatigue Crack in Web on West Face of Joint 11, Test 1
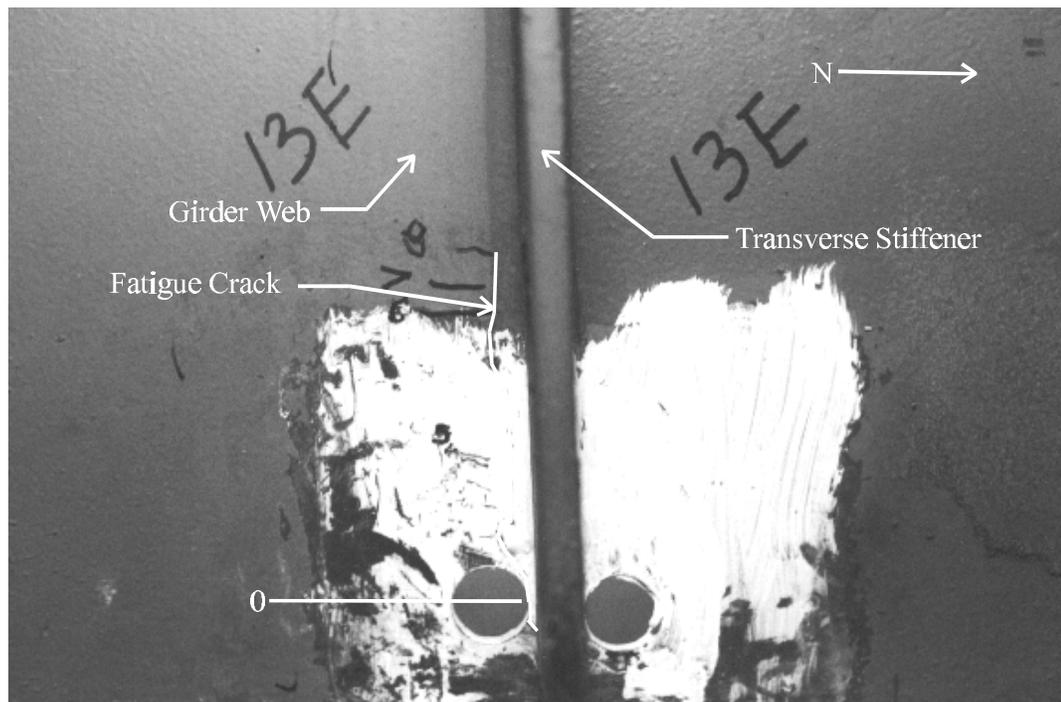
Figure 6–10 Fatigue Crack in Web on East Face of Joint 13, Test 1
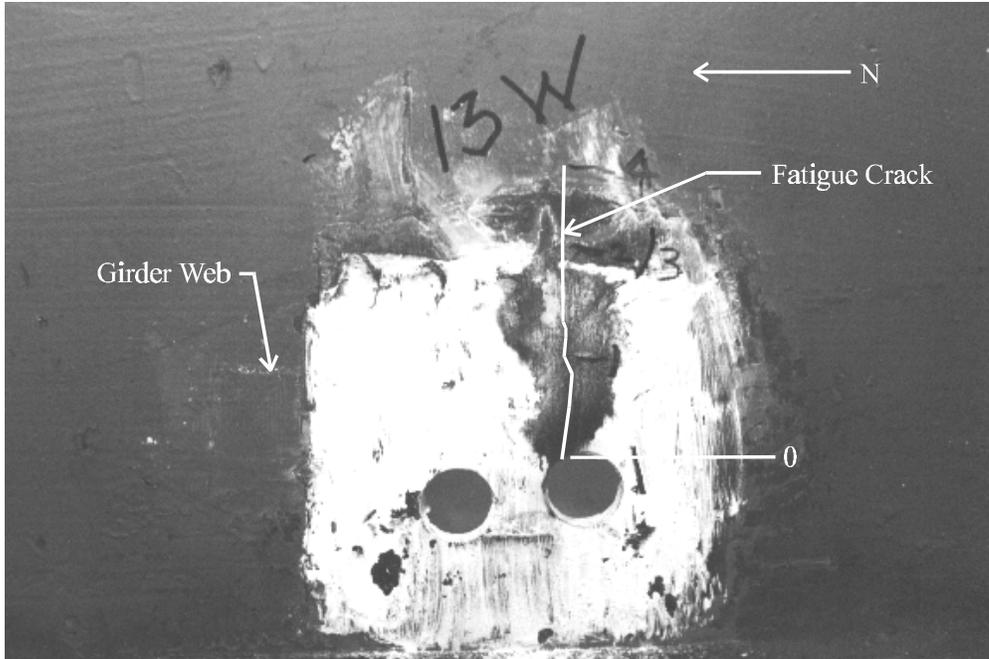
Figure 6–11 Fatigue Crack in Web on West Face of Joint 13, Test 1
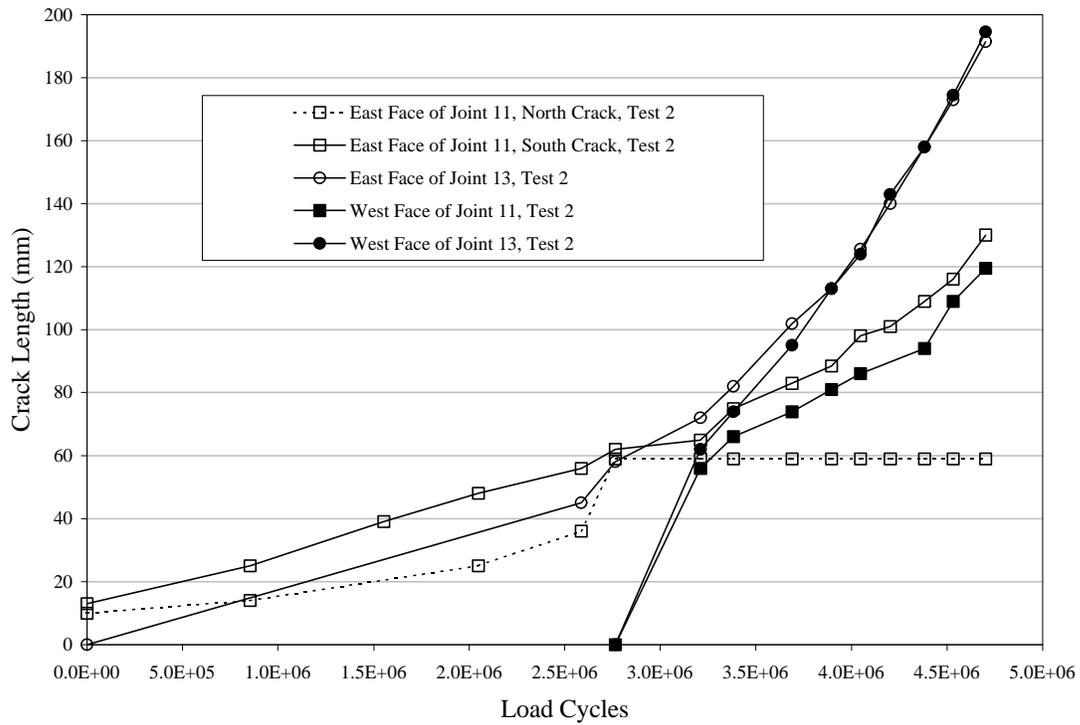

Figure 6–12 Crack Lengths vs. Load Cycles, Test 2
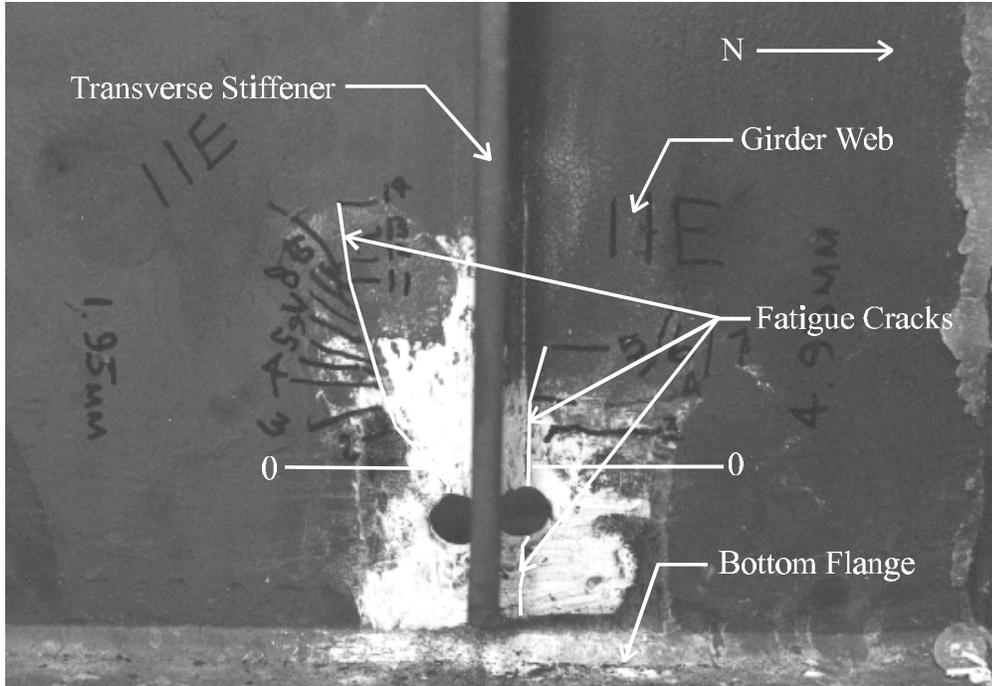
**Figure 6–13** Fatigue Cracks in Web on East Face of Joint 11, Test 2
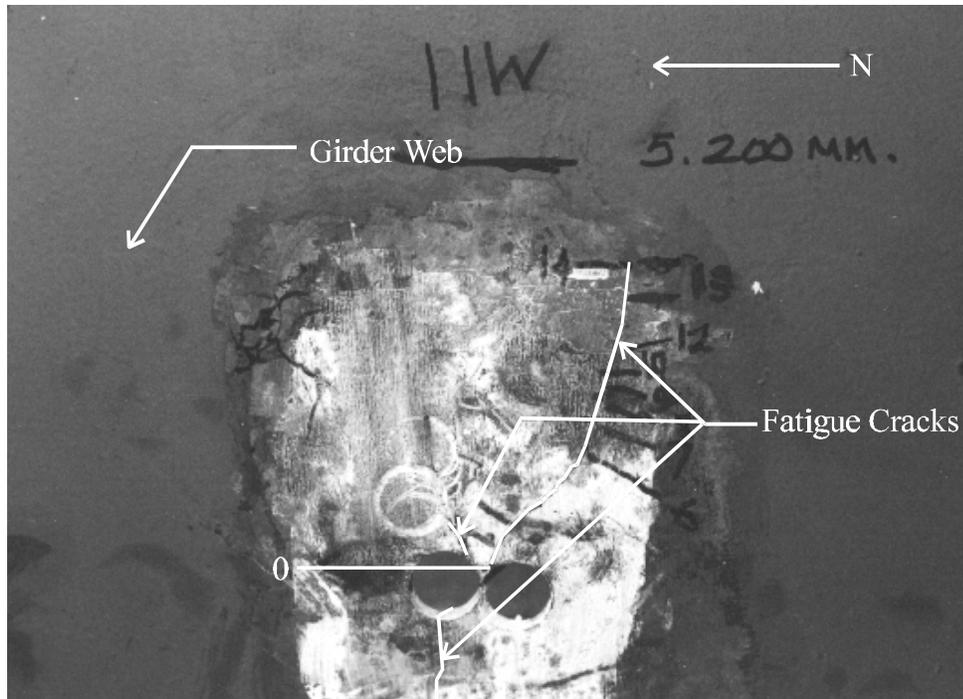
**Figure 6–14** Fatigue Cracks in Web on West Face of Joint 11, Test 2
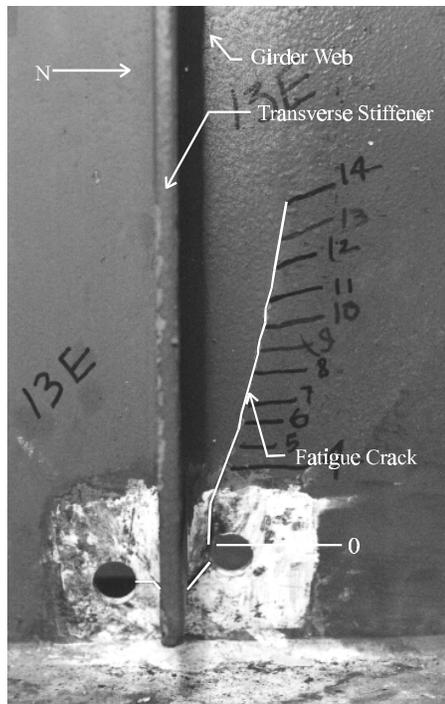
**Figure 6–15** Fatigue Crack in Web on East Face of Joint 13, Test 2
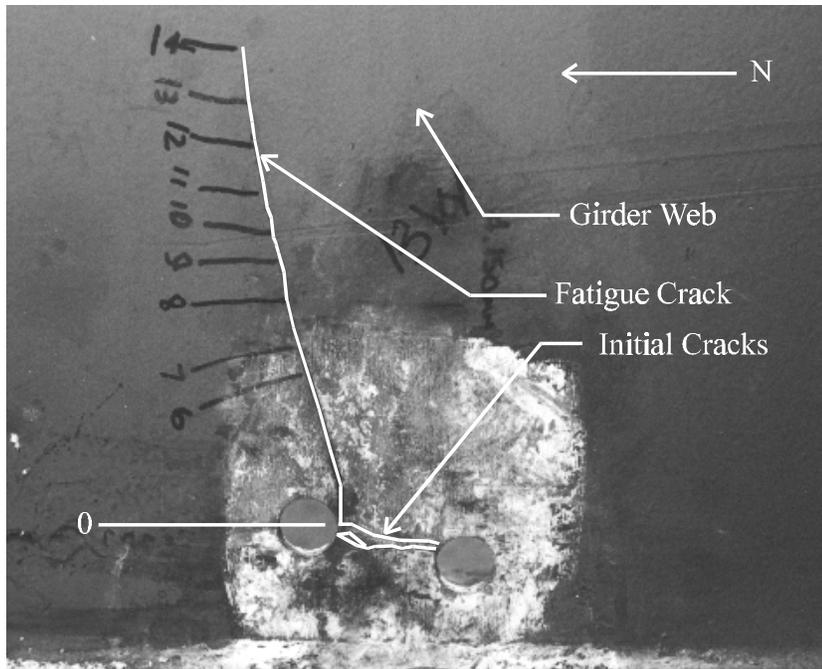
**Figure 6–16** Fatigue Crack in Web on West Face of Joint 13, Test 2
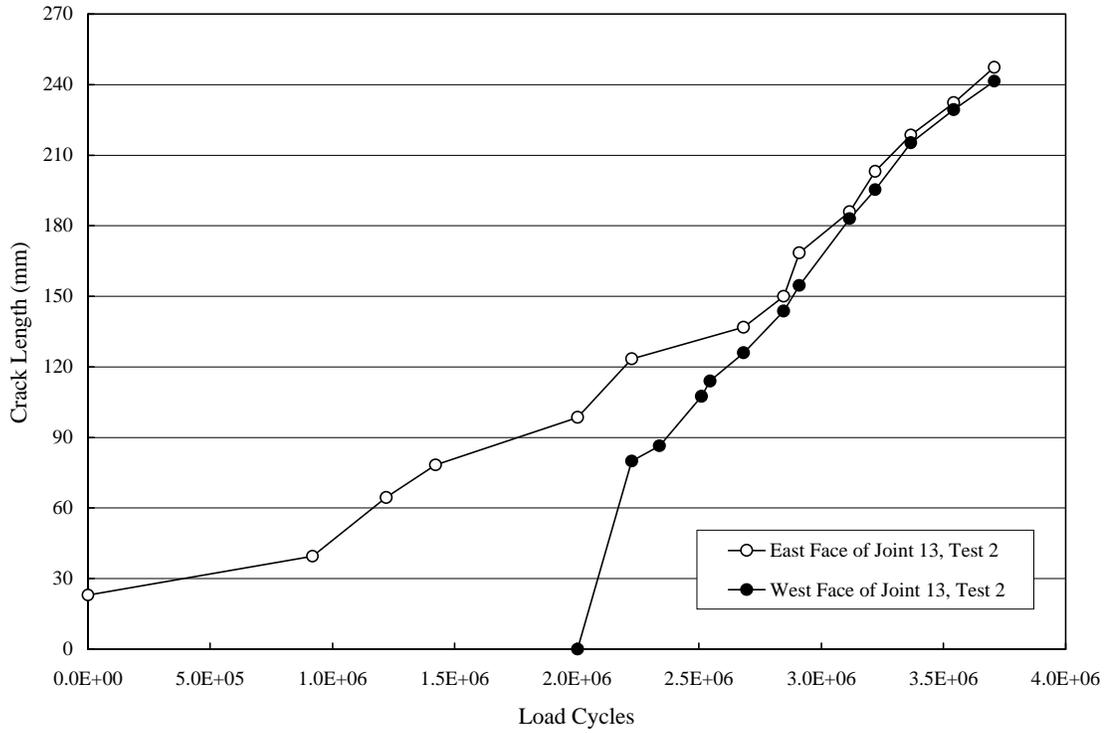
**Figure 6–17** Crack Lengths vs. Load Cycles, Test 3
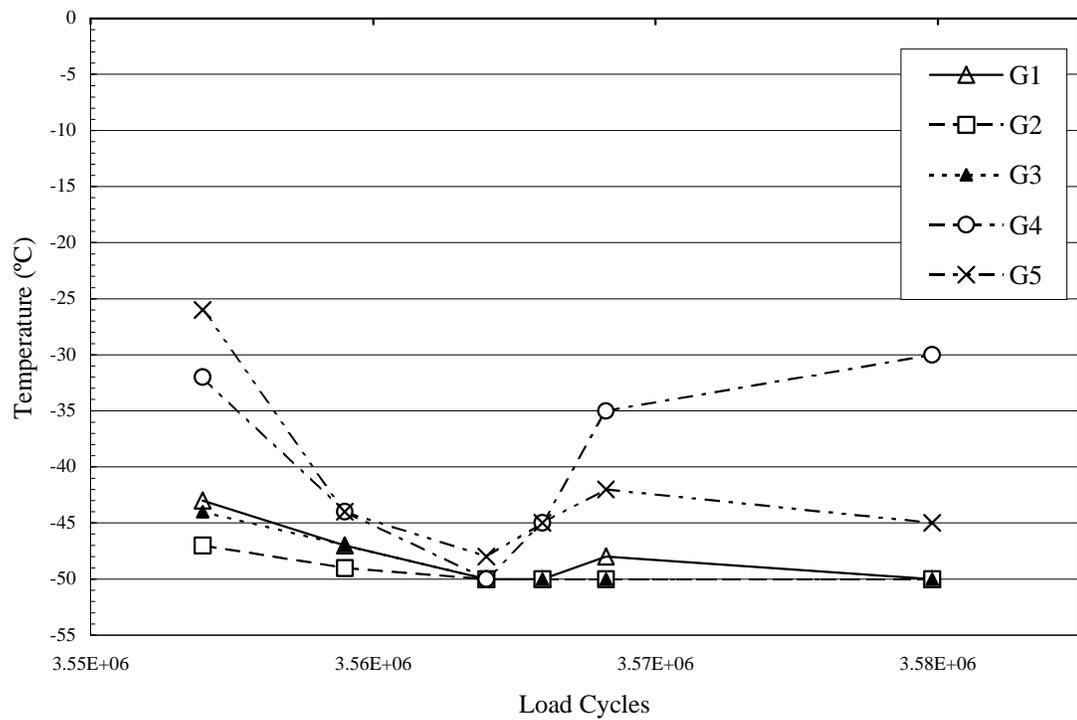
Figure 6–18 Temperature Profile at Joint 13 During Dynamic Low Temperature Test, Test 3
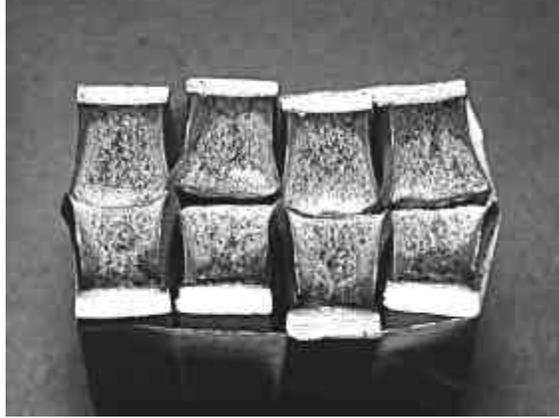
(a) +20° C

(b) –25° C
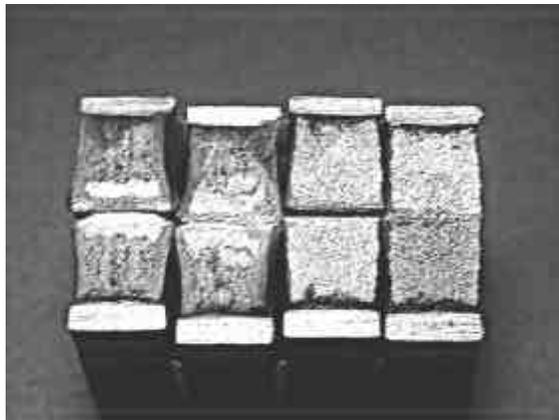
(c) –50° C

**Figure 6–19** Fracture Surface Appearance of Charpy Specimens
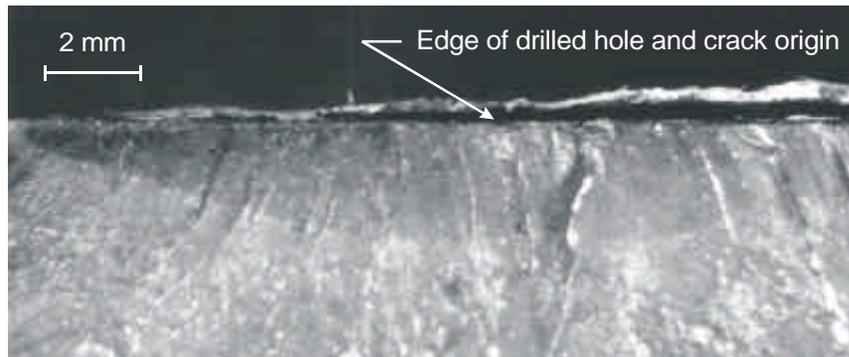
Figure 6-20 Origin of Fatigue Crack at Surface of Drilled Hole
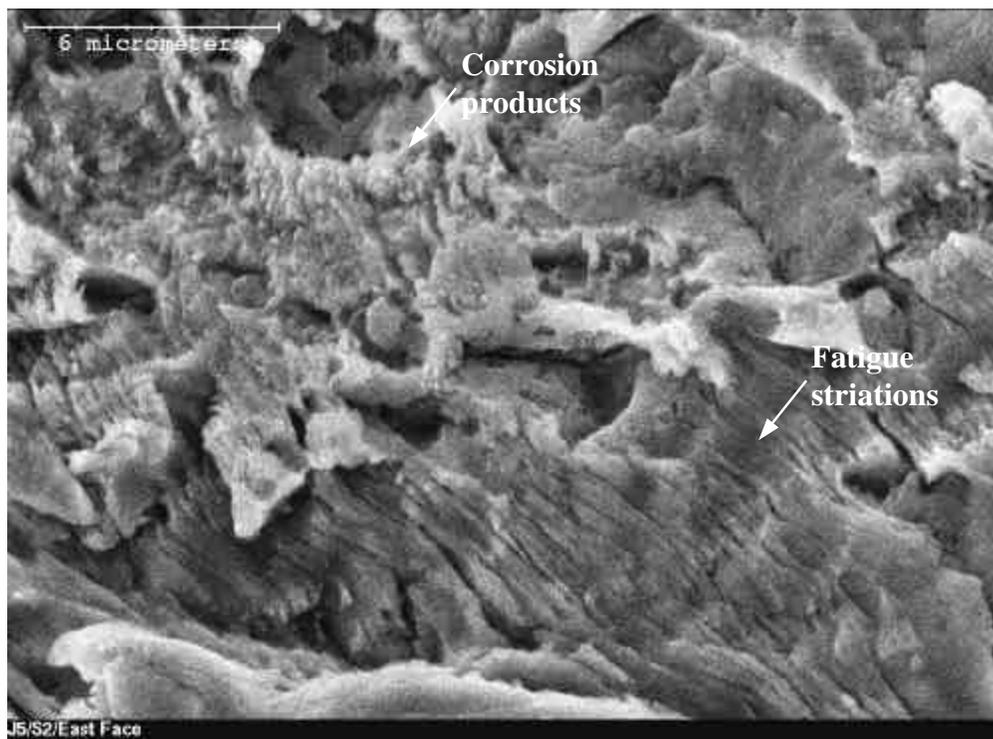

Figure 6-21 Fatigue Striations and Corrosion Products on Fracture Surface of Specimen 2

131

CHAPTER 7

SUMMARY, CONCLUSIONS AND RECOMMENDATIONS

7.1 Summary

Many multigirder bridges are experiencing distortion-induced fatigue cracking at the diaphragm-to-girder connections. One of these bridges is the St. Albert Trail Mile 5.09 Subdivision bridge in Edmonton Alberta. This bridge was placed in service in 1965 and is comprised of two parallel bridges, one for the eastbound traffic and one for the westbound traffic. Each bridge has eight parallel steel girders interconnected by steel diaphragms and a composite concrete deck. The four span bridge (two end spans of 9.9 m and two middle spans of 17.3 m) is built on a 28° RHF skew and the diaphragms are staggered across the girder spans. The channel-type diaphragm members are connected to each girder through transverse stiffeners that are welded to the girder web and top flange, but cut 50 mm short of the bottom tension flange. Because the diaphragm is not continuous across the width of the bridge, the out-of-plane distortion in the web gap increased due to the out-of-plane flexibility of the web. By 1998 over 300 distortion-induced fatigue cracks had been discovered in the girder webs near the web-to-stiffener junction.

In August 1998 the owner of the bridge decided to replace the bridge with a new structure. Before the bridge was dismantled, the writer carried out field testing in order to measure the strains and displacements in one set of the 9.9 m spans. Static and dynamic tests were conducted using two CN Rail EF-644a locomotives running on the main line (north rails). After field testing was completed, University of Alberta researchers obtained twelve girders from the 9.9 m spans in the North Bridge for laboratory testing.

The field test results were used to design the experimental test setup so that the behaviour of the distortion-induced fatigue cracks could be studied during the remaining life of the girders under conditions similar to those that existed in the field. The in-situ midspan-bottom fiber stress range in the most heavily loaded girder and the in-situ racking motion at each of the diaphragms surrounding the same girder were re-created in the

experimental testing program. The program consisted of fatigue testing three of the girders to assess the behaviour of the fatigue cracks in the web gap regions. Low temperature tests were also carried out, at -50ºC, in order to determine whether the fatigue cracks would remain stable throughout the remaining useful life of the girders. The first test was stopped at 4.23 million cycles, at which time the fatigue crack lengths were 170 mm and 152 mm. At 4.71 million cycles, the second test was ended and the critical fatigue crack lengths were measured to be 130 mm and 195 mm. Lastly, the third test was stopped at 3.71 million cycles, when the maximum crack length at a web gap location was 247 mm. Even at the end of fatigue testing, the fatigue cracks in each of the three tests remained stable during the low temperature tests.

7.2 Conclusions

This report summarizes the results obtained from the field tests performed on the St. Albert Trail Mile 5.09 Subdivision bridge and the full-scale fatigue and low temperature tests performed on three of the bridge girders that were taken out of service. From the field testing program, the following observations can be made:

1. A comparison between strain gauge data obtained under static and dynamic loading conditions indicated that the dynamic load factor was as low as 1.02 .

2. The static and dynamic live load distribution analyses showed that the percentage of total load resisted by each girder is 16.5% for Girder 1, 24.4% for Girder 2, 30.8% for Girder 3, and 28.3% for Girder 4.

3. The maximum midspan bottom fiber stress range as a result of one of the heaviest repeatable loads on the structure in the instrumented span was 35 MPa.

From the laboratory experimental program, the following observations regarding the behaviour of the girders and the distortion-induced fatigue cracks in the girder webs can be made:

1. The remaining fatigue life of the bridge girders (after they were taken out of service) is 4.22 million cycles at a midspan-bottom fiber stress range of 35 MPa and

diaphragm racking motions as large as 0.44 mm. These conditions are representative of the maximum response of the bridge span under CN Rail EF-644a locomotive loads.

2. The presence of the large fatigue cracks in the girder web did not significantly affect the ability of the girders to resist and transfer even the most extreme service loads.

3. Staggered diaphragms are not very effective at transferring gravity loads laterally and the large fatigue cracks in the girder webs further reduced the ability of the diaphragms to transfer these loads.

4. Static and cyclic tests conducted on girders with large fatigue cracks in the web indicated that, even at a temperature of -50°C, the girders exhibited sufficient fracture toughness to prevent unstable crack propagation even under service stresses two times those measured in the field under CN Rail EF-644a locomotive loads.

5. It seems that rehabilitation of steel girders with distortion-induced fatigue cracks by the use of drilled holes at crack tips merely retards crack growth in situations where distortion-induced stresses initiate and propagate the cracks.

6. The distortions and stresses measured in the web gaps show that the gaps are in double curvature: the top of the gap is pulled towards the end of the diaphragm and the bottom of the web gap is restrained by the relatively stiff bottom flange. The major principal stresses in the web gap were measured to be as large as 66 MPa at Joint 12 where the racking motion was approximately 0.19 mm. This suggests that much larger gap stresses would be present at the diaphragms where the racking motion is as large as 0.44 mm (i.e., Joint 13), at least before significant cracking and rehabilitation holes are present in these web gaps.

7.3 Recommendations for Further Research

Several recommendations for the research that is to be carried out on the remaining nine girders can be made so that more knowledge about the behaviour of distortion-induced fatigue cracks can be acquired. These recommendations are:

1. A comprehensive finite element model of the web gap region should be created and calibrated to the localised distortions and strains measured in the web gap region during testing. The calibrated numerical model can then be used to correlate the web gap stresses with the differential displacements at diaphragm positions and the in-plane bottom fiber stresses at midspan.

2. Further investigation of the tearing deformation of distortion- induced fatigue cracks should be carried out. This is an important phenomenon that may limit the effectiveness of hole drilling to arrest fatigue cracks.

3. Test the remaining nine girders taken out-of-service in sets of two or three at different stress ranges to determine the fatigue categories of the critical web gap details.

4. Assess possible rehabilitation schemes to determine the most effective manner to repair girders that have been damaged in this manner. Possible rehabilitation schemes include:

   - Attach the transverse stiffeners to the girder tension flange (as recommended in Clause 6.6.1.3 of the 1998 AASHTO LRFD Bridge Design Specifications) using a bolted angle section;

   - Cut back the transverse stiffeners at diaphragm positions in order to increase the flexibility, and, subsequently, to reduce the stresses in the web gap region to a level where fatigue cracks will not initiate. The effectiveness of this rehabilitation scheme at pre-cracked web gap locations is problematic since some driving force at the crack front still exists. Therefore, it should only be carried out at uncracked locations;

   - Drill holes at the tips of fatigue cracks and cold-work the holes to create high residual compressive stresses around the crack tip;

   - Grind out small cracks that are restricted to the web-to-stiffener welds.

Since it was observed that the diaphragms were not very effective at distributing the load laterally, another appealing rehabilitation scheme would be the removal of all or some of the diaphragms. The effect of removing the diaphragms on the live load distribution amongst girders, the increase in transverse slab moments caused by the increase in differential displacements between girders, and the transfer of lateral loads through the structure would have to be assessed.

REFERENCES

AASHTO, (1983). AASHTO bridge design specifications. Washington, D.C.

AASHTO, (1998). AASHTO LRFD bridge design specifications. First edition. Washington, D.C.

American Railway Engineering Association (AREA), (1994). Manual for railway engineering. The American Railway Association, Chicago.

ASTM, (1997). ASTM Designation: A 370-97a – Standard test methods and definitions for mechanical testing of steel products. American Society for Testing and Materials, Philadelphia, PA.

Barth, A.S., Bowman, M.D., (1999). Fatigue behavior of intermittently welded diaphragm-to-beam connections. Structural Engineering in the 21st Century – Proceedings of the 1999 Structures Congress, ed. Avent and Alawady, pp. 805–808. ASCE, Reston, Virginia.

Canadian Standards Association (CSA), (1960). CSA-G40.8-1960 – Structural Steels with Improved Resistance to Brittle Fracture. Rexdale, Ontario.

Canadian Standards Association (CSA), (1988). CAN/CSA-S6-88 – Design of highway bridges. Rexdale, Ontario.

Canadian Standards Association (CSA), (1994). CAN/CSA-S16.1-94 – Limit states design of steel structures. Universal Offset Limited, Ontario.

Castiglioni, C.A., Fisher, J.W., Yen, B.T., (1988). Evaluation of fatigue cracking at cross diaphragms of a multigirder steel bridge. Journal of Constructional Steel Research, Vol. 9, pp. 95–110.

Cousins, T.E., Stallings, J.M., Lower, D.A., Stafford, T.E., (1998). Field evaluation of fatigue cracking in diaphragm-girder connections. ASCE Journal of Performance of Constructed Facilities, Vol. 12, No. 1, pp. 25–32.

Fraden, J., (1996). Handbook of modern sensors. Second edition. Springer – Verlag New York, Inc., Baltimore, MD.

Fisher, J.W., (1978). Fatigue cracking in bridges from out-of-plane displacements. Canadian Journal of Civil Engineering, Vol. 5, No. 4, pp. 542–556.

Fisher, J.W., Barthelemy, B.M., Mertz, D.R., Edinger, J.A., (1980). Fatigue behavior of full-scale welded bridge attachments. NCHRP Report No. 227, Transportation Research Board, National Research Council.

Fisher, J.W., Keating, P.B., (1989). Distortion-induced fatigue cracking of bridge details with web gaps. Journal of Constructional Steel Research, Vol. 12, pp. 215–228.

Fisher, J. W., Kulak, G. L. and Smith, I. F., (1998). A fatigue primer for structural engineers. National Steel Bridge Alliance, American Institute of Steel Construction, Chicago, IL.

Fisher, J.W., Yen, B.T., Wang, D., (1990). Fatigue strength of riveted bridge members. ASCE Journal of Structural Engineering, Vol. 116, No. 11, pp. 2968–2981.

Lai, L-Y, (1997). On drilling holes to arrest fatigue crack growth. Building to Last – Proceedings of the Structural Congress XV, Vol. 1, ed. Kempner and Brown. ASCE, New York, pp. 31–35

Mandel, J., (1964). Statistical analysis of experimental data. General Publishing, Ltd., Ontario.

Pullaro, J.J., (1990). Retrofit of cracked welded steel bridge girders. Extending the Life of Bridges, ed. Maupin, Brown and Lichtenstein. ASTM, Philadelphia, PA, pp. 18–31.

Reed, R.P., Clark, A.F., (1983). Materials at low temperatures. Carnes Publication Services, Inc., U.S.

Roberts, R., Fisher, J.W., Irwin, G.R., Boyer, K.D., Hausammann, H., Krishna, G.V., Morf, V., Slockbower, R.E., (1977). Determination of tolerable flaw sizes in full size welded bridge details. FHWA Report No. RD-77-170, Federal Highway Administration, Washington, D.C.

Schilling, C.G., Klippstein, K.H., Barsom, J.M., Novak, S.R., Balke, G.T., (1975). Low-temperature test of simulated bridge members, ASCE Journal of the Structural Division, Vol. 101, No. ST1, pp. 31–48.

Stallings, J.M., Cousins, T.E., Stafford, T.E., (1999). Removal of diaphragms from three-span steel girder bridge. ASCE Journal of Bridge Engineering, Vol. 4, No. 1, pp. 63–70.

Suresh, S. (1998). Fatigue of materials. Second edition. Cambridge University Press, Cambridge, U.K.

Tedesco, J.W., Stallings, J.M., Tow, D.R., (1995). Finite element method analysis of bridge girder–diaphragm interaction. International Journal of Computers and Structures, Vol. 56, No. 2/3, pp. 461–473.

Appendix A

Non-Critical Crack Growth Rate Curves

Figures A–1 through A–3 show the crack growth rate curves for all non-critical fatigue cracks observed during each of the three tests completed during the experimental testing program. The joint numbering system used in these figures is shown in Figure 5–2.
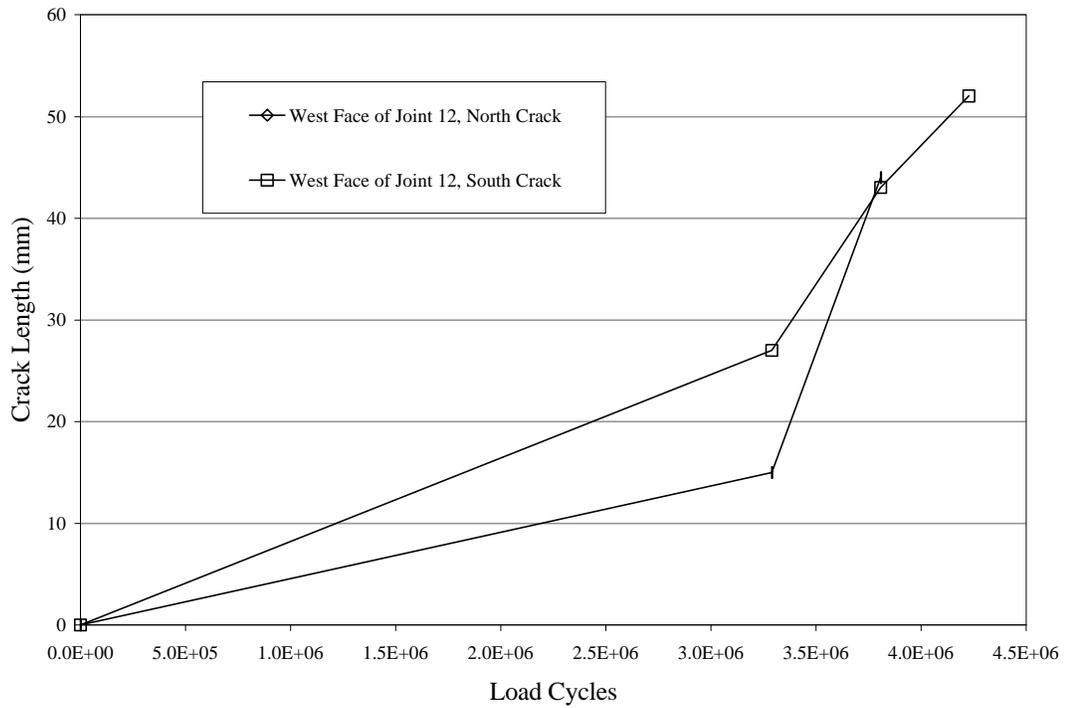

Figure A–1

Non-Critical Crack Lengths vs. Load Cycles, Test 1
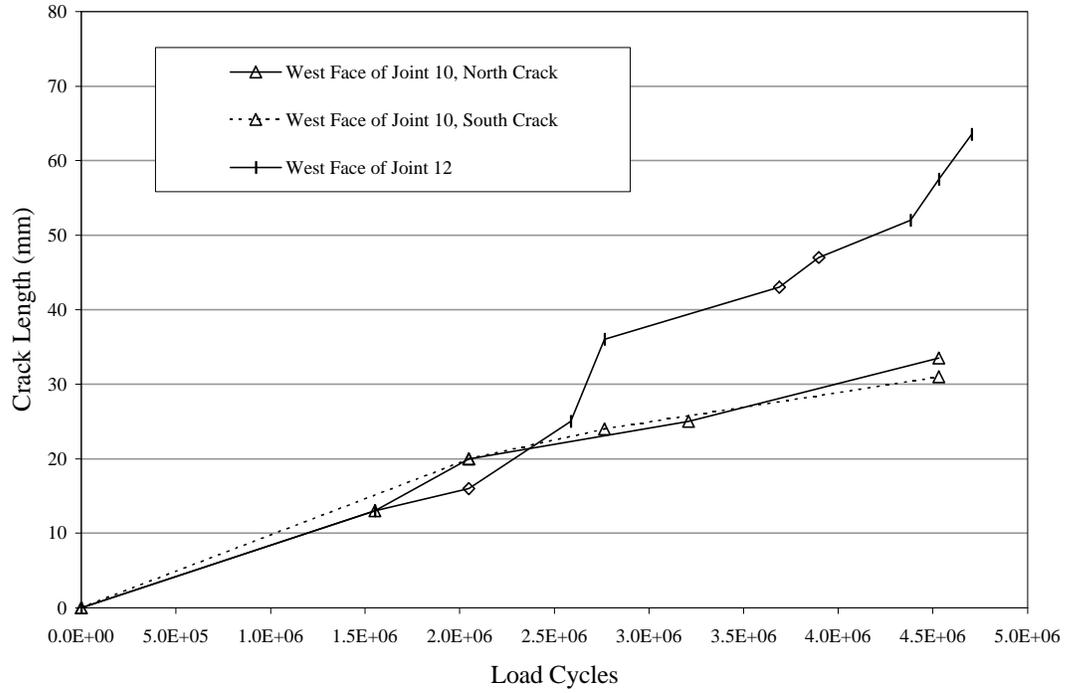
Figure A–2

Non-Critical Crack Lengths vs. Load Cycles, Test 2
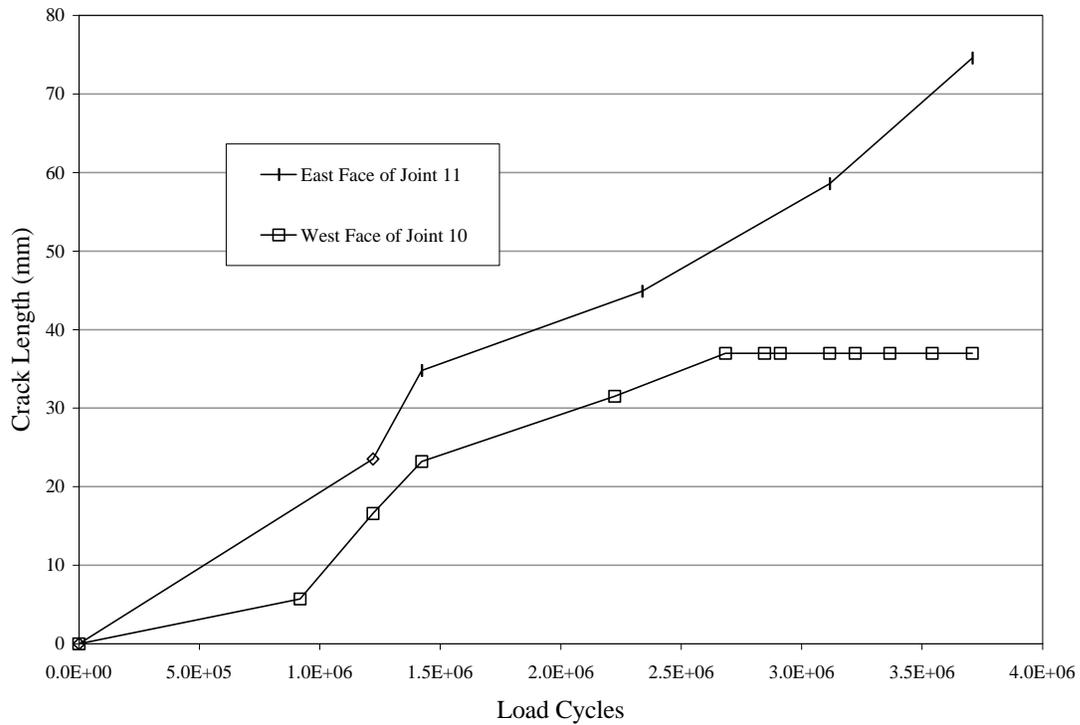

Figure A–3

Non-Critical Crack Lengths vs. Load Cycles, Test 3

142

Recent Structural Engineering Reports
Department of Civil & Environmental Engineering
University of Alberta

207. *Analytical Investigation of the Compressive Behaviour and Strength of Steel Gusset Plate Connections* by Michael C.H. Yam and J.J. Roger Cheng, December 1994.

208. *The Effect of Tension Flange Movement on the Strength of Point Loaded–Beams* by *Dean* Mullin and J.J. Roger Cheng, January 1995.

209. *Experimental Study of Transversely Loaded Continuous Steel Plates* by Kurt P. Ratzlaff and D.J. Laurie Kennedy, May 1995.

210. *Fatigue Tests of Riveted Bridge Girders* by Daniel Adamson and Geoffrey L. Kulak, July 1995.

211. *Fatigue of Riveted Tension Members* by Jeffrey DiBattista and Geoffrey L. *Kulak*, November 1995.

212. *Behaviour of Masonry Cavity Walls Subjected to Vertical Eccentric Loads* by Ru *Wang*, Alaa E. Elwi, Michael A. Hatzinikolas and Joseph Warwaruk, February 1996.

213. *Thermal Ice Loads on Structures* by Azita Azarnejad and Terry M. Hrudey, *November* 1996.

214. *Transmission of High Strength Concrete Column Loads Through Concrete Slabs* by *Carlos* E. Ospina and Scott D.B. Alexander, January 1997.

215. *Seismic Behaviour of Steel Plate Shear Walls* by Robert G. Driver, Geoffrey L. Kulak, D.J.Laurie Kennedy and Alaa E. Elwi, February 1997.

216. *Extended End Plate Moment Connections under Cyclic Loading* by Bryan T. Adey, Gilbert Y. Grondin and J.J. Roger Cheng, June 1997.

217. *Connection of Infill Panels in Steel Plate Shear Walls* by Ann S. Schumacher, Gilbert Y. Grondin and Geoffrey L. Kulak, August 1997.

218. *Shear Rehabilitation of G-Girder Bridges using CFRP Sheets* by John G.S. Alexander and J.J. Roger Cheng, October 1997.

219. *Seismic Evaluation of Steel Buildings with Concentrically Braced Frames* by Manoj S. Medhekar and D.J. Laurie Kennedy, October 1997.

220. *Rational Design of Prestressed and Reinforced Concrete Tanks* by Abdelaziz A. Rashed, David M. Rogowsky and Alaa E. Elwi, December 1997.

221. *Repair of Cracked Steel Elements using Composite Fibre Patching* by Gaylene D. Kennedy and J.J. Roger Cheng, May 1998.

222. *Strength of Joints that Combine Bolts and Welds* by Thomas J. Manuel and Geoffrey L. Kulak, July *1998*.

223. *Strip Model for Capacity of Slab-Column Connections* by Shahab Afhami, Scott D.B. *Alexander*, and Sidney H. Simmonds, August 1998.

224. *Behaviour of Large Diameter Line Pipe under Combined Loading* by Patrick R. DelCol, Gilbert Y. Grondin, J.J. Roger Cheng and David W. Murray, September 1998.

225. *An Analysis of the Cyclic Behaviour of Steel Gusset Plate Connections* by Scott S. Walbridge, Gilbert Y. Grondin, and J.J. Roger Cheng, September 1998.

226. *Rehabilitation of Unreinforced Masonry Walls with Externally Applied Fiber Reinforced Polymers* by Michael L. Albert, J.J. Roger Cheng, and A.E. Elwi, October, 1998.

227. *Fatigue of Bearing-Type Shear Splices* by Georg Josi, G.Y. Grondin, and G.L. Kulak, Apri*l, 1999.*

228. *Out-of-Plane Cyclic Behavior of Masonry Walls Reinforced Externally with GFRP by* Marc D. Kuzik, A.E. Elwi, and J.J. Roger Cheng, August 1999.

229. *Cyclic Behavior of Stiffened Gusset Plate–Brace Member Assemblies* by Trina Nast, G.Y. *Grondin*, and J.J.R. Cheng, November 1999.

230. *Behaviour of Sleeper-supported Line Pipe* by Jeffrey D. DiBattista, J.J.R. Cheng, and D.W. *Murray*, April 2000.

231. *Field Assessment of Crowchild Trail Bridge* by Kong K. Taing, J.J.R. Cheng, and S. Afhami, *January* 2000.

232. *Ductile Fracture of Steel* by Heng Aik Khoo, J.J. Roger Cheng, and T.M. Hrudey, August 2000.

233. *Shear Lag in Bolted Cold-Formed Steel Angles and Channels in Tension* by Amy Sin-Man *Yip* and J.J. Roger Cheng, September 2000.

234. *Behaviour of Reinforced Concrete Beams Strengthened in Shear with FRP Sheets* by Christophe Deniaud and J.J. Roger Cheng, October 2000.

235. *Behaviour of Distortion-Induced Fatigue Cracks in Bridge Girders* by R. Fraser, G.Y. *Grondin*, and G.L. Kulak, December 2000.